

# Kinematics, strain pattern and geochronology of the Salem-Attur shear zone: Tectonic implications for the multiple sheared Salem-Namakka blocks of the Southern Granulite terrane, India

B.M. Behera<sup>a,\*</sup>, B.D. Waele<sup>b,c</sup>, V. Thirukumaran<sup>d</sup>, K. Sundaralingam<sup>e</sup>, S. Narayanan<sup>a</sup>,  
B. Sivalingam<sup>a</sup>, T.K. Biswal<sup>a</sup>

<sup>a</sup> Department of Earth Sciences, Indian Institute of Technology Bombay, Mumbai 400 076, India

<sup>b</sup> SRK Consulting (Australasia) Pty Ltd, Level 1, 10 Richardson Street, WA6005 P.O. BOX 943, West Perth, WA 6872, Australia

<sup>c</sup> Department of Applied Geology, Curtin University, Kent St, Bentley, WA 6102, Australia

<sup>d</sup> Department of Geology, Govt. Arts College, Salem 636 007, India

<sup>e</sup> Geological Survey of India, Southern Region, Hyderabad, 500 068, India

## ARTICLE INFO

### Keywords:

Salem-Attur shear zone  
Southern Granulite terrane  
Polyphase shearing  
Strain partitioning  
Geochronology

## ABSTRACT

Structural mapping, strain analysis, and a variety of geochronological studies were carried out to determine the tectonothermal evolution of the Salem-Attur shear zone in the Southern Granulite terrane of South India. The Salem-Namakka blocks containing the shear zone consisted of quartzofeldspathic gneiss, charnockite and mafic granulite, and had undergone multiple phases of magmatism spanning over a period of 3.2–0.5 Ga. The rocks were deformed by four phases of deformation D<sub>1</sub>–D<sub>4</sub>. The D<sub>1</sub> deformation was characterized by isoclinal and recumbent NE-SW trending F<sub>1</sub> fold with a pervasive subhorizontal axial planar granulitic fabric, S<sub>1</sub>, and associated quartzofeldspathic leucosomes. Granulite metamorphism was dated at ca. 2.5–2.3 Ga. The F<sub>1</sub> fold and S<sub>1</sub> fabric were coaxially refolded by tight to isoclinal, upright to steeply inclined NE-SW trending F<sub>2</sub> folds during D<sub>2</sub> deformation. The D<sub>2</sub> deformation was associated with F<sub>2</sub> axial planar shear zones, crenulations and leucosomes, S<sub>2</sub> fabric. Large-scale D<sub>2</sub> shear zones characterized by high-temperature ductile shear fabric with a vertical flow host syntectonic syenite pluton which was dated at ca. 2.5–2.4 Ga. A P-T condition of 7 kb/600 °C was inferred for the D<sub>2</sub> deformation. The D<sub>3</sub> deformation was characterized by NW-SE to E-W trending F<sub>3</sub> folds and the Salem-Attur shear zone. The shear zone was a greenschist to amphibolite facies shear zone being characterized by mylonitic foliation and dominantly down-dip stretching lineation defined by quartz, biotite and hornblende minerals and dated at ca. 2.0 Ga. It indicated N-NNE vergence of thrusting with the mean kinematic vorticity number, *Wm*, as 0.7 suggesting general simple shear strain with 50% pure shear component. The D<sub>4</sub> deformation was manifested as NNE-SSW striking strike-slip faults and NW-SE striking extensional normal faults. Pseudotachylite veins having an age of 1.9 Ga injected during strike-slip faulting and granite-pegmatite veins showing age of 0.8–0.5 Ga intruded during normal faulting. The Salem-Namakka blocks thus recorded a long-lived shearing history. We suggest that the Salem-Attur shear zone and other shear zones such as Palghat-Cauvery, Moyar, Bhavani, Karur-Kambam-Painavu-Trichur and Achankovil shear zones, were Paleoproterozoic intraterrane shear zones which were overprinted by Meso-Neoproterozoic-Cambrian ductile and brittle deformations.

## 1. Introduction

The structural architecture of an orogen is often defined by shear zones which divide the orogen into a number of domains characterized by distinctive lithology, metamorphic history, structural style and geochronology (e.g., Himalaya orogen- Valdiya, 1984; Limpopo mobile

belt- McCourt and Vearncombe, 1987; Cap de Creus shear zone- Carreras and Druguet, 1994; Sierras Pampeanas shear zone- Sims et al., 1998; Eastern Ghats mobile belt- Biswal et al., 2007; Sierra Ballena shear zone- Oyhantcabal et al., 2010; Southern Granulite terrane, Plavsa et al., 2015). Shear zones undergo principally simple shear deformation, pure shear deformation associates in different proportions.

\* Corresponding author.

E-mail address: [beherabhubanmohan@gmail.com](mailto:beherabhubanmohan@gmail.com) (B.M. Behera).

<https://doi.org/10.1016/j.precamres.2019.01.022>

Received 20 August 2018; Received in revised form 29 December 2018; Accepted 29 January 2019

Available online 31 January 2019

0301-9268/ © 2019 Elsevier B.V. All rights reserved.

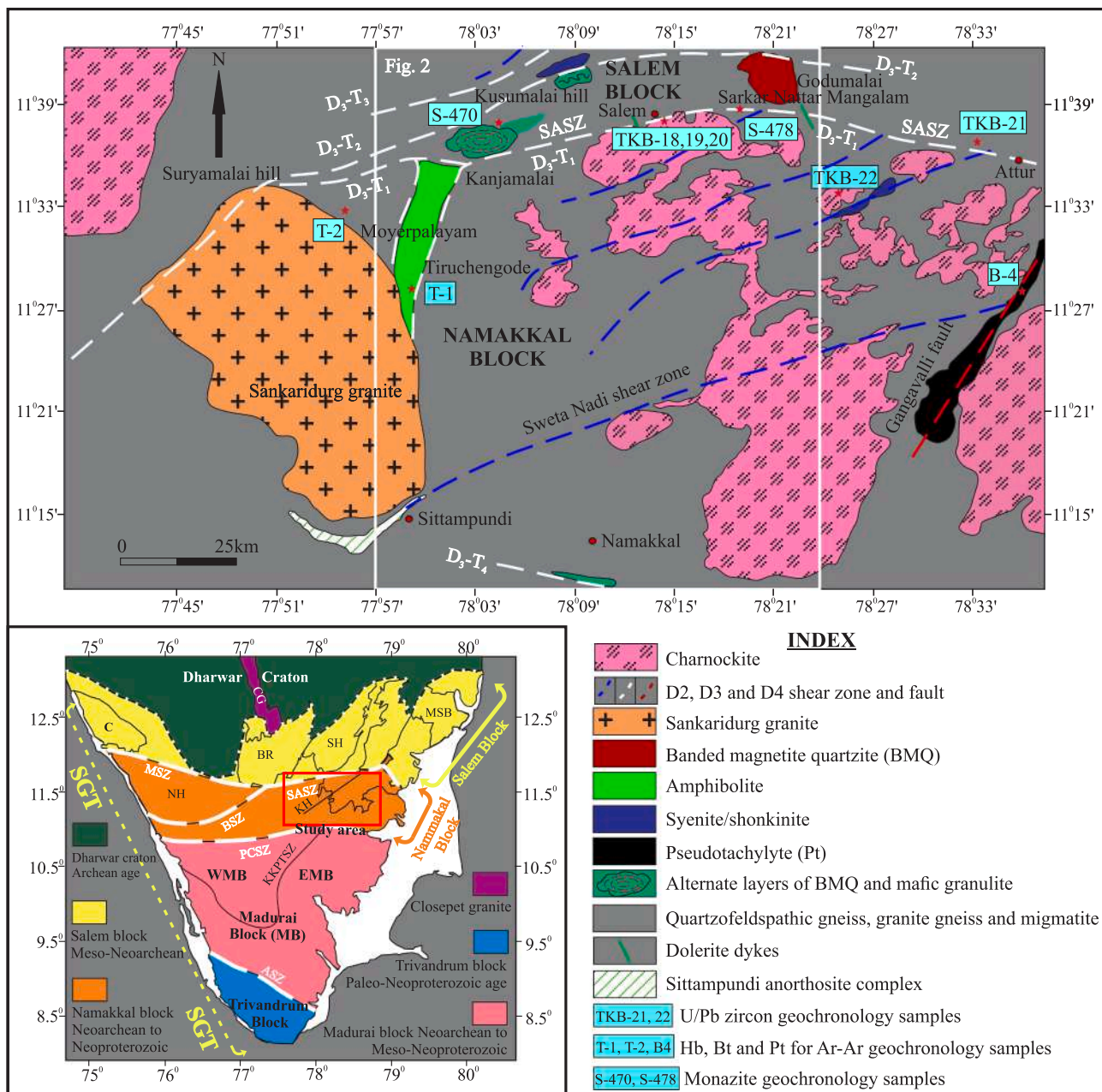


**Fig. 1.** Regional geological map of the Salem-Namakal blocks, northern part of the SGT (Sundaralingam et al., 2017). D<sub>2</sub>, D<sub>3</sub> and D<sub>4</sub> shear zones/faults are marked in blue, white and red, respectively. Two zircon geochronology samples are plotted in the map, as their locations lie outside the area in Fig. 2. Fig. 2 is marked by white box. *Inset:* Geological map of the SGT (Ramakrishnan and Vaidyanadhan, 2008). ASZ- Achankovil shear zone, BR- Biligirirangan, BSZ- Bhabani shear zone, C- Coorg, CG- Closepet granite, EDC- Eastern Dharwar craton, FL- Fermor’s line, KH- Koli hill, KKPTSZ- Karur-Kambam-Painavu-Trichur shear zone, MSB- Madras block, MSZ- Moyar shear zone, PCSZ- Palghat Cauvery shear zone, SASZ- Salem-Attur shear zone, SH- Shevroy hill, WDC- Western Dharwar craton. (For interpretation of the references to color in this figure legend, the reader is referred to the web version of this article.)

Depending on the nature of deformation, shear zones can be characterized by a variety of strain fabrics (Ramsay, 1980; Fossen and Cavalcante, 2017). Mapping out shear zones and structural domains and interpreting the deformation history, shear kinematics, nature of strain and timing of deformation, using different geochronological techniques, help unravel the tectonic history of a mobile belt (Sims et al., 1998; Dumond et al., 2008, 2015; Oyhantcabal et al., 2012; Oriolo et al., 2016).

The Neoproterozoic to Neoproterozoic Southern Granulite terrane (SGT) of South India is transected by several shear zones (Fig. 1 inset) which were considered to be suture between different tectonic blocks (Santosh et al., 2013; Brandt et al., 2014). The Salem-Attur shear zone, the focus of this paper, occurs in the northern part of the SGT. The shear

zone was described as a dextral strike-slip shear zone delineating two contrasting blocks namely Archean Salem block in the North and the Paleoproterozoic Palghat-Cauvery block in the south (also referred to as the Namakal block) (Chetty, 1996; Chetty and Rao, 1998, 2006; Chetty et al., 2003; Ghosh et al., 2004; Plavsa et al., 2015). Our study focuses on the tectonothermal evolution of the Salem-Attur shear zone based on detailed structural mapping, petrofabric analysis, strain estimation and geochronology. We have constrained the deformation events by zircon U-Pb SHRIMP geochronology on igneous intrusions, monazite U-Th-Pb EPMA dating on metamorphic and sheared rocks and hornblende/biotite <sup>40</sup>Ar/<sup>39</sup>Ar dating of pseudotachylite from shear zones and brittle faults. Our study of the Salem-Attur shear zone provides a better understanding of the evolution of SGT in general and

allows regional correlation with other segments of Peninsular India as well as adjoining continents within the Gondwanaland assembly.

## 2. Geological background

The SGT consists of several tectonic blocks bound by shear zones (Fig. 1 inset). These blocks are characterized by distinct lithological assemblages, grades of metamorphism and isotopic ages. From north to south, these are (i) the Salem block (between the Dharwar craton and the Salem-Attur shear zone), (ii) the Namakkal block (previously referred as the Palghat-Cauvery shear system, bounded by the Salem-Attur and Palghat-Cauvery shear zones), (iii) the Madurai block (between the Palghat-Cauvery shear zone and the Achankovil shear zone), (iv) the Trivandrum block (south of the Achankovil shear zone and (v) the Nagercoil block (Santosh et al., 2009a).

The Salem block consisted of isolated hills of Meso-Neoproterozoic quartzofeldspathic gneiss, charnockite, mafic granulite and BIF. The intrusion of parent magma of mafic granulite was constrained at ca. 2.7 Ga (Sato et al., 2011a), charnockite at 2.6 Ga (Vinogradov et al., 1964; Clark et al., 2009; Saitoh et al., 2011), granite gneiss at ca. 2.5 Ga (Saitoh et al., 2011) and shonkinite and ultramafic rocks at ca. 0.8 Ga (Friend and Janardhan, 1984; Reddy et al., 1995). Several episodes of granulite facies metamorphism affected the block at ca. 2.5 Ga, (Peucat et al., 1993; Sato et al., 2011a; Anderson et al., 2012), ca. 0.7 Ga (Bhaskar Rao et al., 1996) and ca. 0.6 Ga (Ghosh et al., 2004; Bhutani et al., 2007). It was interpreted that the Salem block represented the southern extension of the Dharwar craton, where the greenstone-tonalite-trondhjemite-granodiorite rocks of the craton were metamorphosed to granulite facies (Friend and Nutman, 1992; Bartlett et al., 1998; Bhaskar Rao et al., 2003; Ghosh et al., 2004). The P-T conditions of 8–14 kb/800–900 °C were estimated for the garnet-orthopyroxene-clinopyroxene-plagioclase assemblage in the Salem block (Mukhopadhyay and Bose, 1994).

The Namakkal block consisted of a similar lithological assemblage and was intruded by ultramafic, ultrabasic and granite rocks of Neoproterozoic to Neoproterozoic ages. The anorthosite pluton at Sittampundi containing mafic granulite enclaves yielding crystallization ages of ca. 2.9 Ga and 2.5 Ga, and a metamorphic ages of 0.7 Ga (Subramanyam, 1956; Rao et al., 1996; Dharma Rao et al., 2013; Mohan et al., 2013). The Sankaridurg granite pluton with several small to large scale roof pendants of marble, pelitic rock and quartzite, was emplaced between 0.6 Ga to 0.4 Ga age (Condie, 1986; Pandey et al., 1993; Ghosh et al., 1994; Nathan et al., 1994; Santosh et al., 2005). Granulite facies metamorphism belonged to two phases at ca. 2.5 Ga (Ghosh et al., 2004; Plavsa et al., 2015) and ca. 0.5 Ga (Collins et al., 2007a; Raith et al., 2010; Santosh et al., 2012). Both high pressure (eclogite facies, Shimpou et al., 2006; Tsunogae and Santosh, 2006; Sato et al., 2009) and ultrahigh temperature metamorphism (sapphirine and quartz bearing rocks: Kelsey, 2008; Nishimiya et al., 2009) of Neoproterozoic-cambrian phase associated with the Namakkal block. Different interpretations have been proposed for the tectonic setting of this block. One view proposed that it was a part of the reworked Archean Dharwar craton (Harris et al., 1994; Rao et al., 1996; Chetty et al., 2003; Ghosh et al., 2004; Tomson et al., 2006). An alternative model suggested a Cryogenian supra-subduction zone (Santosh et al., 2009a, 2012; Yellappa et al., 2010; Sato et al., 2011b), while another model suggested the Namakkal block represented a collapsed marginal basin (Drury and Holt, 1980). The block was previously known as the Palghat-Cauvery shear system as it contained several ENE-WSW striking shear zones identified by remote sensing. The shear zones were interpreted to constitute a transpressive dextral shear zone system producing a flower structure (Drury and Holt, 1980; Chetty et al., 2003; Chetty and Rao, 2006). The Moyar-Attur-Bhavani shear zone along the northern margin of the shear system was characterized by E-W striking dextral strike-slip (Plavsa et al., 2015). The NW-SE Palghat-Cauvery shear zone along the southern margin of the shear system represented

an extremely shortened zone (Mukhopadhyay et al., 2003), dextral strike-slip shear zone (Drury and Holt, 1980) and a zone of juxtaposition of blocks of different geochronological ages and metamorphism (Harris et al., 1994; John et al., 2005). The Palghat-Cauvery shear zone is further considered to mark the location where the Mozambique ocean was subducted during amalgamation of the Madurai and Salem-Namakkal blocks (e.g., Collins et al., 2014).

The Madurai block was divided into two sub-blocks namely the Neoproterozoic western Madurai and Meso-Neoproterozoic eastern Madurai sub-blocks along the Karur-Kambam-Painavu-Trichur shear zone (Ghosh et al., 2004; Brandt et al., 2014). The Dharwar craton was believed to extend up to the Karur-Kambam-Painavu-Trichur shear zone (Ghosh et al., 2004; Brandt et al., 2014). However, Palaeoproterozoic (2.0–1.6 Ga) crust existed in the Madurai as well as Trivandrum block (Braun et al., 1998; Ghosh et al., 2004). The metamorphism in the Madurai block was constrained at 0.6–0.5 Ga under UHT conditions (Jayananda et al., 1995; Bartlett et al., 1998; Braun, 2006; Santosh et al., 2006a; Braun et al., 2007; Collins et al., 2007b; Brandt et al., 2011).

The Achankovil shear zone juxtaposed the Madurai block with Trivandrum block and interpreted as a magnetic lineament (Rajaram et al., 2003), a dextral or sinistral shear zone (Drury et al., 1984; Rajesh and Chetty, 2006), and coaxial deformation zone (Ghosh et al., 2004). The shear zone experienced high temperature and pressure metamorphism at ca. 0.5 Ga (Santosh et al., 2009b). The Trivandrum block is dominated by khondalites with protolith-sedimentation age was at ca. 1.9 Ga, and recording high-grade metamorphism around 0.5 Ga (Ghosh et al., 2004; Santosh et al., 2006b, c; Collins et al., 2007b). The Nagercoil block was interpreted to have a similar age and evolution as the Trivandrum block (Santosh et al., 2006c) and contained charnockites with a chemistry showing an arc signature (Santosh et al., 2009a).

Kinematics of the shear zones in SGT were interpreted by remote sensing analysis only, leading to contrasting views. Based on remote sensing, the Salem-Attur shear zone has previously been interpreted as a strike-slip (Drury et al., 1984; Satheesh Kumar and Prasannakumar, 2009), a transpressive (Chetty, 1996; Chetty and Rao, 1996; Plavsa et al., 2015) or compressive shear zone (Naha and Srinivasan, 1996; Biswal et al., 2009, 2010; Sundaralingam et al., 2012, 2017), while strike-slip faults hosting pseudotachylites have been interpreted to be produced from N-S compression (Behera et al., 2017).

## 3. Methodology

### 3.1. Structural mapping, sampling and petrography

The Salem-Namakkal blocks including the Salem-Attur shear zone were mapped at 1:10,000 scale (Fig. 2). The structural features were photographed on profile section (Figs. 3–5, 7 and 8) and structural data are presented in stereonet (Fig. 2 insets). Samples were collected from different lithounits for petrographic work. Oriented samples were collected at regular interval along a profile across the strike of the shear zones (Fig. 6). The mylonitic foliation and stretching lineations were marked on the sample. The samples were cut into foliation perpendicular thin sections; one section was parallel to lineation (XZ section) and another perpendicular to lineation (YZ section). Photomicrographs of the XZ sections were presented in Fig. 8, which were studied for kinematic and vorticity analysis.

### 3.2. Mean kinematic vorticity number

The mean kinematic vorticity number ( $Wm$ ) is an approximate measure of the relative proportion of simple shear and pure shear components (Ghosh and Ramberg, 1976; Passchier, 1987). Several vorticity gauges, including (i) clast-based gauges (Ghosh and Ramberg, 1976; Passchier, 1987; Simpson and De Paor, 1993; Wallis et al., 1993),

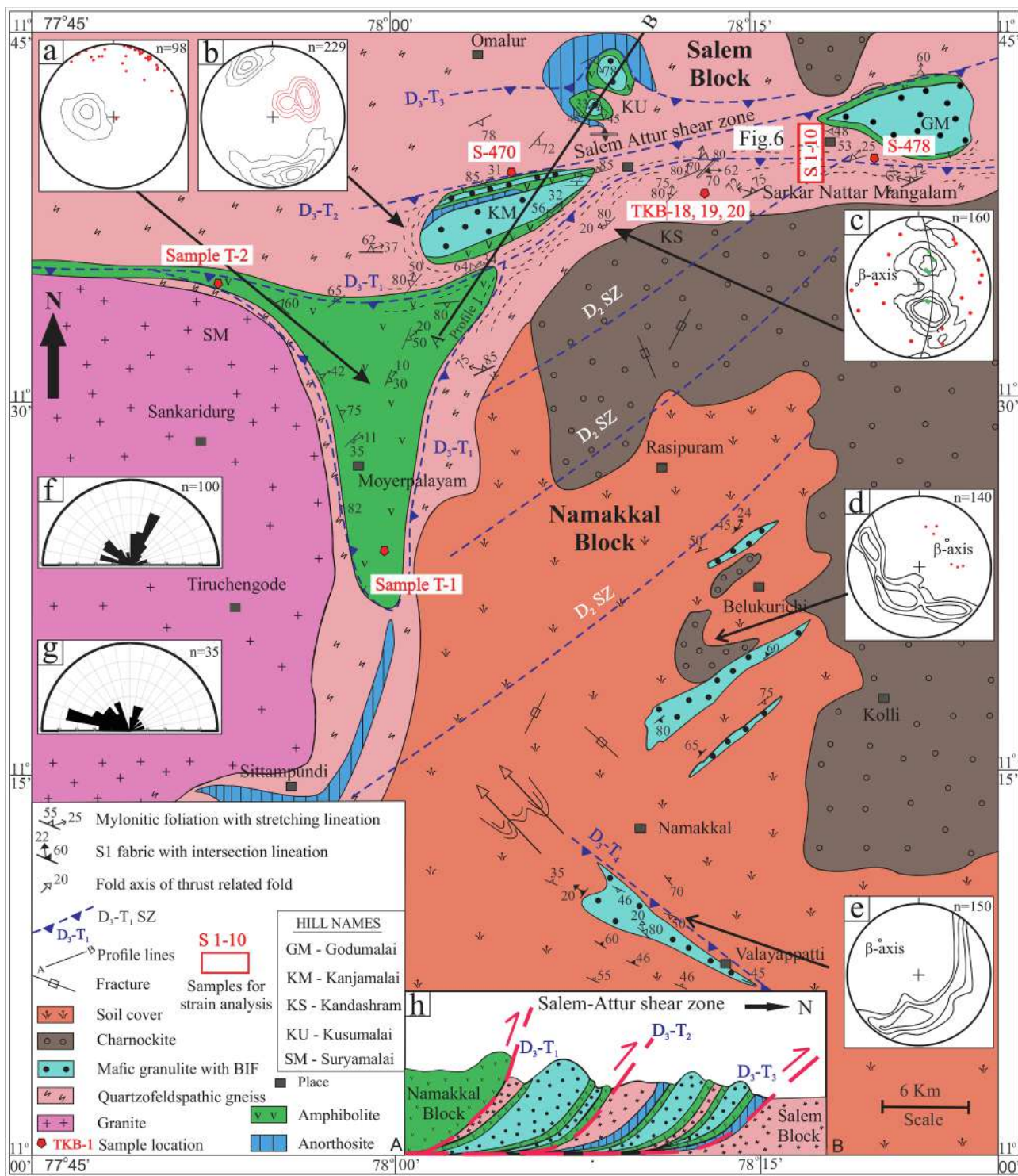
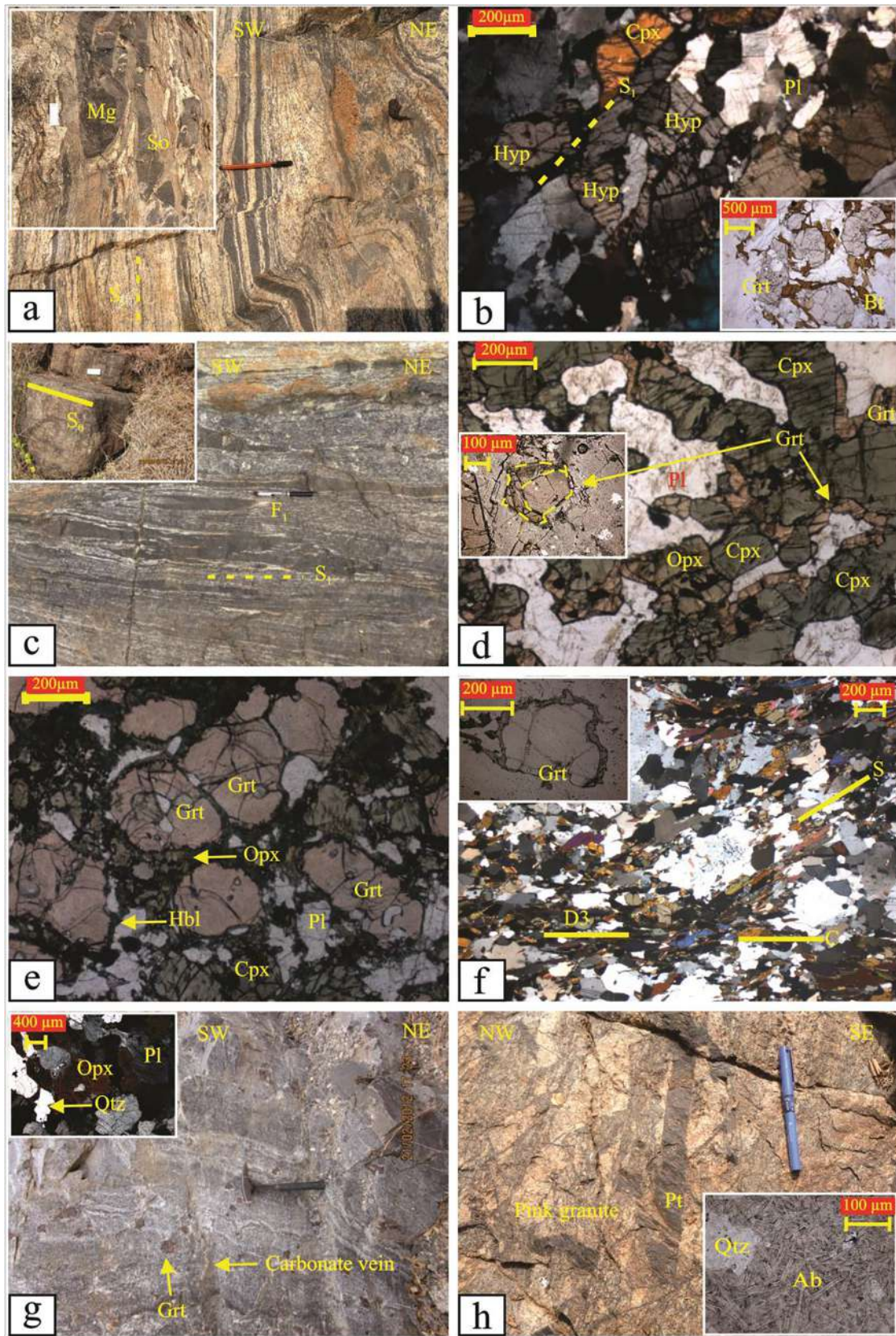


**Fig. 2. Structural map of the Salem-Namakkal blocks.** Geochronology sample locations are plotted in red colour. (a–e) Stereoplots of structural features for Moyerpalayam, Kanjamalai, Kandashram, Belukurichi and Namakkal areas. (a) 98 mylonitic foliations, contours in black, 1–5–10%; 53 stretching lineations plotted as red colored dots; (b) 229 S<sub>1</sub> fabric, contours in black, 1–2–3–5–10%, 125 fold axis and lineation, contours in red, 1,2,5,10%; (c) 160 S<sub>1</sub> fabric and mylonitic foliation, contours in black, 1–3–5–10%, girdle with westerly low plunging β axis. There are two sets of lineation, green dots indicate stretching lineations and red dots, fold axis; (d) 140 S<sub>1</sub> fabrics, contours in black, 1–5–10%, girdle distribution with northeasterly plunging β axis. Red dots indicate F<sub>1</sub>-F<sub>2</sub> fold axis; (e) 150 S<sub>1</sub> fabrics show girdle distribution, β axis of F<sub>3</sub> fold plunges to NW, Contours 1–5–10%; (f, g) Rose diagrams for strike-slip and normal faults respectively; (h) Suggestive A-B profile across Salem-Attur shear zone, illustrating D<sub>3</sub>-T<sub>1</sub>, D<sub>3</sub>-T<sub>2</sub> and D<sub>3</sub>-T<sub>3</sub> thrusts that merge at depth, forming a leading imbricate structure. Shear zones are marked in blue color. (For interpretation of the references to color in this figure legend, the reader is referred to the web version of this article.)

(ii) the angle between macroscopic foliation and shear zone boundary ( $R_s/\theta$  or  $R_{xz}/\beta$ ,  $R_{xz}/\theta$ ) (Ramsay and Huber, 1987; Tikoff and Fossen, 1995), (iii) oblique dynamically recrystallized grain shape foliation

(Wallis, 1995) and (iv)  $R_{xz}/\delta$  method (Xypolias 2009, 2010) have been applied to deformed rocks. Here, we followed the clast-based and the  $R_s/\theta$  techniques. In the clast-based method, the aspect ratio and



(caption on next page)

**Fig. 3.** (a) Field photograph, quartzofeldspathic gneiss in the Namakkal block, dark layers ( $S_1$ ) contain hypersthene and biotite, and white layers are quartz and plagioclase bearing. *Inset:* mafic granulite (Mg) band defining  $S_0$  is present within the quartzofeldspathic gneiss; (b) Photomicrograph of quartzofeldspathic gneiss with hypersthene (Hyp) and  $S_1$  foliation. *Inset:* garnet (Grt) porphyroblast surrounded by biotite, indicating retrogression; (c) Mafic granulite consisting of alternate enderbyte layer with plagioclase + quartz and dark garnet + pyroxene-rich layer, the layers define the  $S_1$  foliation.  $F_1$  fold is present in the center. *Inset:* primary cumulate layers ( $S_0$ ) containing pyroxene and magnetite; (d) Photomicrograph of mafic granulite in the Salem block: garnet corona (Grt) is developed around hypersthene (Opx), clinopyroxene (Cpx) and first stage garnet (Grt-inset), in contact with plagioclase; this marks isobaric cooling or loading; (e) Mafic granulite in the Namakkal block: garnet (Grt) is surrounded by hypersthene-corona (Hyp). Hornblende (Hbl) is developed due to retrogression of hypersthene and pyroxene; (f) Amphibolite at Moyerpalayam contains hornblende and biotite defining  $D_3$ -S-C fabric. *Inset:* garnet is retrograded to epidote; (g) Charnockite contains dark and white layers ( $S_1$  foliation), garnet (Grt) porphyroblasts are present randomly in the rock. Carbonate veins (white colour) cross cut the  $S_1$  foliation. *Inset:* Charnockite contains quartz, hypersthene and plagioclase; (h) Pseudotachylite (Pt) veins cross cutting the pink granite. *Inset:* Albite (Ab) microlites and quartz (Qtz) clasts in Pt. (For interpretation of the references to color in this figure legend, the reader is referred to the web version of this article.)

inclination of porphyroclasts to the shear plane constitute the base data. The 'imageJ' software was used to measure the aspect ratio of the feldspar porphyroclasts. The basic principle underlying the clast based method is that the porphyroclasts rotate in response to shearing. Simple shearing produces forward rotation for any aspect ratio of the clast while pure shearing will tend to rotate clasts in opposite direction if they are oppositely inclined. In general shear, depending on the proportion of pure shear to simple shear, certain aspect ratios of grains will have a forward rotation, even if they are inclined in the opposite direction. Other grains can show a backward rotation while some will show zero rotation rates. Grains with zero rotation rates have critical aspect ratio ( $R_{crit}$ ) (Ghosh and Ramberg, 1976; Passchier, 1987, 1997; Simpson and De Paor, 1993, 1997; Stahr and Law, 2011, 2014).  $R_{crit}$  is a direct measure of the mean kinematic vorticity number,  $Wm$  ( $Wm = R_{crit}^2 - 1/R_{crit}^2 + 1$ ) and can be determined geometrically (Rigid Grain Net of Jessup et al., 2007). In the  $Rs/\theta$  method, the strain ratio ( $Rs$ ) is calculated using  $R_f/\phi$  method (Ramsay, 1967; Lisle, 1985). The  $\theta$  angle is obtained by measuring the inclination of the long axis of the quartz grains (S-fabric) with the C-fabric. The  $S^{\circ}C$  angle is a measure of instantaneous strain. If the flow is non-steady,  $\theta$  values will represent the last instantaneous strain (Wallis, 1995). The  $Wm$  is determined from the equation,

$$Wm = \cos[\tan^{-1}\{1 - R_s \tan^2\theta / (1 + R_s) \tan\theta\}]$$

(Xypolias, 2009).

We carried out vorticity analysis of  $D_3$  mylonites of the Salem-Attur shear zone near Sarkar Nattar Mangalam (Figs. 2 and 6). The shear zones lacked P-bands and fissure veins, suggesting that there was minimal volume change (e.g., Ramsay and Lisle, 2000). Feldspar porphyroclasts were devoid of dynamic recrystallization and constituted the major population of rigid grains. They were widely spaced, so they didn't interfere during the rotation. A large variety of aspect ratios were included in the analysis. There were few grains with aspect ratios  $> 5.0$  as the samples used for analysis were from mylonite and ultramylonite. The aspect ratio ( $B^*$ ), vorticity number ( $Wm$ ) and percentage of pure shear were calculated following Jessup et al. (2007) (for RGN plot, Fig. 9). Further,  $Rs$  of the dynamically recrystallized quartz grains was measured on the same petrographic section whose RGN analysis was carried out. The  $Rs$  was plotted against  $\theta$  to get the  $Wm$  (Fig. 10a, Ramsay and Huber, 1987; Tikoff and Fossen, 1995). A comparison of  $Wm$  obtained by both methods is provided in Fig. 10b and Table 1 (e.g., Tikoff and Fossen, 1995). The values were furthermore, matched with that of Flinn's plot between X/Y and Y/Z ratio of quartz grains (Fig. 10c).

### 3.3. Zircon U-Pb geochronology

Zircon has a high closure temperature ( $> 900$  °C) to the U-Th-Pb system and is therefore ideal to date the crystallization age of intrusive and extrusive rocks (Dahl, 1997; Cherniak and Watson, 2001). We have applied zircon geochronology to date charnockite and granite in the Salem-Namakkal blocks. Zircon U-Pb geochronology was conducted on the SHRIMP ion microprobe at the John de Laeter Centre for Mass Spectrometry at Curtin University in Perth, Australia. Zircon of all shapes and sizes were handpicked and mounted in epoxy resin together

with natural zircon standard BR266 (Stern, 2001), TEMORA-2 (Black et al., 2003, 2004) and CZ3 (Pidgeon, 1994). The samples were loaded in the SHRIMP sample lock 24 h prior to analysis and pumped to  $\sim 5 \times 10^{-7}$  Torr to allow degassing. Analytical procedure of the SHRIMP follows methods similar to those described in detail by Claoue-Long (1994). Working conditions for both sessions included a primary beam current of 2–3 nA, slightly elliptical spot size of  $\sim 25$ – $30$   $\mu$ m, the sensitivity of  $> 20$  counts per ppm Pb and per nA primary beam current, and a mass resolution of  $> 4500$ . Measurements were conducted on  $Zr_2O^+$ ,  $^{204}Pb^+$ , background,  $^{206}Pb^+$ ,  $^{207}Pb^+$ ,  $^{208}Pb^+$ ,  $^{238}U^+$ ,  $^{232}ThO^+$  and  $^{238}UO_2^+$  in sets of six scans, with a total analysis time of about 15 min per sample spot. Analyses of unknown and BR266 standard zircon were interspersed at a ratio 3:1, allowing calibration of  $^{238}U/^{206}Pb$  ratios and U content using an age of 559 Ma and U content of 909 ppm (Stern, 2001). TEMORA-2 and CZ3 were used as control standards and yielded  $^{206}Pb/^{238}U$  ages within the error of those reported for them (Pidgeon, 1994; Black et al., 2003, 2004). Common Pb correction is based on measure non-radiogenic  $^{204}Pb$  isotope, and a common Pb composition applied following the Pb-evolution model of Stacey and Kramers (1975). Because analyses that recorded high counts on  $^{204}Pb$  during the first scan were aborted, corrections are small and insensitive to the choice of common Pb composition. Nevertheless, some analyses were characterized by very low contents of U, which combined with the relatively young age, lead to low amounts of radiogenic Pb. In these cases, proportions of common Pb can become relatively high, even though counts on  $^{204}Pb$  were barely above background. Because of the low signal to noise ratio of the  $^{204}Pb$  signal, 204-correction suffers from imprecision particularly in these cases, and we, therefore, report uncorrected ratios in the table (Table 2), and in some cases used these uncorrected values to regress the data to common Pb and constrain an intercept age. Standard calibration errors are reported in the table, but were not included in single spot ages and pooled age calculations. Single spot ages are reported at the  $1\sigma$  confidence level, while pooled ages are reported at 95% confidence.

### 3.4. EPMA Th-U-total Pb monazite geochronology

Monazite CHIME geochronology is an effective tool to constrain the tectonic evolution of a geological terrane by correlating ages of monazite in microfibrils with the timing of deformation of the rock. Because it contains a significant amount of Th and U and lacks common Pb, it has been used for Th-U-Pb geochronology by chemical analysis in Electron Probe Microanalyzer (Suzuki and Adachi, 1991; Montel et al., 1996; Williams et al., 2007). Monazite can form as part of metamorphic and hydrothermal events, with closure temperature for Th-U-Pb as high as  $> 800$  °C (Cherniak et al., 2004; Cherniak and Pyle, 2008). At higher temperature, monazite develops dislocation creep (DC) and records fabrics similar to metamorphic minerals. However, monazite can also undergo dissolution and reprecipitation at lower temperatures through dissolution precipitation creep (DPC) (Krohe and Wawrzenitz, 2000; Wawrzenitz et al., 2012). In DPC, newly formed monazite replaces pre-existing grains and forms distinct compositional domains in Backscatter Scanning Electron Microscopy imagery (Zhu and O'Nions, 1999; Williams and Jercinovic, 2002; Pyle and Spear, 2003; Foster et al.,

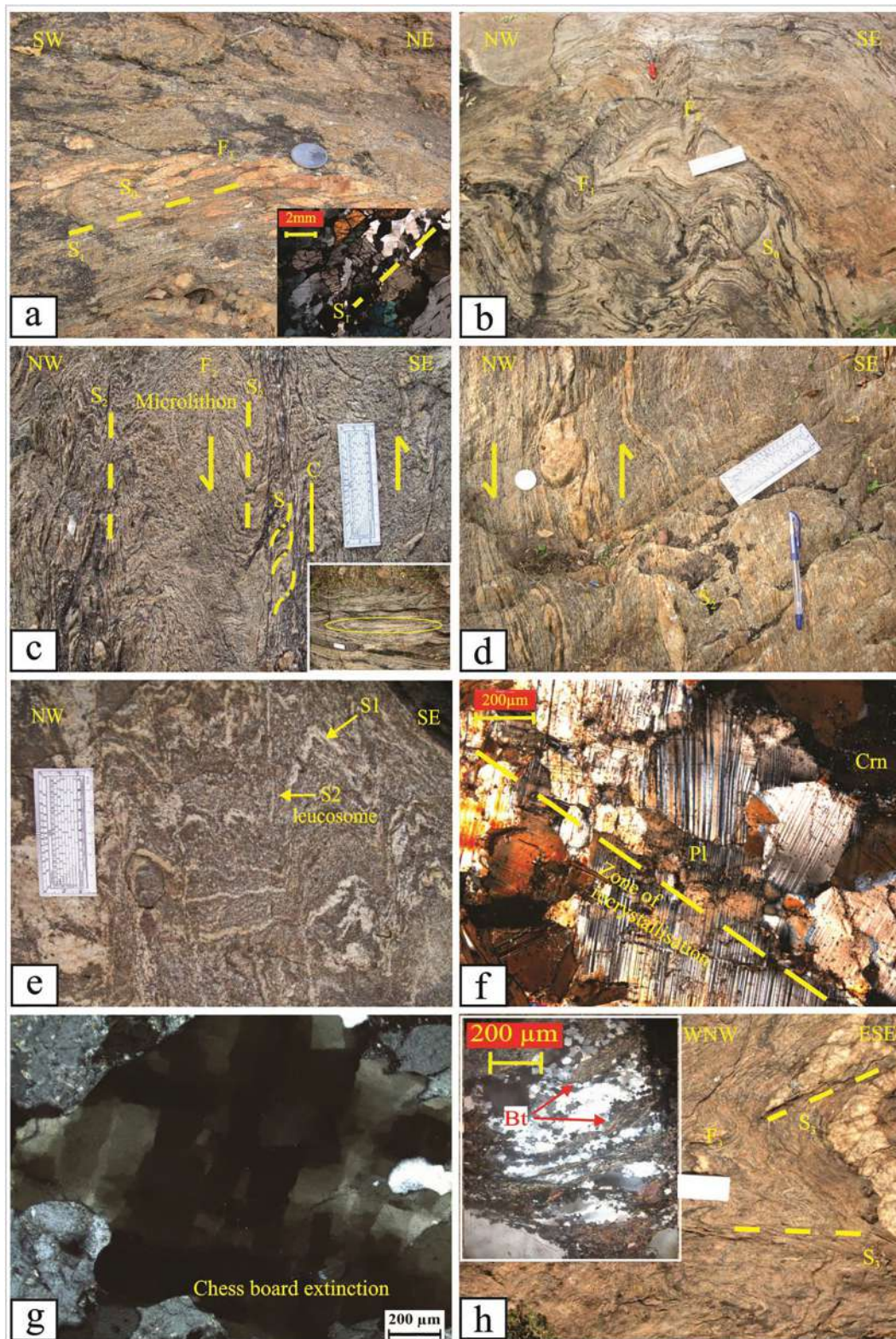


**Fig. 4.** (a) Horizontal view, metachert/quartzite layers ( $S_0$ ) in the quartzofeldspathic gneiss are folded by isoclinal  $F_1$  folds. Axial planar gneissosity ( $S_1$ ) cross cut the  $S_0$  at the hinge zone. *Inset:*  $S_1$  fabric is defined by mineral alignment; (b) Vertical view,  $F_1$  is coaxially refolded by NE-SW trending  $F_2$  fold producing type-3 interference; (c) Vertical section,  $D_2$  shear bands ( $S_2$ ) and microlithons associated with  $F_2$  fold, S-C fabric is developed along the shear band. *Inset:*  $F_1$  sheath fold on horizontal surface; (d) Vertical section, boudins were rotated in anticlockwise manner along the shear band; (e)  $S_1$  and  $S_2$  leucosomes cross cutting each other.  $S_1$  leucosome is folded by  $F_2$ ; (f) Syenite intruded along  $D_2$  shear zone shows dynamically recrystallization of plagioclase (Pl), suggesting high temperature of deformation (Crn-Corundum); (g) Chessboard extinction in the quartz in the syenite suggesting high temperature of deformation; (h) Horizontal section, NW-SE to E-W striking  $F_3$  folds with axial planar shear,  $S_3$ . *Inset:* Retrogression of minerals to biotite (Bt) along  $S_3$ .

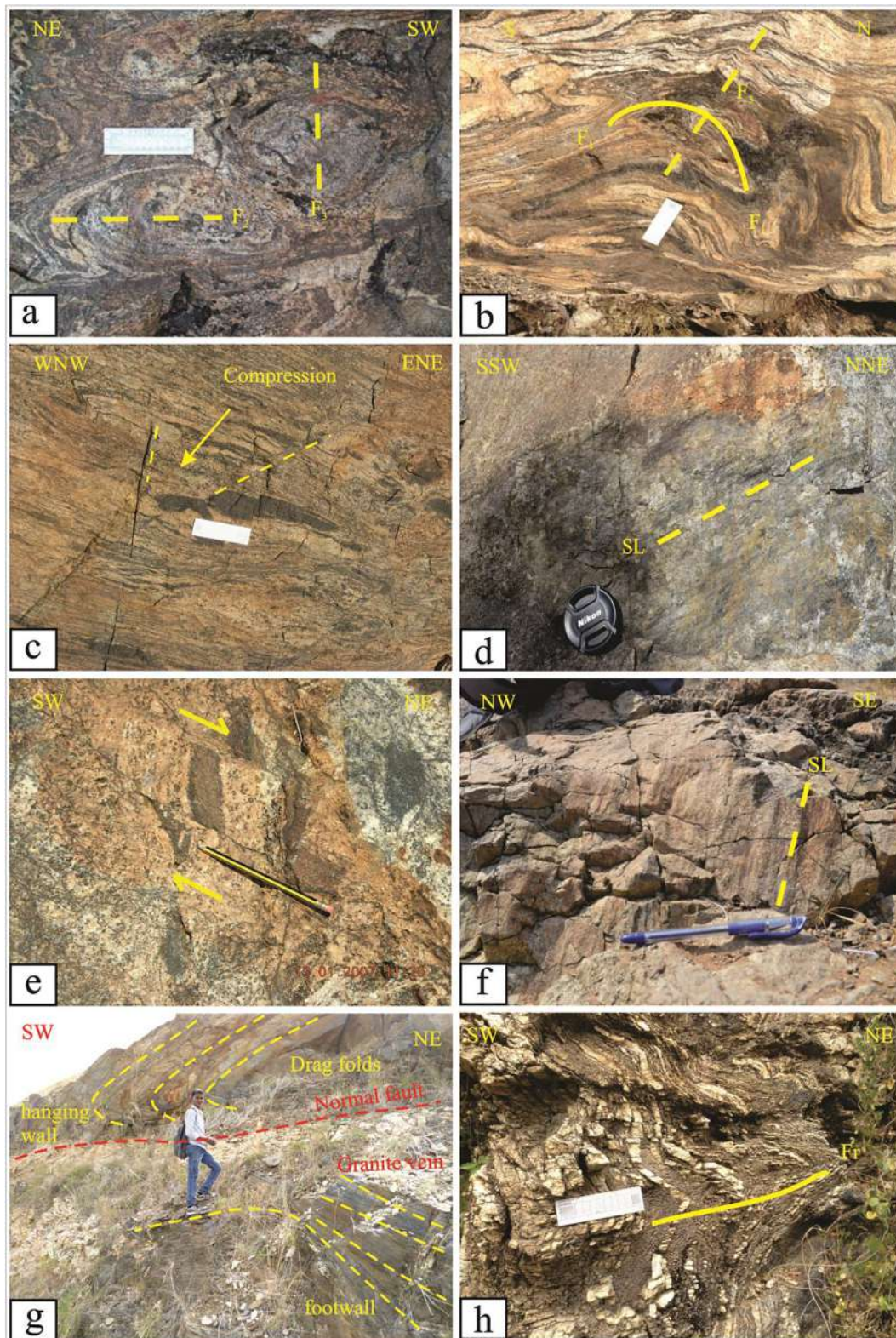


**Fig. 5.** (a) Horizontal view, type-1 interference pattern due to  $F_3$  superimposed on  $F_2$ ; (b) Vertical view, type-2 interference pattern due to superposition of  $F_3$  on recumbent  $F_1$ ; (c) Horizontal view, conjugate strike-slip faults in quartzofeldspathic gneiss, compression direction marked by arrow; (d) Vertical view, low angle slickenlines (SL) on strike-slip fault; (e) Vertical view, normal faults; (f) Down dip slickenlines (SL) on steep normal fault; (g) Vertical view, drag fold in the hanging wall of low angle normal fault. Granite/pegmatite vein intruded along the fault; (h) Vertical view, disjunctive fracture (Fr) appearing as cleavage in a recumbent fold.

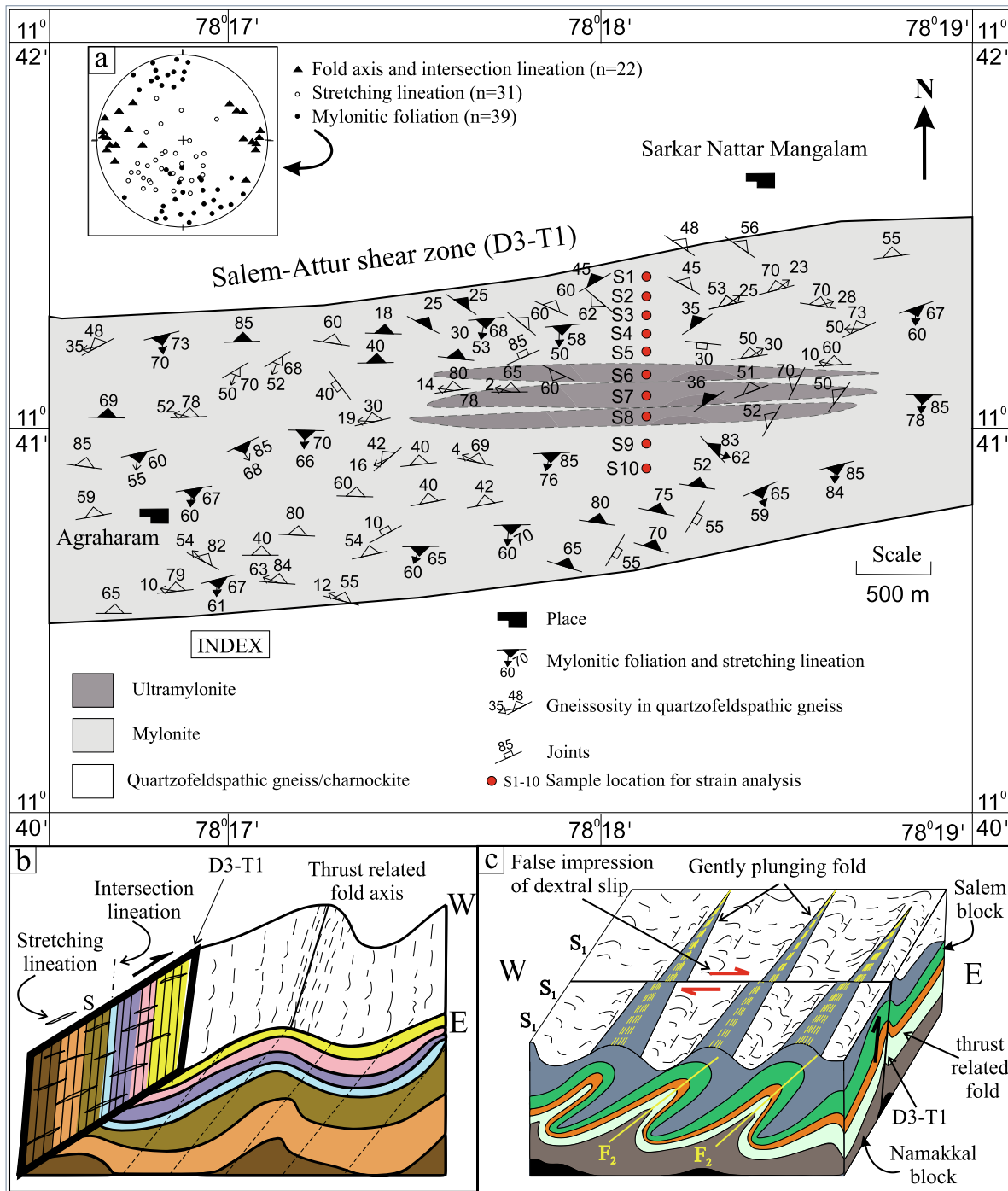


**Fig. 6.** Geological map of the Salem-Attur shear zone near Sarkar Nattar Mangalam. In the centre, thin bands of ultramylonite was mapped, pseudotachylite vein might be the parent rock for ultramylonite. (a) Stereoplot for mylonitic foliation, fold axis intersection lineation, and stretching lineation. The stretching lineations are at high angle to strike of the mylonitic foliation, fold axis and intersection lineations are at low angle; (b) An illustrative sketch explains, fold axis and intersection lineation remain subhorizontal while the stretching lineation is down-dip (S); (c) A false impression of dextral slip (red arrow) is produced due to intersection between the thrust (black arrow) and  $S_1$  fabric, thrust related fold is produced due to shortening across the thrust. (For interpretation of the references to color in this figure legend, the reader is referred to the web version of this article.)

2004; Mahan et al., 2006; Just et al., 2011). We carried out monazite analysis in the Cameca SX-FIVE Electron Probe Micro-Analyzer (with 5 WDS spectrometers including LLIF and LPET crystals) at the Department of Earth Sciences Indian Institute of Technology Bombay. The single point/average method was used to constrain the dates of the monazites domains (Montel et al., 1996). The age analyses were conducted at an accelerating voltage of 20 keV and a 200 nA prob current with 1  $\mu$ m beam diameter (Wawrzenitz et al., 2012). X-ray element

mapping was carried out for Ce, La, Y, Pb, Th, U in monazite was acquired with an accelerating voltage of 20 KeV, beam current of 100 nA and spatial resolution of 1–3  $\mu$ m/pixel with dwell times varying between 50 and 80 ms/pixel. Both natural and synthetic glass standards were used to calibrate for major and trace elements. PbMa, ThMa and UMb spectral lines were calibrated with crocoite (PbCrO<sub>4</sub>), Th glass (ThO<sub>2</sub>- 5 wt%) and U glass (UO<sub>2</sub>- 5 wt%) standards using two spectrometers for 240 s, 160 s and 160 s respectively using sub-counting

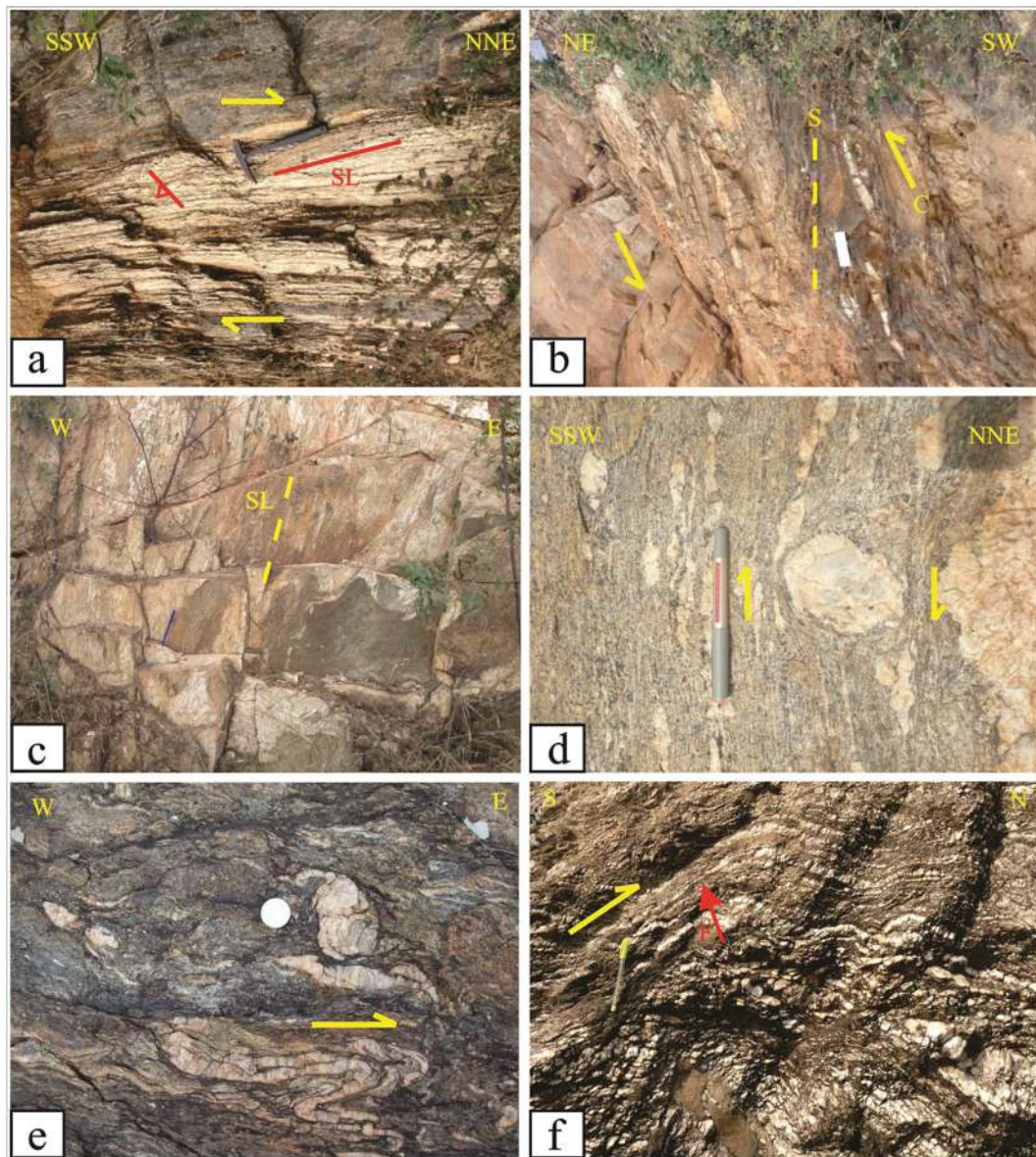


**Fig. 7.** (a) Vertical view,  $D_3-T_1$ , gentle, southerly dipping mylonitic foliation in quartzofeldspathic gneiss, with ductile slickenlines/stretching lineations (SL) indicating NNE vergence; (b) Vertical view  $D_3-T_1$ , steeply southerly dipping mylonitic foliation in quartzofeldspathic gneiss, S-C fabric shows top-to-NE vergence; (c) Vertical view,  $D_3-T_1$ , steep stretching lineation (SL) plunging to south on S-dipping mylonitic foliation; (d) Vertical view,  $D_3-T_1$ , feldspar porphyroclast shows N-NE vergence; (e) Horizontal view,  $D_3-T_2$ ,  $F_1$  parasitic folds have been reoriented to vertical attitude and give a false impression of dextral shearing; (f) Open upright nonplunging folds, developed in  $D_3-T_2$ , indicating that the fold axis (into the photograph) is at right angle to slip direction.

methodology (cf. Spear and Wark, 2009; Prabhakar, 2013). The total counts of PbMa were acquired in the exponential mode to better define the distantly located background positions (Jercinovic and Williams, 2005; Jercinovic et al., 2008; Spear and Wark, 2009; Goncalves et al., 2016). The matrix effects (ZAF) were reduced with X-PHI method (Merlet, 1992). The significant peak interference of ThM2-O4, ThM $\zeta$ 1, ThM $\zeta$ 2, YLC2, YLC3, LaLa on PbMa and ThMc, ThM3-N4 on UMB were corrected during quantification following the values given in Supplementary Table S1. More details on monazite dating protocol and interference corrections were outlined in Pant et al. (2009), Prabhakar (2013), Deshmukh et al. (2017) and Chatterjee et al. (2017). Detection limits were 100 ppm for Th, 110 ppm for U and 80 ppm for Pb. The spot age of individual analysis was computed using the formulae of Montel et al. (1996). If domains and/or mineral grains of a single age with the same amounts of initial Pb but different amounts of Th and U, have remained in a closed system, all analytical data will lie on an isochron with the slope 'm', and from 'm', the age is calculated (Suzuki and Kato,

2008). However, samples (sample –478, –470) in our study, the domains show mixed ages. We therefore used Isoplot (Version 4.14, Ludwig, 2012) to identify distinct age groups as suggested by Sambridge and Compston (1994) and Vlach (2010).

### 3.5. $^{40}\text{Ar}$ - $^{39}\text{Ar}$ geochronology

Hornblende and biotite were used for dating shearing events. Both minerals have low closure temperature for the K-Ar system (hornblende  $530 \pm 40$ ; Harrison, 1981; biotite,  $310 \pm 40$ , Harrison et al., 1985). We also used pseudotachylites produced from melting of the parent rock in fault zones (e.g., Kelley et al., 1994; Magloughlin et al., 2001; Warr et al., 2007; Sherlock et al., 2009). The newly-formed melt contains K, which then produces  $^{40}\text{Ar}^*$  on cooling. The Ar-isotopic clock is thus thought to be reset during frictional melting, as all radiogenic  $^{40}\text{Ar}^*$  is lost from the K-bearing minerals. The  $^{40}\text{Ar}$ - $^{39}\text{Ar}$  dating was done at the National Facility at  $^{40}\text{Ar}$ - $^{39}\text{Ar}$  Geo-thermochronology Lab in

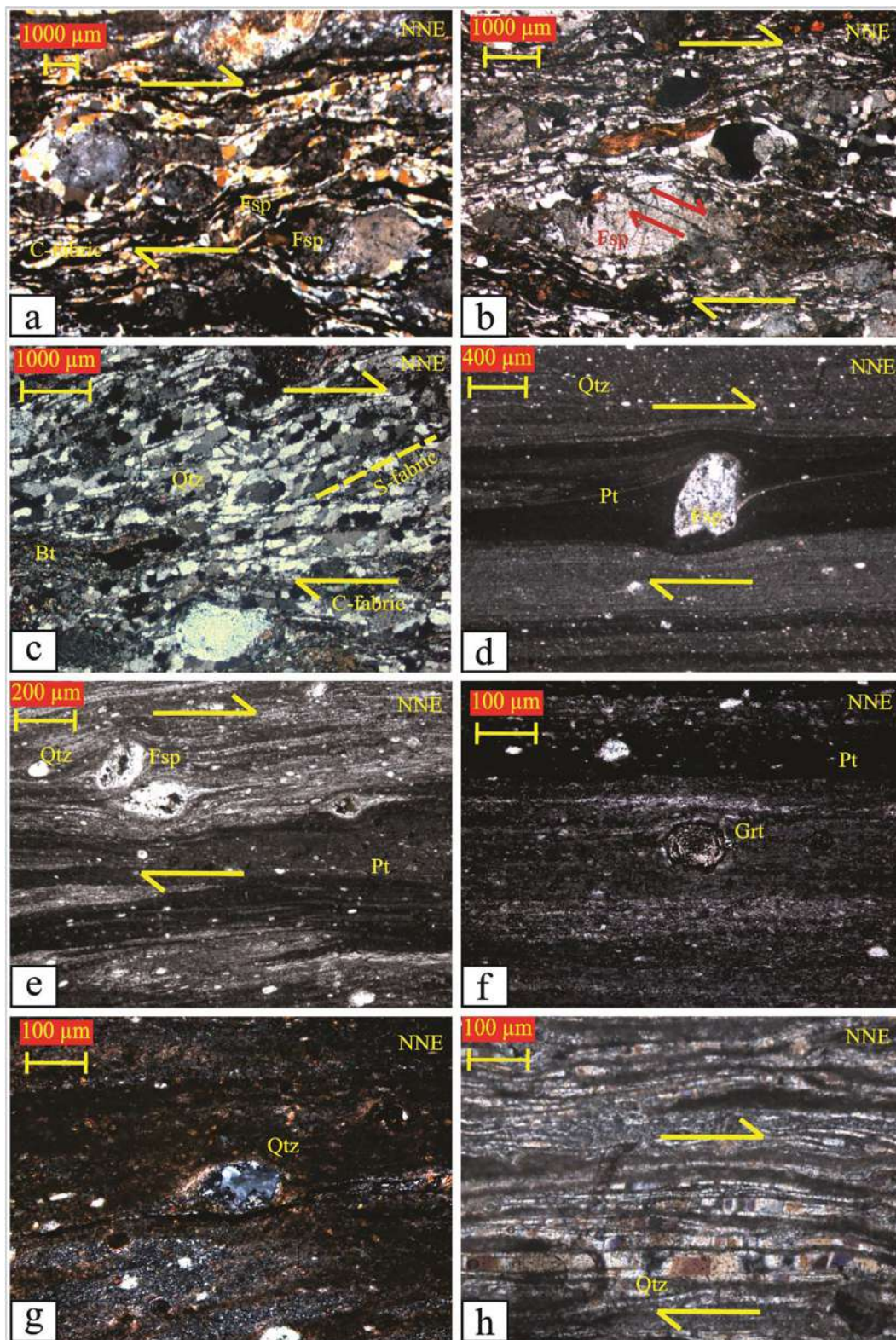


**Fig. 8.** (a) Quartzfeldspathic mylonites with feldspar (Fsp) porphyroclasts; (b) Low angle intragranular fault, in feldspar (Fsp) porphyroclasts, with synthetic shear; (c) S-C fabric, quartz grains (Qtz) with rotation recrystallization, biotite (Bt) along C-fabric; (d) Delta geometry of feldspar (Fsp) porphyroclasts in ultramylonite; (e-f) Ultramylonite with sigmoidal porphyroclasts; (g) Embayed quartz (Qtz) clasts in ultramylonite; (h) Monomineralic quartz ribbons indicating rotation recrystallization.

**RGN Plot of porphyroclasts**

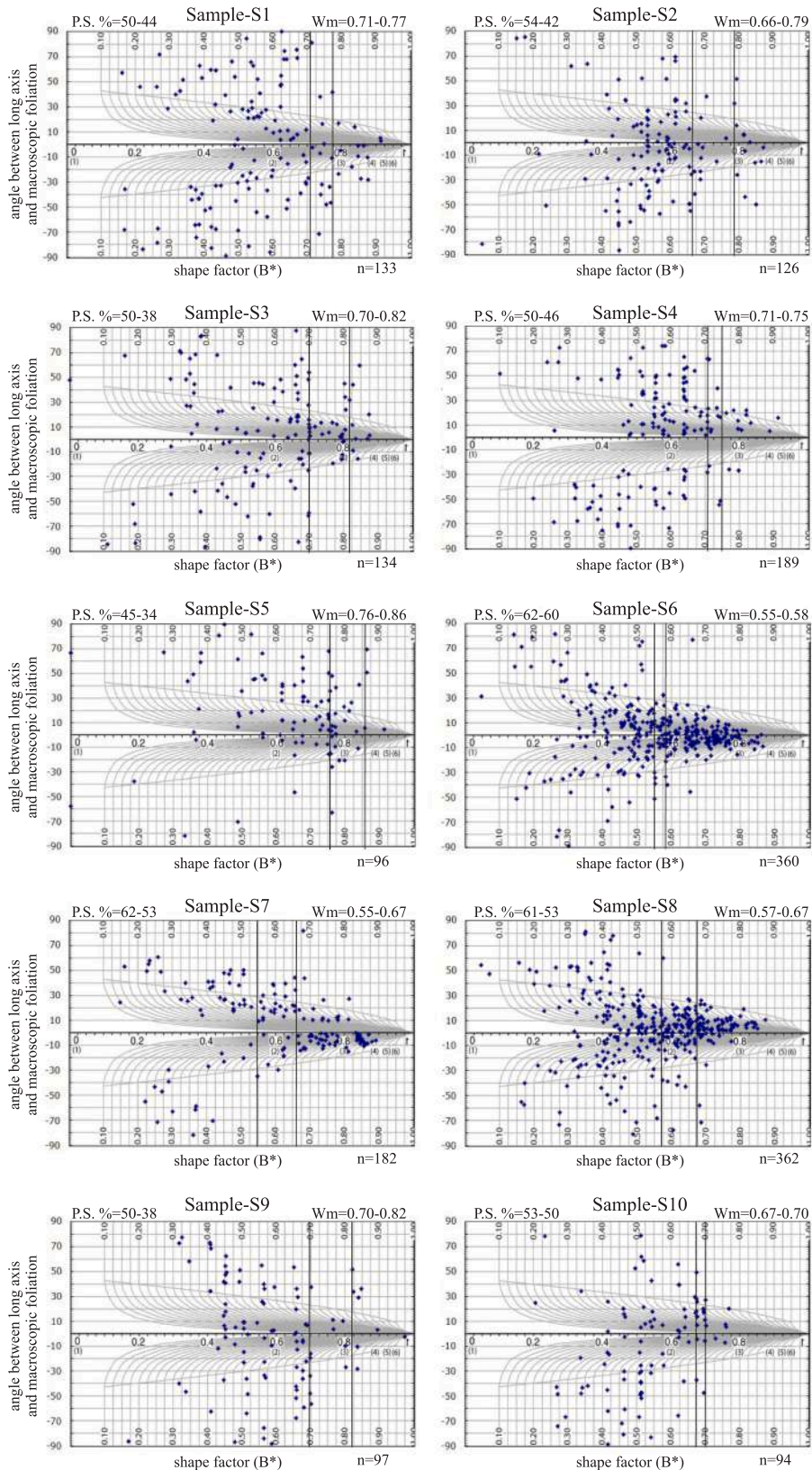


**Fig. 9.** Rigid grain net plot of rotated porphyroclasts from the mylonite-ultramylonite of the Salem-Attur shear zones, D<sub>3</sub>-T<sub>1</sub>. Each plot corresponds to one sample and sample locations are shown in Fig. 6. The XZ-sections were used to measure the angle between the long axis of the porphyroclast and C-plane. Sample number, percentage of pure shear (P.S.) and Wm (mean kinematic vorticity number) are mentioned at the top of each figure. (N) Number of grains counted is mentioned at the bottom right corner of the plot.  $B^* = (\text{long axis}^2 - \text{short axis}^2) / (\text{long axis}^2 + \text{short axis}^2)$  Jessup et al., 2007; P.S. after Law et al., 2004. Wm defines the line from where the theta angle sharply rises above the Rc value (for detail see the text).

the Department of Earth Sciences, Indian Institute of Technology Bombay. Rock chips of about 20–25 g were cut from the hand specimens to avoid veins and weathered material. The chips were crushed in an agate mortar and sieved and the large grains collected using heavy

liquid separation (sodium polytungstate water solution of specific gravity 2.56). The grains were then cleaned in deionized water in an ultrasonic bath and then heated in an oven to dry. About 0.2 g of each sample was packed in aluminum capsules. The Minnesota hornblende

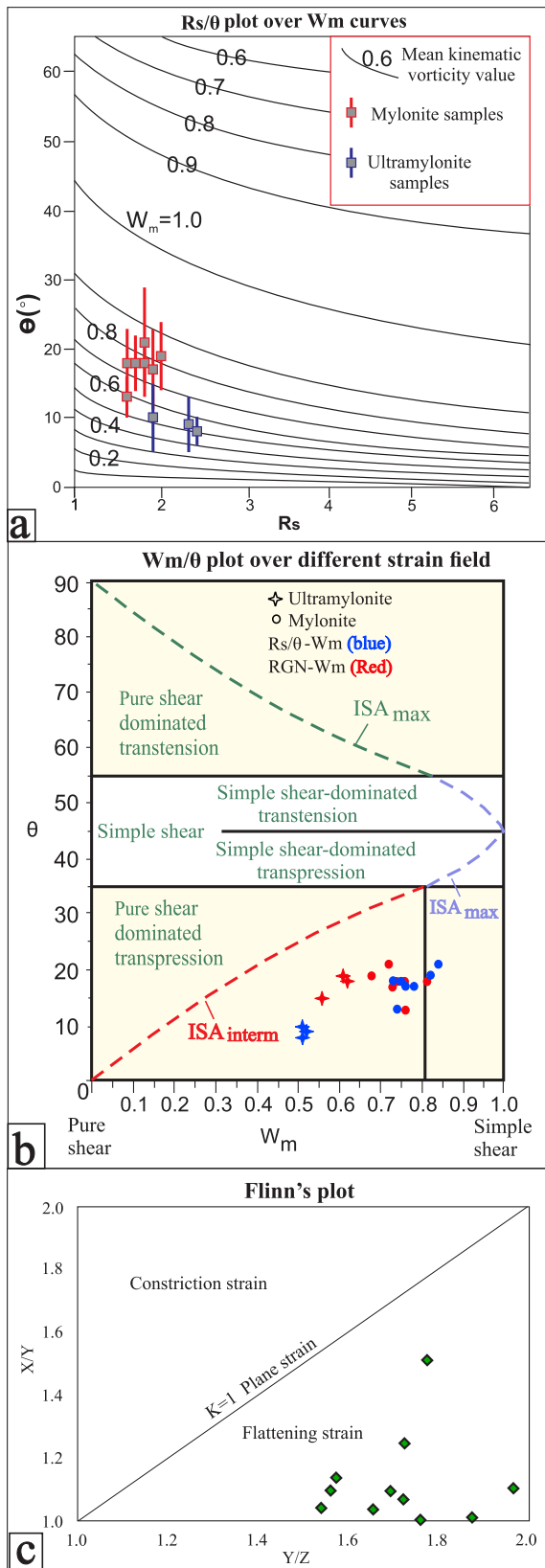


**Fig. 10.** (a)  $R_s$  vs  $S^\circ C$  angle plot on  $W_m$  curves (after Ramsay and Huber, 1983; Fossen and Tikoff, 1993); (b)  $\theta$  vs.  $W_m$  plot (Tikoff and Fossen, 1995).  $W_m$  was computed from rigid grain net analysis in Fig. 9.  $\theta$  is the measure of average  $S^\circ C$  angle in thin section and  $W_m$  is the mean kinematic vorticity number. See Table 1, for the result; (c) Flinn plot, X/Y and Y/Z graph indicates flattening.

reference material (MMhb-1) of age  $523.1 \pm 2.6$  Ma (Renne et al., 1998) and high purity  $CaF_2$  and  $K_2SO_4$  salts were used as monitor samples. High purity nickel wires were placed in both samples to monitor the neutron fluence variation, which was typically  $\sim 5\%$ . The aluminum capsules were kept in a 0.5 mm-thick cadmium cylinder and irradiated in the light-water moderated CIRUS reactor at the Bhabha Atomic Research Centre (BARC), Mumbai, for  $\sim 100$  h. The irradiated samples were repacked in aluminum foil and loaded on the extraction unit of a Thermo Fisher Scientific noble gas preparation system. Argon was extracted in a series of steps up to  $1600^\circ C$  in an electrically heated ultra-high vacuum furnace. After purification using Ti-Zr getters, the argon released in each step was measured with a Thermo Fisher ARGUS mass spectrometer. The mass spectrometer is equipped with five Faraday cups fitted with  $1011 \Omega$  resistors. Interference corrections were made. The irradiation parameter  $J$  for each sample was corrected for neutron flux variation using the activity of the irradiated nickel wires (Supplementary Table S2).

## 4. Result

### 4.1. Lithology and deformational history of the Salem-Namakal blocks

#### 4.1.1. Lithology

Quartzofeldspathic gneiss, mafic granulite and charnockite were the main lithologies of the Salem-Namakal blocks. The quartzofeldspathic gneiss contained alternate orthopyroxene, hornblende and biotite-rich melanosome, and garnet-quartz-plagioclase-alkali feldspar-rich leucosome (Fig. 3a and b). Garnet in the leucosome was mantled by biotite (Fig. 3b inset, sample from Salem block). These gneisses graded to pyroxene-hornblende-biotite gneiss due to enrichment of melanosome parts. The quartzofeldspathic gneiss enclosed thin layers of chert, BIF and mafic granulite (Mg) which were stretched to form boudins (Fig. 3a inset). The next abundant lithounit was the mafic granulite that contained plagioclase-quartz-rich enderbite layers alternating with pyroxene-garnet-hornblende-biotite-rich layers (Fig. 3c). Garnet corona was developed around clino-orthopyroxenes and garnet (Fig. 3d inset) in the Salem block (Kanjamalai, Kusumalai and Godumalai; Fig. 3d). However, in the Namakal block, garnet was mantled by orthopyroxene corona, (Belukurichi, Valayapatti and Sittampundi areas, Fig. 3e). In a few instance, the primary magmatic layers were preserved in the mafic granulite (east of Kanjamalai hill, Fig. 1), being defined by cumulate layers of magnetite, pyroxene and plagioclase minerals (Fig. 3c inset). The mafic granulite retrograded to amphibolite and a thick amphibolite unit was mapped at Moyerpalayam (Fig. 2 for location, Fig. 3f for microphotograph). In the study area, large-scale charnockite plutons formed high hills at several places (Biligirirangan, Shevroy, Jarugumalai and Kolimalai, Fig. 1). These were characterized by a coarse grained assemblage of quartz, feldspar, hypersthene, garnet porphyroblasts and carbonate minerals (Fig. 3g and inset). Further, several other magmatic intrusives associated with the blocks, e.g., slivers of anorthosite-mafic granulite-eclogitic rocks at Sittampundi, dunite-pyroxenite-shonkinite at Nagarmalai and syenite at Attur (Fig. 1). Dolerite and pink granite dykes intruded along NNW-SSE and NNE-SSW fractures. Pseudotachylite veins injected along faults and fractures, these contained albite microlites and quartz-feldspar clasts within dark glassy matrix. The thickest vein was mapped along Gangavalli fault (Fig. 1 for location, 3 h for outcrop photo, 3 h inset for petrography). The Sankaridurg granite pluton was located to the southwest of the area (Fig. 2) and associated with coeval granite-pegmatite veins that intruded into the pre-existing foliation and fractures in the surrounding rocks.

### 4.2. Deformational history

#### 4.2.1. $D_1$ deformation

The Salem-Namakal blocks were characterized by four stages of deformation. The  $D_1$  deformation included NE-SW trending isoclinal

**Table 1**

Vorticity of freely rotating porphyroclasts (through RGN) and recrystallized grains (Rs/θ) of mylonite and ultramylonite samples from Sarkar Nattar Mangalam area (N11°40'46.71", E78°18'04.95").

Sample No.	Vorticity (W <sub>m</sub> )		S-C angle (θ <sup>0</sup> )	% of pure shear(RGN), Range and avg.	Sample type
	Porphyroclasts (RGN, range, avg.)	Recrystallized grains (Rs/θ)			
S1	(0.71–0.77)0.74	0.75	18	(44–50)47	mylonite
S2	(0.66–0.79)0.72	0.84	21	(42–54)48	mylonite
S3	(0.70–0.82)0.76	0.73	18	(38–50)44	mylonite
S4	(0.71–0.75)0.73	0.76	17	(46–50)48	mylonite
S5	(0.76–0.86)0.81	0.78	17	(34–45)40	mylonite
S6	(0.55–0.58)0.56	0.51	10	(60–62)61	ultramylonite
S7	(0.55–0.67)0.61	0.51	8	(53–62)58	ultramylonite
S8	(0.57–0.67)0.62	0.52	9	(53–61)57	ultramylonite
S9	(0.70–0.82)0.76	0.74	13	(38–50)44	mylonite
S10	(0.67–0.70)0.68	0.82	19	(50–53)52	mylonite

recumbent F<sub>1</sub> folds, which were developed on the lithological layering (S<sub>0</sub>) defined by metachert and BIF layers in quartzofeldspathic gneiss and cumulate layers in mafic granulite (Fig. 3c inset, Fig. 4a-b). The folds were extremely flattened to produce intrafolial and boudinaged folds. The F<sub>1</sub> was associated with a penetrative horizontal axial-planar gneissosity (S<sub>1</sub>) that cut across the bedding at the hinge zone and remained parallel to the limbs. The granulite facies minerals such as garnet, pyroxene, and plagioclase in mafic granulite and orthopyroxene, plagioclase and garnet in charnockite were developed parallel to the S<sub>1</sub> fabric (Fig. 4a inset) which implied that the granulite facies metamorphism (M<sub>1</sub>) was syntectonic with F<sub>1</sub> folding. Further, quartzofeldspathic leucosomes were produced parallel to the S<sub>1</sub> suggesting that the rocks melted during M<sub>1</sub> metamorphism (Fig. 4e). We inferred a PT of 7 kb/800 °C for the M<sub>1</sub> metamorphism from garnet + clinopyroxene + plagioclase assemblage (e.g., Harley, 1989).

#### 4.2.2. D<sub>2</sub> deformation

The D<sub>2</sub> deformation affected the S<sub>0</sub> and S<sub>1</sub> fabrics producing NE-SW trending, open to tight and upright to NW inclined F<sub>2</sub> folds indicating buckling origin (Fig. 4b, c and e). Parasitic folds, cleavage refraction, compositional band boudins, and folded boudins were associated with F<sub>2</sub> folds. Coaxial folding between F<sub>1</sub> and F<sub>2</sub> produced a ubiquitous type-3 fold interference pattern (Ramsay, 1967; Fig. 4b). The recumbent/reclined F<sub>1</sub> folds were reoriented to different attitudes; the hinge zone of the F<sub>2</sub> folds contained the reclined folds and the limb region had inclined/upright folds. The S<sub>2</sub> fabric was developed in form of crenulations and shear bands (C-fabric) parallel to the axial plane of the F<sub>2</sub> fold (Figs. 4c, S1a) and the S<sub>1</sub> fabric was transposed parallel to S<sub>2</sub>. Melting along the shear band produced quartzofeldspathic leucosome (Fig. 4e). Vertical to subvertical flow was indicated by sub vertical stretching lineation (Fig. S1C), deflection of the S<sub>1</sub> fabric (Fig. 4c), rotation of quartzofeldspathic aggregate (Fig. 4d) and oblique S fabric between C-domains (Fig. S1a and d). Microlithons comprising stack of small scale F<sub>2</sub> folds were developed between two consecutive shear bands and had similar kinematics.

The NE-SW trending large-scale F<sub>2</sub> folds were mapped at Belukurichi, and interpreted from stereoplot at Kandashram and Kanjamalai (Fig. 2). Stereoplots of S<sub>1</sub> fabric indicated girdle pattern with gentle to moderately plunging F<sub>2</sub> fold axis (β-axis) in NE, W and ENE trend (Fig. 2c, d). The D<sub>2</sub> shear zones were mapped along the limbs of large-scale F<sub>2</sub> folds. Along the shear zone, F<sub>1</sub> and F<sub>2</sub> fold axes were reoriented to near vertical attitude (Fig. S1b). As a result, the F<sub>1</sub> and F<sub>2</sub> folds were converted to sheath folds producing circular to elliptical outcrops within quartzofeldspathic gneiss (Fig. 4c inset). Several magmatic intrusive rocks, namely basic-ultrabasic-shonkinite at Salem, syenite-gabbro at Attur and anorthosite at Sittampundi were present along the D<sub>2</sub> shear zones. These intrusives were elongated parallel to the S<sub>2</sub> strike and contained coplanar magmatic and solid-state deformation fabric. This suggested that the intrusion was probably

syntectonic with D<sub>2</sub> deformation. Petrographic study of the syenite indicated the dominance of K-feldspar with subordinate amount of plagioclase and quartz. The minerals had undergone crystal plastic deformation and dynamic recrystallization. Plagioclase grains contained kinks, undulose extinction and grain boundary migration recrystallization (Fig. 4f) and quartz grains were marked by chessboard extinction (Fig. 4g). The features suggested a PT of 6 kb/700–800 °C, for D<sub>2</sub> shearing (e.g., Pryer, 1993; Kruhl, 1996; Rosenberg and Stunitz, 2003; Passchier and Trouw, 2005). This might occur in the upper amphibolite to granulite facies.

#### 4.2.3. D<sub>3</sub> deformation

The D<sub>3</sub> deformation developed NW-SE to E-W trending F<sub>3</sub> folds (Fig. 4h), crenulation cleavages and axial planar brittle shear over S<sub>1–2</sub> fabrics. As the S<sub>1</sub> surfaces had a variable orientation due to F<sub>2</sub> folding, F<sub>3</sub> fold axes acquired variable plunge depending on the attitude of the S<sub>1</sub> surface. Further, type-1 and type-2 fold interference patterns were produced due to superposition of F<sub>3</sub> on F<sub>2</sub> and F<sub>1</sub> folds respectively (Fig. 5a, b). Along F<sub>3</sub> cleavage, hornblende, biotite and muscovites were crystallized due to retrograde metamorphism of granulites (S<sub>3</sub>, Fig. 4h inset, Fig. S1e).

Large-scale F<sub>3</sub> folding in the area was mapped from the variation of orientation of the S<sub>1–2</sub> fabrics. Variation of S<sub>1–2</sub> strike from ENE-WSW at Salem to N-S at Moyerpalayam and NW-SE at Valayapatti was due to large-scale F<sub>3</sub> fold (Fig. 2). Several large-scale D<sub>3</sub>-retrograde shear zones were mapped. These included the Salem-Attur shear (D<sub>3</sub>-T<sub>1–3</sub>) and Valayapatti shear zones (D<sub>3</sub>-T<sub>4</sub>, 'T' stands for thrusting). NE-SW striking D<sub>2</sub> shear zones and fabric were at an angle to D<sub>3</sub> shear zones (see near Namakkal and Sarkar Nattar Mangalam, Fig. 2). Mafic granulite overthrust the granite gneiss along the NW-SE striking Valayapatti shear zone (D<sub>3</sub>-T<sub>4</sub>, Fig. S1f). The S<sub>1</sub> fabric was folded by large-scale NW plunging folds due to shortening across the thrust (west of Namakkal, Fig. 2e). The thrust was characterized by retrogression of garnet and pyroxene to hornblende. Down-dip stretching lineation defined by hornblende and biotite minerals was produced on southwesterly dipping mylonitic foliation. Rotated porphyroclasts and asymmetric folds indicated top-to-NNE vergence thrust kinematics (Fig. S1g).

#### 4.2.4. D<sub>4</sub> deformation

The D<sub>4</sub> deformation included NE-SW and NW-SE striking strike-slip faults, and WNW-ESE to NW-SE striking normal faults (rose diagrams in Fig. 2f, g). The NE-SW striking Gangavalli sinistral strike-slip fault hosts thick pseudotachylite veins (Fig. 1). In one instance a pink granite pluton that contained large xenoliths of D<sub>3</sub> mylonite was fractured along Gangavalli fault and injected by pseudotachylite veins (Fig. 3h). The relationship suggested that the intrusion of pink granite was between D<sub>3</sub> shearing and strike-slip brittle faulting. Apart from that there were several small-scale strike-slip shears with subhorizontal slickenlines, some of them host pseudotachylite veins (Fig. 5c, d). The

**Table 2**  
Zircon U-Pb SHRIMP data (2σ error of the mean of 0.94%) of sample TKB-18, 19 and 20 (N11°38'04.11", E78°14'25.20"), TKB-21 (N11°36'45.92", E78°33'25.45") and TKB-22 (N11°33'50.29", E78°02'45.02").

Spot Name	f206 (%)	U (ppm)	Th	Th/U	( <sup>238</sup> U/ <sup>206</sup> Pb) <sub>total</sub> (± 1s abs)	( <sup>207</sup> Pb/ <sup>206</sup> Pb) <sub>total</sub>	( <sup>238</sup> U/ <sup>206</sup> Pb) <sub>204</sub>	( <sup>207</sup> Pb/ <sup>206</sup> Pb) <sub>204</sub>	<sup>206</sup> Pb/ <sup>238</sup> U Age (± 1s Ma)	<sup>207</sup> Pb/ <sup>206</sup> Pb Age
TKB-18-C-1	0.03	135	67	0.51	1.97867 ± 0.02943	0.17933 ± 0.00145	1.97924 ± 0.02944	0.17907 ± 0.00146	2636 ± 32	2644 ± 14
TKB-18-C-2	0.06	195	91	0.48	2.09082 ± 0.02906	0.16571 ± 0.00115	2.09204 ± 0.02909	0.16520 ± 0.00117	2519 ± 29	2510 ± 12
TKB-18-C-4	0.04	417	352	0.87	2.06614 ± 0.02524	0.17932 ± 0.00080	2.06693 ± 0.02525	0.17897 ± 0.00081	2606 ± 27	2643 ± 7
TKB-18-C-5	0.11	426	413	1	1.99673 ± 0.02492	0.17979 ± 0.00128	1.99897 ± 0.02495	0.17879 ± 0.00129	2615 ± 27	2642 ± 12
TKB-18-C-6	0.05	152	77	0.52	1.99906 ± 0.02858	0.17929 ± 0.00123	2.00009 ± 0.02860	0.17883 ± 0.00125	2614 ± 31	2642 ± 12
TKB-18-C-7	0.1	359	320	0.92	2.06841 ± 0.02621	0.18035 ± 0.00079	2.07052 ± 0.02624	0.17944 ± 0.00081	2540 ± 27	2648 ± 7
TKB-18-C-8	0.22	287	200	0.72	2.01198 ± 0.02660	0.18190 ± 0.00102	2.01647 ± 0.02667	0.17991 ± 0.00108	2596 ± 28	2652 ± 10
TKB-18-C-9	0.07	247	211	0.88	2.18049 ± 0.02949	0.17034 ± 0.00112	2.18204 ± 0.02952	0.16970 ± 0.00114	2432 ± 27	2555 ± 11
TKB-18-C-10	0.06	212	119	0.58	2.11928 ± 0.02920	0.16862 ± 0.00109	2.12059 ± 0.02922	0.16807 ± 0.00111	2490 ± 28	2539 ± 11
TKB-18-C-11	-	326.96	90	3.75	2.20526 ± 0.03574	0.163922 ± 0.0016328	2.20481 ± 0.035739	0.16411 ± 0.001643	2411 ± 33	2498 ± 17
TKB-18-C-12	0.25	266	149	0.58	2.01321 ± 0.02825	0.17695 ± 0.00133	2.01820 ± 0.02834	0.16475 ± 0.00142	2594 ± 30	2604 ± 14
TKB-18-C-13	2.53	488	396	0.84	3.43140 ± 0.04281	0.19177 ± 0.00210	3.52050 ± 0.04422	0.16920 ± 0.00251	1612 ± 18	2550 ± 25
TKB18-R-1	-	50	64	1.33	2.09132 ± 0.06457	0.16506 ± 0.00203	2.08868 ± 0.06451	0.16619 ± 0.00211	2522 ± 64	2520 ± 21
TKB18-R-2	0.28	64	79	1.28	2.31343 ± 0.06889	0.16679 ± 0.00197	2.31999 ± 0.06911	0.16427 ± 0.00213	2310 ± 58	2500 ± 22
TKB18-R-3	0.07	47	75	1.63	2.37649 ± 0.07220	0.16787 ± 0.00214	2.37814 ± 0.07226	0.16725 ± 0.00218	2263 ± 58	2530 ± 22
TKB18-R-4	2.37	42	8	0.21	2.25903 ± 0.07267	0.17640 ± 0.00292	2.31386 ± 0.07513	0.15532 ± 0.00492	2316 ± 63	2405 ± 54
TKB18-R-5	0.17	38	46	1.25	2.17957 ± 0.06740	0.16762 ± 0.00209	2.18322 ± 0.06753	0.16612 ± 0.00220	2431 ± 63	2519 ± 22
TKB18-R-6	0.07	44	63	1.5	2.49687 ± 0.07554	0.15881 ± 0.00204	2.49857 ± 0.07560	0.15820 ± 0.00209	2170 ± 56	2437 ± 22
TKB18-R-7	0.11	45	63	1.45	2.1387697 ± 0.0647601	0.16771 ± 0.00309	2.14112 ± 0.064842	0.16673 ± 0.003131	2471 ± 62	2525 ± 32
TKB18-R-8	0.04	39	75	1.99	2.19934 ± 0.06914	0.17059 ± 0.00229	2.20021 ± 0.06918	0.17024 ± 0.00232	2415 ± 63	2560 ± 23
TKB18-R-9	0.81	80	14	1.16	1.95114 ± 0.06608	0.17427 ± 0.00195	1.96710 ± 0.06669	0.16703 ± 0.00243	2650 ± 74	2528 ± 24
TKB18-R-10	0.09	18	14	0.79	2.12386 ± 0.07733	0.16804 ± 0.00347	2.12582 ± 0.07743	0.16722 ± 0.00356	2485 ± 75	2530 ± 36
TKB18-R-11	2.65	46	152	3.38	2.08572 ± 0.06493	0.19891 ± 0.00428	2.14245 ± 0.06710	0.17529 ± 0.00535	2469 ± 64	2609 ± 51
TKB18-R-12	0.14	49	182	3.84	2.11565 ± 0.06508	0.16786 ± 0.00210	2.11854 ± 0.06519	0.16665 ± 0.00219	2492 ± 64	2524 ± 22
TKB18-R-13	0.11	59	71	1.26	2.15171 ± 0.06438	0.16312 ± 0.00183	2.15401 ± 0.06446	0.16217 ± 0.00189	2458 ± 61	2478 ± 20
TKB-19-C-1	0.58	844	74	0.09	2.19835 ± 0.02634	0.17048 ± 0.00056	2.21106 ± 0.02651	0.16535 ± 0.00067	2405 ± 24	2511 ± 7
TKB-19-C-2	0.31	998	120	0.12	2.10526 ± 0.02503	0.16926 ± 0.00095	2.11186 ± 0.02514	0.16647 ± 0.00111	2499 ± 25	2522 ± 11
TKB-19-C-3	1.81	202	59	0.3	1.86765 ± 0.02927	0.18686 ± 0.00198	1.90204 ± 0.03014	0.17074 ± 0.00290	2724 ± 35	2565 ± 28
TKB-19-C-4	0.23	273	112	0.43	2.86738 ± 0.06820	0.12853 ± 0.00401	2.87413 ± 0.06837	0.12646 ± 0.00404	1925 ± 40	2049 ± 56
TKB-19-C-5	0.08	71	101	1.47	2.15768 ± 0.03707	0.16638 ± 0.00187	2.15939 ± 0.03712	0.16567 ± 0.00192	2453 ± 35	2514 ± 19
TKB-19-C-6	0.31	165	54	0.34	2.11864 ± 0.02987	0.17018 ± 0.00121	2.12531 ± 0.02999	0.16738 ± 0.00132	2486 ± 29	2532 ± 13
TKB-19-C-7	0.51	876	127	0.15	2.18920 ± 0.02614	0.17274 ± 0.00051	2.20031 ± 0.02629	0.16823 ± 0.00059	2415 ± 24	2540 ± 6
TKB-19-C-8	1.37	121	30	0.26	2.18101 ± 0.03258	0.18756 ± 0.00156	2.21121 ± 0.03378	0.17538 ± 0.00326	2405 ± 31	2610 ± 31
TKB-19-C-9	-	171	90	0.55	3.79163 ± 0.38610	0.11369 ± 0.00787	3.78948 ± 0.38588	0.11419 ± 0.00787	1510 ± 137	1867 ± 124
TKB-19-C-10	0.32	2132	84	0.04	2.11856 ± 0.02583	0.17093 ± 0.00056	2.12544 ± 0.02592	0.16804 ± 0.00059	2486 ± 25	2538 ± 6
TKB-19-C-11	0.09	62	90	1.5	2.17666 ± 0.03888	0.16591 ± 0.00197	2.17857 ± 0.03893	0.16513 ± 0.00202	2435 ± 36	2509 ± 21
TKB-19-C-12	0.62	97	186	1.98	2.14587 ± 0.03387	0.17109 ± 0.00162	2.15932 ± 0.03420	0.16553 ± 0.00200	2453 ± 32	2513 ± 20
TKB-19-C-13	0.27	1275	137	0.11	2.04715 ± 0.02453	0.16864 ± 0.00060	2.05263 ± 0.02461	0.16626 ± 0.00066	2558 ± 25	2520 ± 7
TKB-19-C-14	0.35	1355	75	0.06	2.15037 ± 0.02530	0.16952 ± 0.00041	2.15786 ± 0.02541	0.16643 ± 0.00058	2425 ± 24	2520 ± 6
TKB-19-C-15	0.22	947	120	0.13	2.35753 ± 0.02803	0.16683 ± 0.00049	2.36279 ± 0.02811	0.16485 ± 0.00063	2275 ± 23	2506 ± 6
TKB-19-C-16	0.14	1002	133	0.14	2.14675 ± 0.02553	0.16728 ± 0.00049	2.14976 ± 0.02557	0.16603 ± 0.00051	2462 ± 24	2518 ± 5
TKB-19-C-17	0.2	1037	130	0.13	2.29609 ± 0.02720	0.16455 ± 0.00078	2.30062 ± 0.02726	0.16280 ± 0.00080	2327 ± 23	2485 ± 8
TKB-19-C-18	0.03	881	113	0.13	2.14115 ± 0.02559	0.16752 ± 0.00055	2.14176 ± 0.02560	0.16727 ± 0.00056	2470 ± 25	2530 ± 6
TKB-19-C-19	0.21	1085	125	0.12	2.25372 ± 0.02671	0.16717 ± 0.00048	2.25856 ± 0.02677	0.16526 ± 0.00051	2363 ± 23	2510 ± 5
TKB-19-C-20	0.36	972	129	0.14	2.17729 ± 0.02609	0.17084 ± 0.00055	2.18510 ± 0.02628	0.16766 ± 0.00106	2429 ± 24	2534 ± 11
TKB-19-R-21	0.04	263	186	0.73	2.23876 ± 0.02950	0.16445 ± 0.00194	2.23955 ± 0.02952	0.16413 ± 0.00195	2380 ± 26	2499 ± 20
TKB-19-C-22	0.19	337	414	1.27	1.213657 ± 0.24645	0.05663 ± 0.00116	12.15923 ± 0.24712	0.05512 ± 0.00134	509 ± 10	417 ± 54
TKB-19-C-23	0.08	1418	211	0.15	2.16632 ± 0.02547	0.16652 ± 0.00065	2.16807 ± 0.02549	0.16580 ± 0.00070	2445 ± 24	2516 ± 7
TKB-19-C-24	0.29	93	44	0.49	9.88644 ± 0.24351	0.07117 ± 0.00230	9.91540 ± 0.24480	0.06874 ± 0.00270	619 ± 15	891 ± 81

Spot Name	f206 (%)	U (ppm)	Th	Th/U	$(^{238}\text{U}/^{206}\text{Pb})_{\text{total}}$ ( $\pm 1\text{ s abs}$ )	$(^{207}\text{Pb}/^{206}\text{Pb})_{\text{total}}$	$(^{238}\text{U}/^{206}\text{Pb})_{204}$	$(^{207}\text{Pb}/^{206}\text{Pb})_{204}$	$^{206}\text{Pb}/^{238}\text{U}$ Age ( $\pm 1\text{ s Ma}$ )	$^{207}\text{Pb}/^{206}\text{Pb}$ Age
TKB20-H-1	0.06	2871	454	0.16	2.06961 $\pm$ 0.02406	0.16870 $\pm$ 0.00027	2.07092 $\pm$ 0.02408	0.16814 $\pm$ 0.00028	2540 $\pm$ 24	2539 $\pm$ 3
TKB20-H-2	0.35	1081	253	0.24	2.05476 $\pm$ 0.02441	0.17336 $\pm$ 0.00047	2.06199 $\pm$ 0.02450	0.17023 $\pm$ 0.00052	2549 $\pm$ 25	2560 $\pm$ 5
TKB20-H-3	0.02	883	277	0.32	2.12838 $\pm$ 0.02547	0.16978 $\pm$ 0.00052	2.12880 $\pm$ 0.02548	0.16960 $\pm$ 0.00052	2482 $\pm$ 25	2554 $\pm$ 5
TKB20-H-4	0.54	349	142	0.42	2.13889 $\pm$ 0.05884	0.16762 $\pm$ 0.00128	2.15057 $\pm$ 0.05918	0.16277 $\pm$ 0.00137	2462 $\pm$ 56	2485 $\pm$ 14
TKB20-L-1	–	272	121	0.46	4.11342 $\pm$ 0.15362	0.10852 $\pm$ 0.00753	4.11203 $\pm$ 0.15357	0.10882 $\pm$ 0.00753	1403 $\pm$ 47	1780 $\pm$ 126
TKB20-L-3	0.03	402	83	0.21	12.13987 $\pm$ 0.33425	0.05776 $\pm$ 0.00101	12.14351 $\pm$ 0.33437	0.05752 $\pm$ 0.00104	510 $\pm$ 40	511 $\pm$ 40
TKB20-L-4	0.53	373	405	1.12	8.40221 $\pm$ 0.25520	0.06291 $\pm$ 0.00182	8.44737 $\pm$ 0.25725	0.05855 $\pm$ 0.00256	721 $\pm$ 21	551 $\pm$ 95
TKB20-L-5	9.64	625	1271	2.1	10.19910 $\pm$ 0.28823	0.17152 $\pm$ 0.00899	11.28768 $\pm$ 0.35745	0.08909 $\pm$ 0.01575	547 $\pm$ 17	1406 $\pm$ 339
TKB20-L-6	0.15	250	78	0.32	10.89347 $\pm$ 0.30142	0.06325 $\pm$ 0.00121	10.91009 $\pm$ 0.30200	0.06200 $\pm$ 0.00136	565 $\pm$ 15	674 $\pm$ 47
TKB20-L-7	0.02	65	62	0.97	1.83263 $\pm$ 0.05436	0.20761 $\pm$ 0.00185	1.83299 $\pm$ 0.05438	0.20744 $\pm$ 0.00185	2807 $\pm$ 68	2886 $\pm$ 15
TKB20-L-8	0.56	802	140	0.18	10.66350 $\pm$ 0.56369	0.07548 $\pm$ 0.00787	10.72358 $\pm$ 0.56704	0.07081 $\pm$ 0.00799	575 $\pm$ 29	952 $\pm$ 231
TKB20-L-9	0.14	200	107	0.55	2.46262 $\pm$ 0.16359	0.16623 $\pm$ 0.00167	2.46603 $\pm$ 0.16382	0.16500 $\pm$ 0.00172	2194 $\pm$ 124	2508 $\pm$ 18
TKB20-L-10	0.46	179	378	2.18	11.15073 $\pm$ 0.31227	0.06454 $\pm$ 0.00311	11.20199 $\pm$ 0.31423	0.06079 $\pm$ 0.00339	551 $\pm$ 15	632 $\pm$ 120
TKB20-L-11	0.12	56	216	3.99	2.13657 $\pm$ 0.06485	0.16704 $\pm$ 0.00197	2.13913 $\pm$ 0.06495	0.16598 $\pm$ 0.00204	2473 $\pm$ 62	2517 $\pm$ 21
TKB21-1	0.01	344	136	0.41	3.00838 $\pm$ 0.08274	0.11305 $\pm$ 0.00074	3.00860 $\pm$ 0.08275	0.11299 $\pm$ 0.00074	1850 $\pm$ 44	1848 $\pm$ 12
TKB21-2	0.02	273	94	0.36	2.08804 $\pm$ 0.05768	0.16939 $\pm$ 0.00084	2.08848 $\pm$ 0.05770	0.16920 $\pm$ 0.00084	2522 $\pm$ 58	2550 $\pm$ 8
TKB21-3	0.04	146	95	0.67	2.13344 $\pm$ 0.06067	0.16540 $\pm$ 0.00133	2.13432 $\pm$ 0.06070	0.16504 $\pm$ 0.00134	2477 $\pm$ 58	2508 $\pm$ 14
TKB21-4	0.04	453	156	0.36	3.31510 $\pm$ 0.09072	0.11502 $\pm$ 0.00066	3.31645 $\pm$ 0.09076	0.11466 $\pm$ 0.00067	1699 $\pm$ 41	1875 $\pm$ 11

Spot Name	f206 (%)	U (ppm)	Th	Th	$(^{238}\text{U}/^{206}\text{Pb})_{\text{total}}$ ( $\pm 1\text{ s abs}$ )	$(^{207}\text{Pb}/^{206}\text{Pb})_{\text{total}}$	$(^{238}\text{U}/^{206}\text{Pb})_{204}$	$(^{207}\text{Pb}/^{206}\text{Pb})_{204}$	$^{206}\text{Pb}/^{238}\text{U}$ Age ( $\pm 1\text{ s Ma}$ )	
TKB22-H-1	0	69	10	0.15	2.15866 $\pm$ 0.01729	0.16805 $\pm$ 0.00086	2.15866 $\pm$ 0.01729	0.16805 $\pm$ 0.00086	2454 $\pm$ 16	2538 $\pm$ 9
TKB22-H-1b	0.02	1161	141	0.13	2.09843 $\pm$ 0.01231	0.16503 $\pm$ 0.00038	2.09892 $\pm$ 0.01231	0.16482 $\pm$ 0.00038	2512 $\pm$ 12	2506 $\pm$ 4
TKB22-H-4	0.01	1039	151	0.15	2.10930 $\pm$ 0.01235	0.16645 $\pm$ 0.00039	2.10950 $\pm$ 0.01236	0.16637 $\pm$ 0.00039	2501 $\pm$ 12	2521 $\pm$ 4
TKB22-H-7	0.23	926	86	0.1	2.22363 $\pm$ 0.01807	0.16617 $\pm$ 0.00043	2.22884 $\pm$ 0.01812	0.16408 $\pm$ 0.00046	2389 $\pm$ 16	2498 $\pm$ 5
TKB22-H-8	0.07	779	52	0.07	2.14824 $\pm$ 0.01591	0.16720 $\pm$ 0.00046	2.14985 $\pm$ 0.01592	0.16653 $\pm$ 0.00049	2462 $\pm$ 15	2523 $\pm$ 5
TKB22-H-9	0	1401	186	0.14	2.14216 $\pm$ 0.01453	0.16475 $\pm$ 0.00035	2.14218 $\pm$ 0.01453	0.16474 $\pm$ 0.00035	2470 $\pm$ 14	2505 $\pm$ 4
TKB22-H-12	0.05	2848	175	0.06	8.40221 $\pm$ 0.01996	0.16740 $\pm$ 0.00049	2.16921 $\pm$ 0.01997	0.16692 $\pm$ 0.00049	2444 $\pm$ 19	2527 $\pm$ 5
TKB22-H-13	0.14	721	124	0.18	2.33206 $\pm$ 0.01474	0.16875 $\pm$ 0.00057	2.33533 $\pm$ 0.01477	0.16750 $\pm$ 0.00060	2298 $\pm$ 12	2533 $\pm$ 6
TKB22-H-14	0.2	1097	249	0.23	2.20782 $\pm$ 0.01813	0.16997 $\pm$ 0.00044	2.21217 $\pm$ 0.01817	0.16822 $\pm$ 0.00047	2404 $\pm$ 16	2540 $\pm$ 5
TKB22-H-15	0.15	1748	220	0.13	1.99152 $\pm$ 0.01095	0.16825 $\pm$ 0.00027	1.99444 $\pm$ 0.01097	0.16695 $\pm$ 0.00028	2620 $\pm$ 12	2527 $\pm$ 3
TKB22-H-16	0.04	643	30	0.05	1.56351 $\pm$ 0.00995	0.26081 $\pm$ 0.00101	1.56416 $\pm$ 0.00996	0.26044 $\pm$ 0.00102	3186 $\pm$ 16	3249 $\pm$ 6
TKB22-L-1	0.82	174	51	0.3	2.18203 $\pm$ 0.01932	0.18754 $\pm$ 0.00111	2.19999 $\pm$ 0.01957	0.18026 $\pm$ 0.00136	2415 $\pm$ 18	2655 $\pm$ 13
TKB22-L-2	0.02	184	31	0.18	2.09844 $\pm$ 0.01849	0.17070 $\pm$ 0.00099	2.09891 $\pm$ 0.01850	0.17050 $\pm$ 0.00100	2512 $\pm$ 18	2563 $\pm$ 10
TKB22-L-4	0.18	214	67	0.32	2.05956 $\pm$ 0.01686	0.17296 $\pm$ 0.00089	2.06322 $\pm$ 0.01691	0.17137 $\pm$ 0.00095	2548 $\pm$ 17	2571 $\pm$ 9
TKB22-L-5	0.08	482	168	0.36	2.22414 $\pm$ 0.01475	0.16429 $\pm$ 0.00064	2.22602 $\pm$ 0.01477	0.16353 $\pm$ 0.00066	2392 $\pm$ 13	2493 $\pm$ 7
TKB22-L-6	0.04	346	82	0.24	2.03877 $\pm$ 0.01457	0.17425 $\pm$ 0.00067	2.03965 $\pm$ 0.01458	0.17387 $\pm$ 0.00068	2572 $\pm$ 15	2595 $\pm$ 7
TKB22-L-7	0.17	234	60	0.26	2.11672 $\pm$ 0.01671	0.17176 $\pm$ 0.00084	2.12026 $\pm$ 0.01675	0.17027 $\pm$ 0.00088	2491 $\pm$ 16	2560 $\pm$ 9
TKB22-L-8	0.12	172	84	0.51	1.99136 $\pm$ 0.01754	0.18408 $\pm$ 0.00101	1.99370 $\pm$ 0.01757	0.18304 $\pm$ 0.00104	2621 $\pm$ 19	2681 $\pm$ 9
TKB22-L-9	0.06	899	131	0.15	1.95426 $\pm$ 0.01360	0.17698 $\pm$ 0.00085	1.95539 $\pm$ 0.01361	0.17647 $\pm$ 0.00087	2663 $\pm$ 15	2620 $\pm$ 8
TKB22-L-11	0.06	240	69	0.3	2.14506 $\pm$ 0.01759	0.17143 $\pm$ 0.00097	2.14643 $\pm$ 0.01761	0.17086 $\pm$ 0.00099	2466 $\pm$ 17	2566 $\pm$ 10
TKB22-L-10	0.06	573	46	0.08	2.03468 $\pm$ 0.01338	0.17832 $\pm$ 0.00062	2.03590 $\pm$ 0.01339	0.17779 $\pm$ 0.00063	2576 $\pm$ 14	2632 $\pm$ 6
TKB22-L-12	0	174	58	0.34	2.08694 $\pm$ 0.01873	0.16486 $\pm$ 0.00100	2.08694 $\pm$ 0.01873	0.16486 $\pm$ 0.00100	2524 $\pm$ 19	2506 $\pm$ 10
TKB22-L-13	0.03	269	224	0.86	2.11723 $\pm$ 0.01645	0.16279 $\pm$ 0.00081	2.11779 $\pm$ 0.01645	0.16256 $\pm$ 0.00082	2493 $\pm$ 16	2482 $\pm$ 8
TKB22-L-14	0.09	466	71	0.16	2.10790 $\pm$ 0.01420	0.16700 $\pm$ 0.00063	2.10976 $\pm$ 0.01422	0.16621 $\pm$ 0.00064	2501 $\pm$ 14	2520 $\pm$ 7

Analyses were conducted during three sessions, each with BR266 as standard zircon, with a minimum of 14 standard analyses per session. f206 = proportion of non-radiogenic  $^{206}\text{Pb}$  in total  $^{206}\text{Pb}$ ; total denotes uncorrected ratios; 204 denotes 204-corrected ratios.

normal faults were vertical to gentle with down dip slickenlines (Fig. 5e, f) and had listric geometry in several places. The hanging wall of the sub-horizontal normal fault developed overturned drag folds (Fig. 5g) and subhorizontal extensional brittle fractures (Fig. 5h). Vertical gneissic layers were deflected by such horizontal fractures developing sinuous/folded structures with open recumbent geometry. The fractures were disjunctive cleavage in such folds, that didn't appear buckle folds (wavelength to thickness relation not followed, Ramsay, 1967). Granite-pegmatite veins intruded along brittle fractures along several orientations from horizontal to inclined and vertical (Fig. 51h).

#### 4.3. D<sub>3</sub>- Salem-Attur shear zone

##### 4.3.1. Map pattern and mesoscopic structure

The D<sub>3</sub>- Salem-Attur shear zone consisted of three sub-parallel thrusts (Fig. 2, D3-T1, D3-T2, and D3-T3) which were nearly E-W striking and inclined to the south. The Salem and Namakkal blocks lie in the footwall and hanging wall of the thrust system respectively. The NE-SW striking D<sub>1-2</sub> fabrics in foot- and hanging walls were aligned parallel to the shear zone close to the thrust (Figs. 1 and 2). The D<sub>3</sub>-T<sub>1</sub> developed south of Godumalai and Kanjamalai hills, with a curvilinear trend around an amphibolite outcrop at Moyerpalayam and joined the main shear zone north of Suryamalai hill. The D<sub>3</sub>-T<sub>2</sub> developed to the north of Kanjamalai and Godumalai hills, and the D<sub>3</sub>-T<sub>3</sub>, around Kusumalai hill with a curved geometry in map view. The interpretative cross section AB (Fig. 2h) depicted a trailing imbricate structure with D<sub>3</sub>-T<sub>1</sub> considered as main thrust, and the D<sub>3</sub>-T<sub>2</sub> and D<sub>3</sub>-T<sub>3</sub> are interpreted as trailing thrusts that joined D<sub>3</sub>-T<sub>1</sub> at depth. (e.g., Ramsay and Huber, 1987). The shear zones were characterized by biotite-muscovite-quartz-feldspar mylonite developed at Kandashram and Sarkar Nattar Mangalam on a granite gneiss, charnockite and quartzofeldspathic gneiss parent rock. Amphibolite mylonite was developed at Moyerpalayam, Kanjamalai, Kusumalai and Godumalai on mafic granulite. The amphibolite outcrop at Moyerpalayam represented a klippe (Fig. 2). The geological map at Moyerpalayam showed a NW-SE striking mylonitic foliation (D<sub>3</sub>) and NNW plunging (D<sub>3</sub>) stretching lineation defined by hornblende, biotite and epidote (Fig. 2a, stereonet, Fig. 3f for petrography). The variation in orientation was due to doming up of the Sankaridurg granite pluton. The detailed map of D<sub>3</sub>-T<sub>1</sub>, near Sarkar Nattar Mangalam (Fig. 2 for location; Fig. 6 for detail map) indicated mylonite and ultramylonite were developed on quartzofeldspathic gneiss. We suggest that, ultramylonite was developed from pseudotachylite veins injected into quartzofeldspathic gneiss.

Mesoscopic structures in the Salem-Attur shear zone included S<sub>3</sub> mylonitic foliations that varied in dip from gentle to steep towards the SSE (Fig. 7a, b). At places dip direction changed to NNE-N-NNW (Fig. 6a) due to progressive shearing. Perfectly down dip (D<sub>3</sub>) stretching lineations/ductile slickenlines (e.g., Lin et al., 2007) were developed on gently dipping (D<sub>3</sub>) mylonitic foliation (Fig. 7a). Steeply plunging (D<sub>3</sub>) stretching lineations (70–80 pitch) were present on the D<sub>3</sub> subvertical mylonitic foliation (Figs. 7c and 6a). The down dip stretching lineation on mylonitic foliation, the S-C fabric (Fig. 7b) and sigmoidal porphyroclasts (Fig. 7d) unequivocally indicated N to NNE vergence thrust kinematics.

There were several structural features that gave a false impression of strike-slip kinematics: (i) The F<sub>1</sub>-F<sub>2</sub> folds were reoriented to near vertical attitude due to D<sub>3</sub>-thrusting. As a result, asymmetric F<sub>1</sub> parasitic folds were exposed on the horizontal surface producing an impression of sinistral or dextral shearing (e.g., Ramsay and Lisle, 2000; Fig. 7e), however, these folds were pre-kinematic to D<sub>3</sub>- shearing. ii) Open folds were developed on S<sub>3</sub> mylonitic foliation as well as on S<sub>1</sub> gneissosity due to progressive shear and shortening across the shear zone. Southerly inclined axial parallel fractures are associated with these folds (Fig. 7f). The folds associated with horizontal fold axes and intersection lineation that gave a false impression of strike-slip. This phenomenon was explained in the structural model, Fig. 6b which indicated north

vergence thrust and close to that the S<sub>1</sub> fabric was compressed to develop E-W trending folds; the fold axes were at right angle to stretching lineations. Therefore, down-dip stretching lineation and horizontal fold axis/intersection lineation coexisted on the same outcrop. We get both lineations in the mylonites of Kandashram and Sarkar Nattar Mangalam area (Fig. 6a). iii) In the structural model, Fig. 6c, the E-W trending thrust produced an apparent dextral strike-slip offset of westerly dipping foliation on horizontal surface near Kandashram. Further, the satellite imagery indicated a dextral deflection of the S<sub>1</sub>-S<sub>2</sub> fabrics along the Salem-Attur shear zone.

##### 4.3.2. Microscopic structure

Both quartzofeldspathic (Fig. 8a–c) and amphibolitic mylonites (Fig. 3f and S1e) were marked by anastomosing C-fabrics (D<sub>3</sub>) around the feldspar porphyroclasts that contained intragranular faults and lacked dynamic recrystallization. The C-fabric was marked by biotite, hornblende and muscovite produced from the retrogression of granulite grade minerals. Ultramylonite (Fig. 8d–g) had fewer feldspar and quartz porphyroclasts and was marked by parallel mylonitic bandings with biotite and quartz. Quartz grains in the mylonite were marked by subgrain rotation crystallization and formed an S-C fabric (S<sub>3</sub>) with biotite (Fig. 8c). Quartz porphyroclasts in ultramylonite were rounded and contained embayed margins (Fig. 8e and g), and the feldspar porphyroclasts developed sigmoidal tails (Fig. 8e). Further, rectangular quartz grains produced monomineralic quartz ribbons (Fig. 8h). Features like retrogression of minerals, subgrain rotation in quartz grains, development of monomineralic quartz ribbons, brittle behavior of feldspar and lack of leucosome indicated greenschist to lower amphibolite facies conditions (~4kb/500 °C) during D<sub>3</sub> shearing (e.g., Stipp et al., 2002). Abundant shear sense indicators namely S-C fabric (Fig. 8c), sigmoidal feldspar porphyroclasts (Fig. 8b, f and g) and intragranular faults (Fig. 8b) confirmed top- to-NNE thrust kinematics.

##### 4.3.3. Vorticity analysis

The RGN-*Wm* estimates lay between 0.56 and 0.62 for the ultramylonite and between 0.68 and 0.81 for the mylonite (Fig. 9). The percentage of pure shear varied from 57 to 61% for the ultramylonite and from 40 to 52% for the mylonite (Table 1). The *Rs/θ - Wm* estimates were between 0.51 and 0.52 for the ultramylonite and 0.73 and 0.84 for the mylonite (Fig. 10a). The *Wm vs θ* plot (Fig. 10b) for both set indicated pure shear dominated transpression and the average *Wm* value was 0.7. Flattening strain in the Flinn's plot supported the pure shear component (Fig. 10c). The ultramylonite experienced more flattening than mylonite (low *Wm*). This could be because of the softer behavior of pseudotachylite from which the ultramylonite was presumably derived. Further, *Rs vs. θ* method overestimated *Wm* in ultramylonite compared to RGN-*Wm*. This was due to the fact that the *Rs/θ* method measured the last instantaneous strain while RGN-*Wm* measured the average strain (Wallis, 1995). Hence, the ultramylonite zone experienced more simple shear strain towards the end of deformation. The result indicated that the shear zone had undergone a temporal and spatial strain variation.

#### 4.4. Geochronology

##### 4.4.1. Zircon U-Pb SHRIMP

4.4.1.1. Sample TKB-18. The sample was collected from a charnockite of the Namakkal block (Fig. 2). Zircons ranged in size from 50 to 200 μm (Fig. 11a) and had aspect ratios between 1:1 and 3:1. The zircons were subrounded to round in shape, but many preserve crystal faces indicative of a magmatic character. CL imaging showed that the majority of zircon comprised a zoned inner rim domain with the oscillatory or sector-zoning pattern, overgrown by often extensive bright CL rim domains. Twenty-five analyses were conducted on thirteen grains, including twelve core-rim pairs and one rim. Based on significant common Pb contamination, three analyses were not

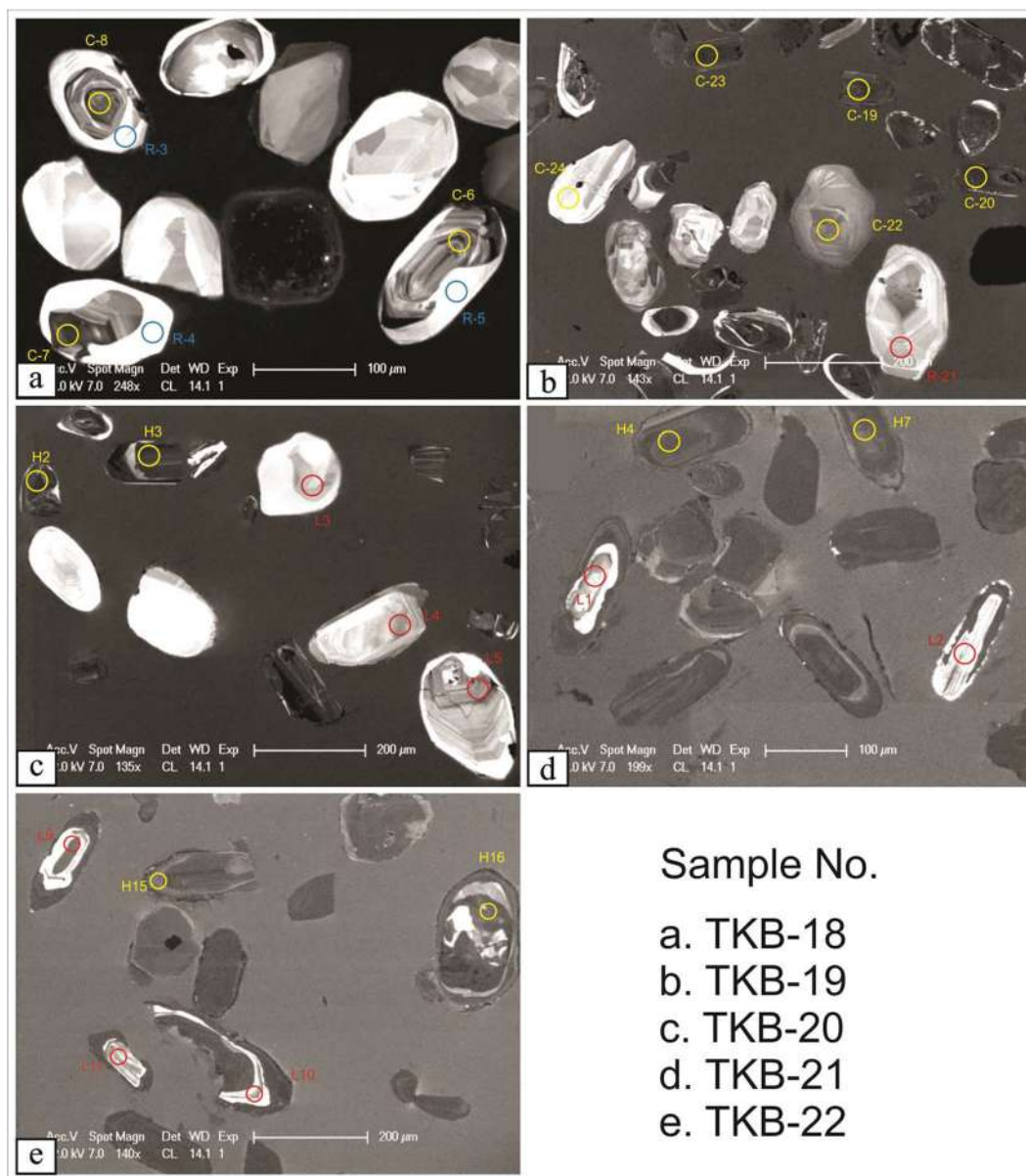


Fig. 11. (a–e) CL images of zircon, sample number TKB-18, 19, 20, 21 and 22.

discussed (see dashed ellipses in Fig. 12a, Table 2). U and Th content on core data were in the ranges 90–488 and 67–413 ppm respectively, with Th/U ratios between 0.5 and 3.8, consistent with magmatic zircon. The rim data were characterized by low U and Th contents, in the ranges 18–80 and 8–182 ppm respectively, with Th/U ratios between 0.2 and 3.8. These values were characteristic of zircon growing from small volumes of partial melt or metasomatic fluids, but not consistent with growth during metamorphism. The data on core appeared to define two separate populations, an older group of six analyses that defined a weighted mean  $^{207}\text{Pb}/^{206}\text{Pb}$  age of  $2604 \pm 28$  Ma and a younger group of four analyses giving a weighted mean  $^{207}\text{Pb}/^{206}\text{Pb}$  age of  $2530 \pm 39$  Ma. The eleven rim data defined a cluster of analyses that appeared to be aligned along a regression line with the lower intercept at  $712^{+780}/_{-540}$  Ma and upper intercept at  $2533^{+73}/_{-27}$  Ma. The poor precision of the lower intercept was due to the fact all data were concentrated along the upper part of the regression and using only the six-concordant data points a weighted mean  $^{207}\text{Pb}/^{206}\text{Pb}$  age of  $2518 \pm 21$  Ma could be calculated. We interpreted the oldest age group on the core to represent xenocrystic components in the charnockite derived from a uniform source with an age of

$2604 \pm 28$  Ma. The younger core population was interpreted as the emplacement age of the charnockite/granite at  $2530 \pm 39$  Ma. The low U rims were constraining crystallization of the latest-stage fluids during cooling of the granite at  $2518 \pm 21$  Ma.

4.4.1.2. *Sample TKB-19.* The sample was collected from charnockite/granite in the Namakkal block. Zircons range in size from smaller than  $50 \mu\text{m}$  to over  $200 \mu\text{m}$  and have aspect ratios from 1:1 to 4:1. The grains were either subrounded to rounded or elongate with clearly defined crystal faces. CL imaging indicated two types of zircon in the sample (Fig. 11b, Table 2). The largest population were elongated and had very low luminescence. Some of these grains had narrow bright CL rim overgrowths, one of which was analyzed (TKB-19-R-8). A smaller second population comprised larger, often equant grains that displayed very high CL response. Some of these larger grains also had core and rim domains, and one rim was large enough for analysis (TKB-19-R-21, Fig. 11b). Twenty-four analyses were conducted on 24 zircons, including 22 single analyses on zircon and one core-rim pair (TKB-19-C-7, TKB-19-R-8, Table 2). Common Pb was relatively high in four points which were not further discussed (see dashed ellipses in Fig. 12b,

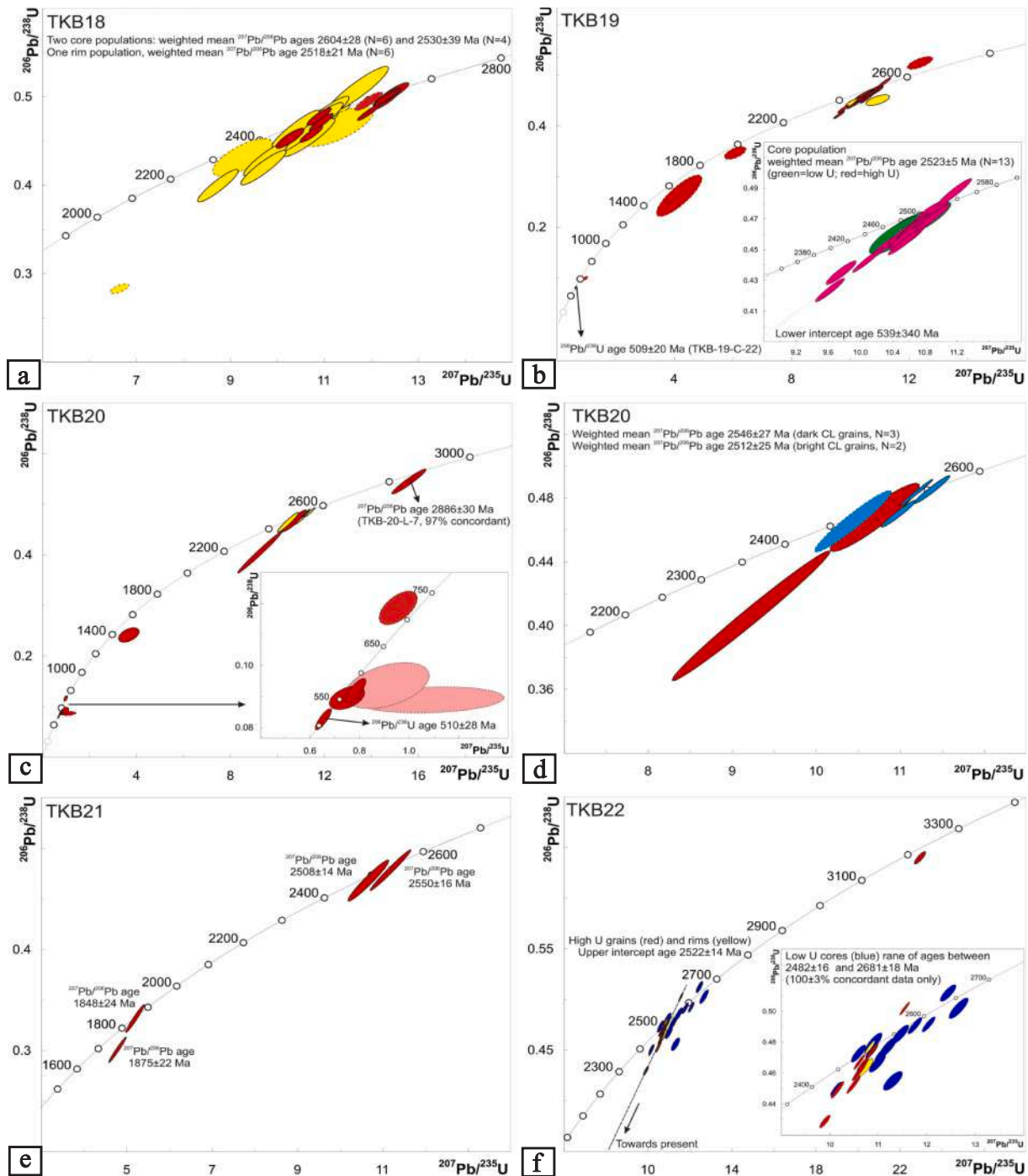


Fig. 12. Zircon U-Pb data for samples TKB-18, 19, 20, 21 and 22 sample locations are in Figs. 1 and 2. Errors are at  $1\sigma$  confidence level.

Table 2). One data point (TKB-19-C-22, Figs. 11 and 12) plots on concordia and defines a  $^{206}\text{Pb}/^{238}\text{U}$  age of  $509 \pm 20$  Ma. This point records a U and Th values of 337 and 414 ppm respectively and has a Th/U ratio of 1.3, consistent with magmatic zircon (Fig. 12). The remaining data, including both high CL (low U) and low CL (high U) grains, clearly plot along a discordia line for which a lower intercept of  $539 \pm 340$  Ma and upper intercept of  $2531 \pm 11$  Ma could be calculated. Considering only the more precise high U analyses, corresponding to the population of dark CL grains, the upper intercept was  $2534 \pm 17$  Ma. A weighted mean  $^{207}\text{Pb}/^{206}\text{Pb}$  age of  $2523 \pm 5$  Ma could be calculated from the 13 concordant data points that was interpreted to be the best estimate for the emplacement age of the charnockite/granite. The lower intercept, although very imprecise,

suggested that the rock was affected by a Pb-loss event at around 540 Ma, further supported the youngest concordant grain, dated at  $509 \pm 20$  Ma.

4.4.1.3. *Sample TKB-20.* The sample was collected from charnockite/granite to the east of Salem. Zircons ranged in size from  $< 50 \mu\text{m}$  to over  $250 \mu\text{m}$  and had aspect ratios between 1:1 and 4:1. The zircon was subrounded, but many preserved crystal faces. CL imagery indicated two populations (Figs. 11 and 12; Table 2); one of smaller grains with a very low response, one of larger grains with very luminescent character. Many analyses on dark-CL grains were discarded due to significant counts on  $^{204}\text{Pb}$ . Two analyses, which also recorded relatively high amounts of common Pb, were completed, but need to be excluded as

they had large errors and were significantly discordant (TKB-20-L-5, Fig. 12c and d; TKB-20-L-8). The bright-CL grains defined a wide range of apparent ages between 510 and 2807 Ma, while the dark-CL grains defined a more narrow range of  $^{207}\text{Pb}/^{206}\text{Pb}$  ages between 2560 and 2485 Ma. The oldest analysis was on a bright CL round zircon which recorded a  $^{207}\text{Pb}/^{206}\text{Pb}$  age of  $2886 \pm 30$  Ma (TKB-20-L-7). Three dark-CL grains gave a weighted mean  $^{207}\text{Pb}/^{206}\text{Pb}$  age of  $2546 \pm 27$  Ma, while two less precise bright-CL grains gave the weighted mean  $^{207}\text{Pb}/^{206}\text{Pb}$  age of  $2512 \pm 26$  Ma. One dark CL zircon gave yet a slightly younger  $^{207}\text{Pb}/^{206}\text{Pb}$  age of  $2485 \pm 28$  Ma. Together these analyses were taken to indicate crystallization of primary zircon from various melt batches that generated the charnockite/granite. We, therefore, considered the granite to have been emplaced sometime between 2550 and 2480 Ma. A number of analyses on bright-CL zircon yielded  $^{206}\text{Pb}/^{238}\text{U}$  ages of between 575 and 510 Ma (excluding one strongly inversely discordant point, TKB-20-L-4, Fig. 12c). The most concordant and youngest data point provided a  $^{206}\text{Pb}/^{238}\text{U}$  age of  $510 \pm 28$  Ma and was taken to provide an estimate for crystallization of these zircons (Figs. 11 and 12; Table 2). This corresponded to the intrusion of granite veins during brittle fracturing.

**4.4.1.4. Sample TKB-21.** The sample belongs to pink granite mixed with pseudotachylite, it was collected from the Gangavalli shear zone (Fig. 3h). The granite was a small circular plutonic body with dimension of 20 m across, having been traversed by several fractures and pseudotachylite veins. Therefore, the granite intrusion was pre-tectonic to strike-slip fracturing ( $D_4$ ). As it contained xenoliths of  $D_3$ -mylonites, it was post-tectonic to ductile shearing ( $D_3$ ). It is therefore aimed that the age of the granite would constrain the upper age limit of ductile shearing and the lower age limit of brittle fracturing. Only very few zircons were recovered from the sample. The zircons were broken but had euhedral shapes with well-developed crystal faces. In CL, the zircon produced medium to high response, with prominent oscillatory zoning pattern indicating a magmatic character (Figs. 11-H-4, H-7, L-1, L2 and 12; Table 2). Four analyses were conducted on four zircons. The data defined two age groups: the oldest analyses gave  $^{207}\text{Pb}/^{206}\text{Pb}$  ages of  $2550 \pm 16$  and  $2508 \pm 14$  Ma, while two younger analyses gave  $^{207}\text{Pb}/^{206}\text{Pb}$  ages of  $1848 \pm 24$  and  $1875 \pm 22$  Ma (Figs. 11d and 12e; Table 2). We interpreted that these zircon grains were all magmatic, so they were most likely magmatic components, unrelated to the pseudotachylite formation. This suggested protolith would have been perhaps between  $1848 \pm 24$  and  $1875 \pm 22$  Ma, with xenocrysts of  $2550 \pm 16$  and  $2508 \pm 14$  Ma.

**4.4.1.5. Sample TKB-22.** The sample was collected from syenite intruded along  $D_2$  shear zone west of Attur. Zircons were between 50 and 300  $\mu\text{m}$  in size and had aspect ratios between 2:1 and 5:1. The grains were sub- to euhedral and had well-preserved crystal faces and bipyramidal terminations, all indicative of a magmatic character. CL imagery revealed a dark population of zircon in which there was sometimes a small lighter CL core domain. A minority of zircon were bright CL, similar in character to the preserved cores (Figs. 11e and 12; Table 2). Twenty-four analyses were conducted, eleven on bright CL core domains, nine on dark CL grains, two on dark CL rim domains overgrowing small bright CL cores, one on a non-complex bright CL zircon (TKB-22-L-13) and one on an anomalous dark-CL core of a large zircon (TKB-22-H-16). The data on dark CL-zircon had a higher U content and lower Th/U ratios than data from bright CL zircon. Ten analyses of the dark-CL zircon, including the two analyses on rim domains, defined a linear array with lower intercept indicating recent Pb-loss, and the upper intercept age was  $2522 \pm 14$  Ma. The bright-CL core data defined a scattered population with the concordant data providing apparent  $^{207}\text{Pb}/^{206}\text{Pb}$  ages between  $2482 \pm 16$  and  $2681 \pm 18$  Ma. The anomalous dark-CL core analyzed gave a concordant  $^{207}\text{Pb}/^{206}\text{Pb}$  age of  $3249 \pm 12$  Ma (Fig. 12f). We interpreted the dark and bright CL cores to indicate various inherited

zircon component, while the dark CL zircon and rims gave an emplacement age of  $2522 \pm 14$  Ma for the syenite.

Zircon geochronological data suggested that intrusion of charnockite/granite gneiss in the Salem-Namakkal blocks was constrained over a broad age range between ca. 3250 and ca. 2500 Ma. There were several phases of charnockitic magma intrusion comparable to many granulite terranes (e.g., Oyhantcabal et al., 2012; Oriolo et al., 2016). This was consistent with the result obtained by Clark et al. (2009), about the age of the charnockite from the Salem block. Hence, charnockitic intrusion in both Salem and Namakkal blocks was of same age. The  $D_3$  thrusting along the Salem-Attur shear zone was a younger than ca. 2500 Ma event. The lower age of the thrusting was constrained by the intrusion of the pink granite at ca. 1900 Ma.

#### 4.4.2. Monazite geochronology

**4.4.2.1. Sample S-478.** Monazite grains were present within the quartz-biotite-rich mylonite that was characterized by distinct  $D_3$  mylonitic foliation with sigmoidal feldspar porphyroclasts (Fig. 13a–e). The monazite grains were round to subrounded with a distinct mantle structure. Mantle consisted of newly crystallized monazites marked by DPC produced during shearing. The mantle was converted to asymmetric wings producing sigma-type monazite porphyroclasts, aligned parallel to the  $D_3$ -mylonitic foliation (Fig. 13a and c). The structure was exactly similar to the winged feldspar porphyroclasts produced during  $D_3$  shearing (Fig. 8a, b). Hence, the core part represented the  $D_{1-2}$  monazite and the mantle grains represented the  $D_3$  monazite. Elemental analysis of core and mantle indicated that the core was rich in Y, HREE and depleted in Th while the opposite was the case for the mantle (Table 3). This was also indicated by the X-ray images of some of the grains (Fig. 13d, e). Other elements like Pb and U had low concentration and Ce a higher concentration in the mantle compared to the core. Depletion in Y probably happened due to the mobilization of Y into biotite and garnet that developed during shearing. Further, the monazites were fractured subsequent to ductile deformation (Fig. 13b). Sixty-seven analyses were completed, and the isoplot was constructed (Fig. 13f) which had three clusters of ages as ca. 2435 Ma, ca. 2010 Ma, and ca. 860 Ma (Fig. 13f). The oldest ages were derived from cores and indicated the age of granulite facies metamorphism ( $\text{syn-}D_{1-2}$ ); the second ca. 2.0 Ga age was derived from the mantles and indicated the age of ductile shearing ( $D_3$ ) while the youngest ages ca. 0.8 Ga probably indicate hydrothermal alteration during brittle shearing ( $D_4$ ).

**4.4.2.2. Sample S-470.** The sample was collected from the granite gneiss intruded within mafic granulite in the Kanjamalai Hill of the Salem block. The granite gneiss was marked by  $D_1$  gneissic fabric. The monazites were present as inclusions inside quartz and underwent DC. These were smaller in size, equant to irregular in shape and had compositional domains (Fig. 14a–c). No DPC fabrics were recorded as the sample lie away from the Salem-Attur shear zone. The compositional domains do vary in chemistry with the younger domains recording lower Y, Th, HREE, Pb, U and high in LREE (Table 3). The Y and HREE were mobilized to garnet developed during high grade metamorphism. The histogram had three clusters of ages at ca. 2580 Ma, 2460 Ma and 2250 Ma (Fig. 14d). First one corresponded to the age of granitic intrusion and later two to the timing of granulite metamorphism syntectonic with  $D_{1-2}$  deformation.

#### 4.4.3. $^{40}\text{Ar}$ - $^{39}\text{Ar}$ analysis

**4.4.3.1. Sample T-1.** Large  $D_3$  hornblende crystals, from amphibolites, near Tiruchengode (Fig. 2) were used for  $^{40}\text{Ar}$ - $^{39}\text{Ar}$  dating. The data defined a  $^{40}\text{Ar}/^{39}\text{Ar}$  plateau age of  $2049.4 \pm 4.7$  Ma (MSWD = 0.27, probability = 0.95) (Fig. 15a and Table 4). We interpret this age to reflect the age of hornblende growth and  $D_3$ - ductile shearing.

**4.4.3.2. Sample B-4.** A fresh and unaltered sample of pseudotachylite

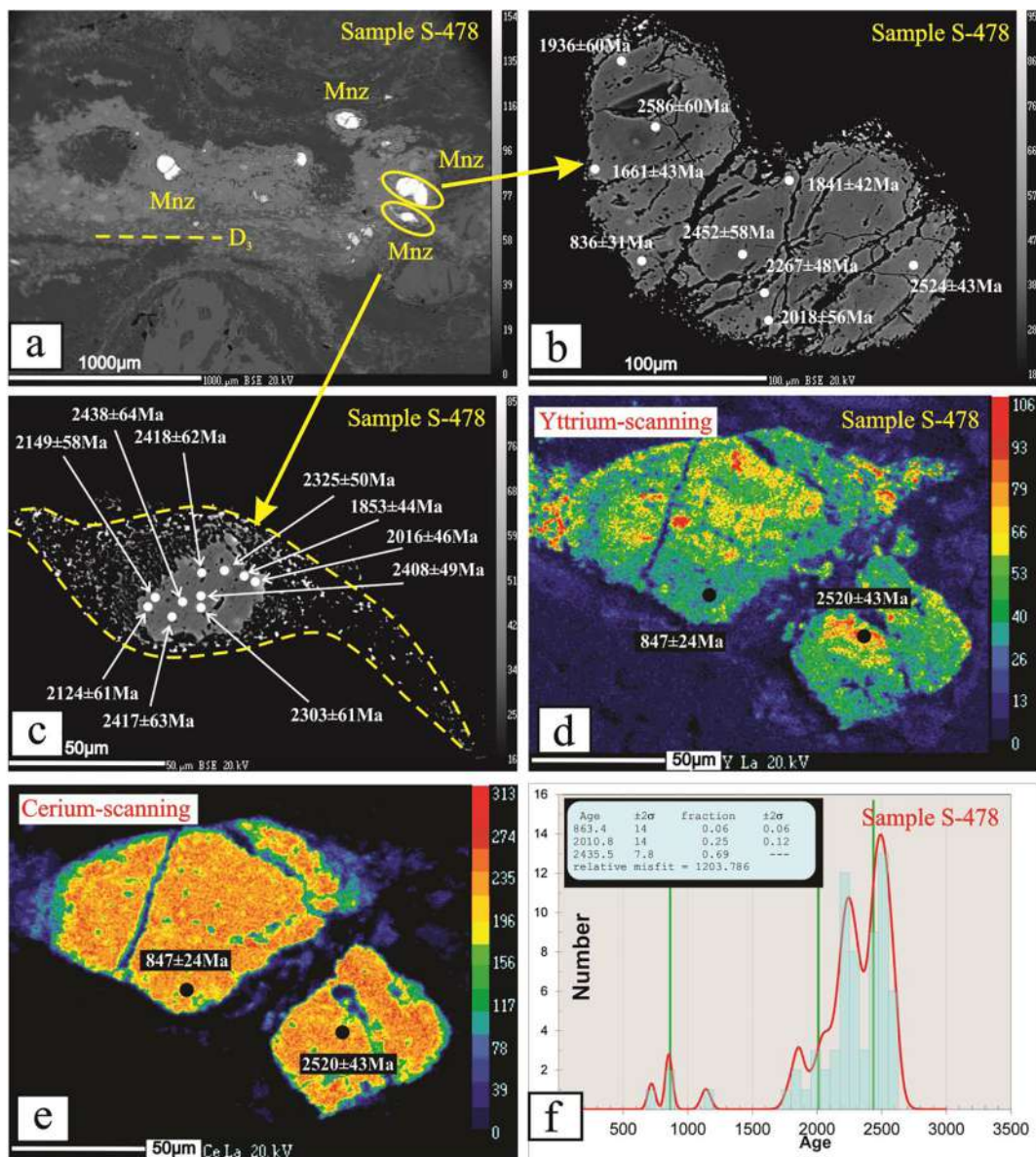


**Fig. 13.** (a) EPMA back scatter electron (BSE) Image taken in EPMA, Sample S-478,  $D_3$ - mylonite containing monazite (Mnz) grains within the quartz-biotite matrix; (b) One of the monazite grains has micro monazite grains precipitated around the larger grain. The original grain is broken by fractures, older ages are seen in the core of the grain, while younger ages in the periphery; (c) Monazite porphyroblast with asymmetric wings. The peripheral grains have ca. 2.0 Ga and the core has ca. 2.4 Ga; (d-e) X-ray images of  $D_3$ - monazites with Y and Ce variation from core to the periphery; (f) The histogram has ca. 2.4, 2.0 and 0.8 Ga ages corresponding to metamorphism ( $D_1$ - $D_2$ ), ductile shearing ( $D_3$ ) and brittle shearing ( $D_4$  normal faulting).

from the Gangavalli strike-slip fault was chosen for  $^{40}\text{Ar}$ - $^{39}\text{Ar}$  dating through step heating (Fig. 1 for sample location). A plateau age of  $1852 \pm 9$  Ma can be calculated (MSWD = 0.02, probability = 1) (Fig. 15b and Table 4). This age marked the timing of strike-slip brittle shearing.

**4.4.3.3. Sample T-2.** This was a biotite sample from a granite/pegmatite vein intruded along the normal faults. The biotite produced a well-defined  $^{40}\text{Ar}$ / $^{39}\text{Ar}$  plateau age of  $563 \pm 2$  Ma (MSWD = 0.89, probability = 0.50) suggesting its cooling/crystallization age (Fig. 15c and Table 4). This age may reflect the minimum age of normal faulting and granite/pegmatite intrusion.

## 5. Discussion

### 5.1. Deformation in the Salem-Attur shear zone

The Salem-Namakal blocks had recorded multiple stages of shearing that included  $D_2$ - high temperature shearing,  $D_3$ - low temperature shearing and  $D_4$ - brittle shearing. The Salem-Attur shear zone represented a  $D_3$  shear zone which formed at quartz ductile-feldspar brittle zone. It was a retrograde shear zone characterized by retrogression of granulite minerals to hornblende, biotite and muscovite. From outcrop to microscopic scale, the mylonites recorded a top to N-NNE thrust slip kinematics. The  $RGN$  and  $Rs/\theta$  analyses suggested that the shear zone underwent a general simple shear with an average 50% pure shear component. The average  $Wm$  value derived from both methods was about 0.7. The presence of the pure shear component led to variation in finite strain and the orientation of stretching lineation. The  $D_3$ - stretching lineation was down dip in gently dipping  $D_3$ -

**Table 3**  
Monazite compositions and U-Th-Pb (total) monazite ages obtained from mylonite (Sample S-478; N11°40'05.09", E78°19'02.11") and granitic gneissic (Sample S-470; N11°38'05.26", E78°04'28.52") using electronprobe micro analysis (EPMA).

Sample S-470																		
DataSet/Point	Al <sub>2</sub> O <sub>3</sub>	SiO <sub>2</sub>	P <sub>2</sub> O <sub>5</sub>	CaO	Y <sub>2</sub> O <sub>3</sub>	La <sub>2</sub> O <sub>3</sub>	Ce <sub>2</sub> O <sub>3</sub>	Pr <sub>2</sub> O <sub>3</sub>	Nd <sub>2</sub> O <sub>3</sub>	Sm <sub>2</sub> O <sub>3</sub>	Gd <sub>2</sub> O <sub>3</sub>	Dy <sub>2</sub> O <sub>3</sub>	PbO	ThO <sub>2</sub>	UO <sub>2</sub>	Total	Age (Ma)	± Age (Ma)
2/1	0	2.185	26.366	0.141	4.846	8.622	23.554	3.409	15.203	3.119	2.81	1.333	0.564	4.784	0.259	97.268	2198	54
3/1	0.029	2.157	25.943	0.065	2.006	11.093	26.469	3.441	13.774	2.637	2.08	0.742	0.664	6.029	0.16	97.292	2247	50
4/1	0	1.557	26.76	0.163	4.348	10.701	25.056	3.177	13.178	2.702	2.333	1.169	0.589	4.741	0.168	96.642	2438	58
5/1	0	1.679	27.193	0.204	3.766	11.642	25.302	3.14	12.728	2.553	1.039	0.624	0.624	4.941	0.172	97.168	2480	57
6/1	0	1.716	27.116	0.235	3.555	11.888	25.342	3.134	12.786	2.602	2.196	0.99	0.608	4.887	0.19	97.245	2416	57
7/1	0	1.333	28.044	0.134	5.417	8.424	23.335	3.379	15.41	3.253	2.937	1.435	0.452	3.426	0.235	97.214	2331	66
8/1	0	1.86	26.875	0.181	5.143	7.876	22.246	3.325	15.318	3.297	3.001	1.381	0.736	5.487	0.331	97.039	2449	52
9/1	0	1.056	28.4	0.136	5.213	9.105	24.832	3.527	15.154	3.027	2.565	1.327	0.295	2.235	0.182	97.055	2251	86
10/1	0.006	0.995	28.143	0.114	4.831	9.826	25.94	3.545	14.502	2.698	2.216	1.207	0.27	2.034	0.156	96.483	2292	94
11/1	0.037	1.543	27.323	0.187	4.044	11.131	25.271	3.169	13.158	2.658	2.235	1.088	0.571	4.469	0.149	97.033	2518	62
12/1	0.023	3.388	24.45	0.246	3.718	7.437	20.882	3.157	14.278	3.012	2.633	1.114	1.349	11.163	0.298	97.148	2446	37
13/1	0.282	1.537	27.849	0.139	5.201	9.303	24.823	3.355	14.314	2.775	2.432	1.284	0.404	3.358	0.176	97.232	2247	68
14/1	0.054	0.92	27.974	0.124	3.916	10.72	26.902	3.524	14.536	2.606	2.102	1.014	0.218	1.723	0.146	96.478	2157	103
17/1	0.028	1.909	26.963	0.179	4.29	9.888	24.199	3.235	13.216	2.7	2.415	1.152	0.72	5.702	0.177	96.773	2508	53
18/1	0	1.059	29.398	0.084	2.443	11.618	26.627	3.549	14.635	2.481	1.824	0.877	0.256	2.275	0.095	97.221	2181	93
19/1	0.014	1.526	28.912	0.185	3.45	12.32	26.396	3.192	12.991	2.72	2.26	0.909	0.484	3.735	0.104	99.199	2595	71
20/1	0.002	1.909	27.754	0.186	3.983	10.857	24.692	3.176	13.19	2.637	2.358	1.065	0.61	5.402	0.174	97.995	2259	52
21/1	0.044	1.868	27.905	0.216	4.273	9.173	23.381	3.304	14.285	3	2.649	1.134	0.702	6.566	0.129	97.72	2539	54
22/1	0.027	1.324	28.675	0.08	2.826	11.477	27.579	3.498	14.159	2.531	1.923	0.795	0.316	2.505	0.142	97.858	2319	87
25/1	0.009	1.136	28.904	0.145	5.895	9.404	24.507	3.33	14.088	2.744	2.481	1.357	0.333	2.604	0.165	97.103	2304	80
26/1	0.004	1.489	28.5	0.15	5.118	8.603	23.394	3.391	15.307	3.182	2.902	1.355	0.482	3.864	0.231	97.971	2276	62
27/1	0.009	2.627	26.608	0.222	3.383	8.882	23.252	3.234	14.252	2.854	2.352	0.91	0.961	8.381	0.082	98.008	2470	42
28/1	0.006	2.275	27.036	0.159	4.532	8.702	22.89	3.304	14.751	3.12	2.818	1.234	0.704	5.946	0.293	97.772	2238	48
29/1	0.088	1.129	28.979	0.118	5.136	9.564	25.069	3.485	14.525	2.74	2.32	1.236	0.329	2.499	0.15	97.367	2384	85
30/1	0.079	1.255	30.184	0.122	4.426	10.158	25.769	3.499	14.619	2.697	2.35	1.098	0.212	1.898	0.157	98.521	1931	92
31/1	0.006	2.517	26.874	0.196	4.848	7.62	21.364	3.188	14.665	3.247	2.908	1.294	0.99	7.702	0.347	97.765	2439	43
32/1	0	1.647	28.009	0.232	3.664	9.478	24.127	3.388	14.621	3.054	2.635	1.038	0.595	5.04	0.061	97.588	2515	57
33/1	0	1.732	28.008	0.217	5.609	10.156	23.789	3.098	12.716	2.639	2.515	1.306	0.596	4.704	0.178	97.262	2461	58
34/1	0.319	4.047	24.217	0.266	3.582	6.908	19.613	3.047	13.796	2.974	2.561	1.038	1.715	13.891	0.206	98.181	2598	35
Sample S-478																		
DataSet/Point	Al <sub>2</sub> O <sub>3</sub>	SiO <sub>2</sub>	P <sub>2</sub> O <sub>5</sub>	CaO	Y <sub>2</sub> O <sub>3</sub>	La <sub>2</sub> O <sub>3</sub>	Ce <sub>2</sub> O <sub>3</sub>	Pr <sub>2</sub> O <sub>3</sub>	Nd <sub>2</sub> O <sub>3</sub>	Sm <sub>2</sub> O <sub>3</sub>	Gd <sub>2</sub> O <sub>3</sub>	Dy <sub>2</sub> O <sub>3</sub>	PbO	ThO <sub>2</sub>	UO <sub>2</sub>	Total	Age (Ma)	± Age (Ma)
1/1	0	0.915	29.02	2.166	0.895	13.001	27.205	3.138	12.14	2.217	1.494	0.361	0.395	4.297	0.089	97.333	1936	60
2/1	0.014	0.972	29.34	0.653	1.227	14.169	28.204	3.027	11.831	2.127	1.469	0.419	0.648	5.151	0.107	99.358	2586	60
3/1	0	1.257	29.102	0.595	1	14.226	28.127	3.013	11.438	2.084	1.357	0.38	0.486	6.497	0.052	99.615	1661	43
4/1	0	1.102	29.262	0.545	1.23	14.371	28.358	3.039	11.65	2.061	1.32	0.391	0.644	5.258	0.157	99.389	2452	58
5/1	0.004	1.064	29.448	0.541	1.1	14.403	28.46	3.058	11.907	2.08	1.365	0.408	0.527	4.973	0.134	99.472	2166	57
6/1	0.142	2.273	28.567	0.653	0.622	13.62	26.979	3.068	11.857	2.083	1.265	0.469	0.47	6.238	0	98.209	2248	48
7/1	0.665	1.08	28.287	0.524	1.492	13.605	27.623	3.092	12.205	2.249	1.59	0.22	0.623	4.709	0.149	98.209	2018	56
8/1	0.076	1.654	28.513	0.739	0.656	13.679	27.585	3.072	11.849	2.09	1.262	0.284	0.716	6.838	0.07	99.083	2267	48
9/1	0	1.788	27.938	0.856	0.304	13.156	27.507	3.11	11.938	2.092	1.193	0.166	0.849	7.914	0	98.811	2407	44
10/1	0.006	1.779	28.229	0.798	0.182	13.184	27.416	3.063	11.853	2.091	1.202	0.164	0.966	8.556	0	99.492	2524	43
11/1	0	1.017	29.444	0.758	1.206	14.398	28.042	3.055	11.562	2.081	1.397	0.379	0.574	5.546	0.113	99.574	2168	53
12/1	0.022	1.724	28.172	0.585	0.227	13.517	28.044	3.155	12.037	2.133	1.211	0.191	0.547	8.168	0	99.732	1535	35
17/1	0.275	1.79	28.774	3.989	0.421	13.226	25.457	3.003	11.311	1.904	1.191	0.213	0.574	7.098	0	99.226	1841	42
21/1	0.002	0.939	29.149	0.519	1.084	14.304	28.581	3.119	12.058	2.164	1.439	0.346	0.542	4.482	0.126	98.853	2438	64
22/1	0.006	1.245	28.696	0.722	0.839	13.475	27.609	3.088	11.864	2.206	1.452	0.361	0.688	6.45	0.05	98.753	2325	50
27/1	0.004	1.5	28.517	0.65	0.632	13.651	27.777	3.14	12.289	2.183	1.382	0.283	0.523	6.419	0	98.95	1853	44
28/1	0.006	1.001	29.633	0.585	1.251	14.488	28.086	3.099	11.845	2.084	1.424	0.381	0.557	4.697	0.118	99.255	2418	62
29/1	0.035	0.923	30.407	0.729	1.214	14.584	28.555	3.045	11.812	2.148	1.423	0.415	0.544	4.62	0.106	100.561	2417	63

(continued on next page)

Table 3 (continued)

Sample S-470	DataSet/Point	Al <sub>2</sub> O <sub>3</sub>	SiO <sub>2</sub>	P <sub>2</sub> O <sub>5</sub>	CaO	Y <sub>2</sub> O <sub>3</sub>	La <sub>2</sub> O <sub>3</sub>	Ce <sub>2</sub> O <sub>3</sub>	Pr <sub>2</sub> O <sub>3</sub>	Nd <sub>2</sub> O <sub>3</sub>	Sm <sub>2</sub> O <sub>3</sub>	Gd <sub>2</sub> O <sub>3</sub>	Dy <sub>2</sub> O <sub>3</sub>	PbO	ThO <sub>2</sub>	UO <sub>2</sub>	Total	Age (Ma)	± Age (Ma)
30/1		0.02	0.984	29.693	0.608	1.673	13.362	27.753	3.179	12.628	2.406	1.665	0.517	0.547	4.342	0.194	99.569	2398	63
31/1		0.038	1.827	27.83	0.886	0.5	13.353	26.607	3.092	12.047	2.105	1.181	0.199	0.833	7.499	0	97.997	2485	46
33/1		0.007	1.415	28.571	0.597	0.647	13.834	28.027	3.099	12.227	2.198	1.392	0.275	0.671	6.244	0	99.204	2408	49
34/1		0.016	0.881	29.755	0.63	1.125	14.711	28.476	3.051	11.699	2.107	1.388	0.394	0.492	4.807	0.094	99.626	2149	58
35/1		0.017	0.878	30.023	0.596	1.224	14.269	28.423	3.069	12.045	2.258	1.483	0.438	0.463	4.542	0.099	99.826	2124	61
36/1		0	0.994	29.325	0.532	1.082	14.369	28.487	3.081	12.154	2.2	1.447	0.373	0.534	4.706	0.129	99.412	2303	61
37/1		0.015	1.491	28.202	1.083	0.631	13.784	28.109	3.122	12.346	2.196	1.398	0.265	0.565	6.348	0	99.554	2016	46
38/1		0.013	1.551	27.919	0.306	0.147	15.172	28.897	3.047	11.572	1.761	0.883	0.096	0.275	7.466	0.06	99.165	836	31
1/2		0	0.915	29.02	2.166	0.895	13.001	27.205	3.138	12.14	2.217	1.494	0.361	0.398	4.29	0.089	97.329	1950	61
2/2		0.014	0.972	29.339	0.653	1.227	14.169	28.204	3.027	11.831	2.127	1.469	0.419	0.653	5.151	0.107	99.363	2605	61
3/2		0	1.257	29.102	0.595	1	14.226	28.127	3.013	11.438	2.084	1.357	0.38	0.486	6.497	0.049	99.612	1664	43
4/2		0	1.102	29.262	0.545	1.23	14.371	28.358	3.039	11.65	2.061	1.32	0.391	0.649	5.258	0.157	99.393	2467	59
5/2		0.004	1.064	29.448	0.541	1.1	14.403	28.46	3.058	11.907	2.08	1.365	0.408	0.527	4.973	0.134	99.472	2166	57
6/2		0.142	2.273	28.567	0.653	0.622	13.62	26.979	3.068	11.857	2.083	1.265	0.22	0.623	6.238	0	98.209	2248	48
7/2		0.665	1.08	28.287	0.524	1.492	13.605	27.623	3.092	12.205	2.249	1.59	0.469	0.47	4.709	0.149	98.209	2016	57
8/2		0.076	1.654	28.514	0.739	0.656	13.679	27.585	3.072	11.849	2.09	1.262	0.284	0.716	6.838	0.064	99.077	2274	48
9/2		0	1.788	27.938	0.856	0.304	13.156	27.507	3.11	11.938	2.092	1.193	0.166	0.849	7.914	0	98.811	2407	44
10/2		0.006	1.779	28.228	0.798	0.182	13.184	27.416	3.063	11.853	2.091	1.202	0.164	0.972	8.557	0	99.497	2540	44
11/2		0	1.017	29.444	0.758	1.206	14.398	28.042	3.055	11.562	2.081	1.397	0.379	0.58	5.547	0.113	99.578	2185	54
12/2		0.022	1.724	28.172	0.585	0.227	13.517	28.044	3.155	12.037	2.133	1.211	0.191	0.547	8.168	0	99.732	1535	35
17/2		0.275	1.79	28.771	3.989	0.421	13.226	25.457	3.003	11.31	1.904	1.191	0.213	0.595	7.099	0	99.243	1903	45
21/2		0.002	0.939	29.149	0.519	1.084	14.304	28.58	3.119	12.058	2.164	1.439	0.346	0.542	4.476	0.126	98.847	2440	64
22/2		0.006	1.245	28.696	0.722	0.839	13.475	27.609	3.088	11.864	2.206	1.452	0.361	0.692	6.45	0.05	98.756	2338	50
27/2		0.004	1.5	28.516	0.65	0.632	13.651	27.777	3.14	12.289	2.183	1.382	0.283	0.535	6.419	0	98.96	1892	46
28/2		0.006	1.001	29.631	0.585	1.251	14.488	28.086	3.099	11.845	2.084	1.424	0.381	0.564	4.708	0.117	99.271	2441	65
29/2		0.035	0.923	30.407	0.729	1.214	14.584	28.555	3.045	11.812	2.148	1.423	0.415	0.544	4.62	0.106	100.561	2417	63
30/2		0.02	0.984	29.692	0.608	1.673	13.362	27.753	3.179	12.628	2.406	1.665	0.517	0.549	4.35	0.193	99.578	2405	64
31/2		0.038	1.827	27.829	0.886	0.5	13.354	26.607	3.092	12.047	2.104	1.181	0.199	0.842	7.499	0	98.005	2511	47
33/2		0.007	1.415	28.571	0.597	0.647	13.834	28.027	3.099	12.227	2.198	1.392	0.275	0.671	6.244	0	99.204	2408	49
34/2		0.016	0.881	29.755	0.63	1.125	14.711	28.476	3.051	11.699	2.107	1.388	0.394	0.497	4.807	0.094	99.631	2169	59
35/2		0	0.978	30.023	0.596	1.224	14.269	28.423	3.069	12.045	2.258	1.483	0.438	0.461	4.542	0.099	99.825	2117	64
36/2		0	0.994	29.325	0.532	1.082	14.369	28.487	3.081	12.154	2.2	1.447	0.373	0.537	4.706	0.129	99.415	2316	62
37/2		0.015	1.491	28.202	1.083	0.631	13.784	28.109	3.122	12.346	2.196	1.398	0.265	0.565	6.348	0	99.554	2016	46
38/2		0.013	1.551	27.918	0.306	0.147	15.172	28.897	3.047	11.572	1.761	0.883	0.096	0.277	7.466	0.06	99.167	843	31

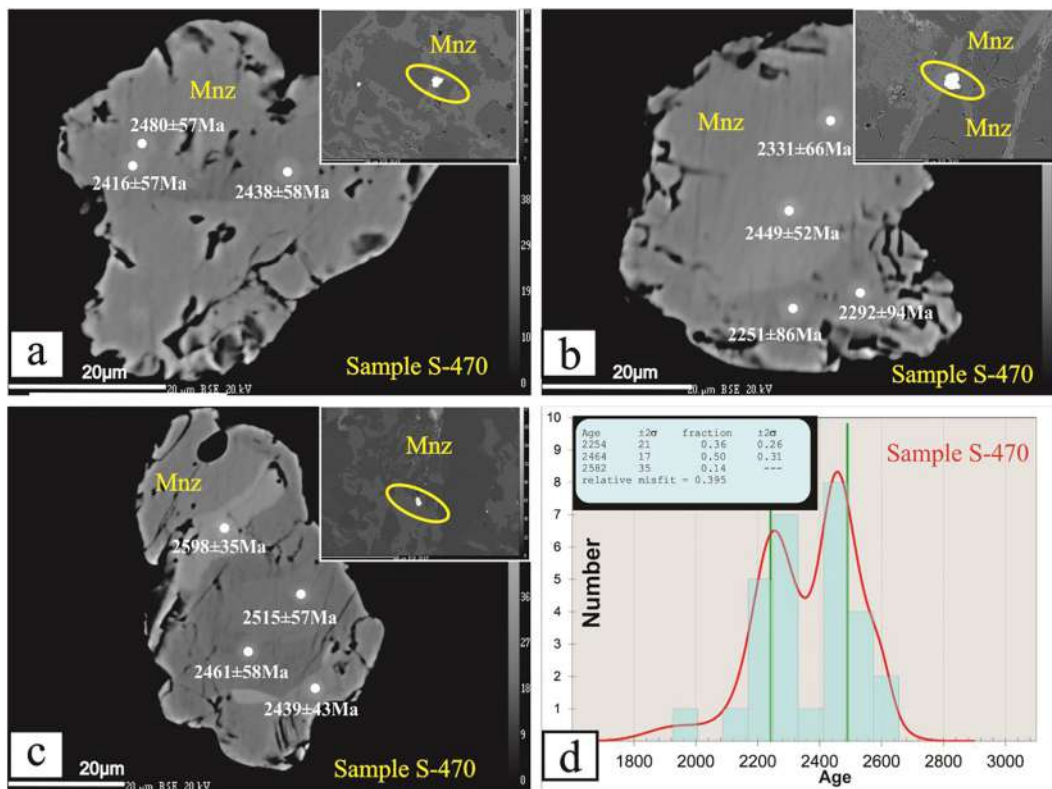


**Fig. 14.** (a–c) Sample S-470: granite gneisses from Kanjamalai hill, *Inset*: monazite grains are present within quartz without any feature related to DPC strain during D<sub>3</sub>- ductile shearing; (d) The histogram has two prominent peaks at ca. 2.4 and 2.3 Ma indicating age of metamorphism (M<sub>1</sub>), ca. 2.6 Ma peak reflects age of intrusion of granite gneiss.

mylonites because the pure shear strain axes was close to the simple shear strain axes. In steeply dipping D<sub>3</sub>- mylonitic foliation, the D<sub>3</sub>-stretching lineation had a pitch of 70–80° since the strain axes of pure and simple shear deviated similar to in an inclined transpression (Jones et al., 2004). Additionally, the Salem-Attur shear zone was developed on heterogeneous protolith with heterogeneity was produced due to D<sub>1–2</sub> deformation, metamorphism and melting. As a result orientation of D<sub>3</sub> strain fabric varied depending upon the attitude of preexisting heterogeneity and rheological properties of the rocks (Ramsay and Lisle, 2000; Jones et al., 2004). This was evident in lesser *Wm* estimates of ultramylonite where the interpreted protolith was weak (probably pseudotachylite). The weak protolith accommodated more compression than the mylonite.

### 5.2. Tectonothermal evolution of the Salem-Attur shear zone

The Salem Namakkal blocks underwent common magmatic history spanning over ca. 3.2–0.5 Ga as suggested by several phases of charnockitic and mafic granulite magma intrusion. The D<sub>1–2</sub> fabrics were related to granulite facies metamorphism. Pressure and temperature estimates of M<sub>1</sub> metamorphism (D<sub>1</sub> fabric) were inferred to be ca. 7 kb/800 °C. The D<sub>2</sub> deformation recorded a PT of 6 kb/700 °C indicated by dynamic recrystallization of plagioclase and chessboard twinning in quartz. The D<sub>1–2</sub> deformations were constrained at 2.5–2.3 Ga by both zircon and monazite geochronology (Table 5). As per the published work, the granulite facies metamorphism was correlated with Neo-archean-Paleoproterozoic subduction (Santosh et al., 2013; Brandt et al., 2014).

The D<sub>3</sub> fabric developed in greenschist to amphibolite facies condition and was defined by hornblende, biotite and muscovite. During D<sub>3</sub> deformation, the feldspar behaved as a brittle phase and quartz underwent sub grain rotation recrystallization. These criteria constrained the PT conditions at ca. 4 kb/500 °C, corresponding to the upper crust

(15 km). The D<sub>3</sub>- shearing was constrained at 2.0 Ga by monazite and hornblende geochronology (Table 5). The lower age limit of shearing was at ca. 1.9 Ga indicated by the age of a post D<sub>3</sub> and pre-D<sub>4</sub> pink granitic pluton. We, therefore infer that the Namakkal block was exhumed from lower to middle upper crust between ca. 2.5 Ga to 2.0 Ga. Orthopyroxene corona around garnet-clinopyroxene in the Namakkal block (Fig. 3d) suggested isothermal decompression (Harley, 1989; Thost et al., 1991; Kumar and Chacko, 1994; Biswal et al., 2007) related to thrust tectonics. The Salem block recorded a loading (Spear et al., 2002; Abati et al., 2003) or isobaric cooling (Harley, 1989; Thost et al., 1991) indicated by growth of garnet corona around M<sub>1</sub>-garnet-clinopyroxene-orthopyroxene (Fig. 3c inset).

Subsequently, the Salem-Attur shear zone was affected by brittle deformation (D<sub>4</sub>). The strike-slip faults were produced through N-S compression and injected by pseudotachylite veins as in the Gangavalli fault (Behera et al., 2017). High strain slip along the fault resulted in frictional melting of the rocks (above 1000 °C) to produce pseudotachylite. <sup>40</sup>Ar-<sup>39</sup>Ar geochronology of pseudotachylite constrained the shearing event at ca. 1.9 Ga (Table 5). Normal faults constituted a younger stage of brittle shearing when the rocks had undergone fluid activity alteration (e.g., Teufel and Heinrich, 1997). The age of shearing was broadly constrained between 0.8 and 0.5 Ga by the monazite and zircon ages (Sample S-478 and TKB-19, 20). Biotite obtained from the granite vein produced <sup>40</sup>Ar-<sup>39</sup>Ar cooling age at ca. 0.5 Ga (sample T-2, Table 5). Similar ages were obtained from different parts of the SGT. The Sankaridurg granite pluton, which was considered to be the source of granite-pegmatite veins, was reported to be Neo-proterozoic-Cambrian age (ca. 0.4–0.7 Ga. Pandey et al., 1993; Ghosh et al., 1994; Santosh et al., 2005). Alkaline granite and carbonatite intrusions were at ca.0.8 Ga (Schleicher et al., 1997) and thermal resetting of isotopic ages along the Moyar-Bhavani shear zone was at ca. 0.5 Ga (Detters-Umlauf et al., 1997; Meibner et al., 2002; Ghosh et al., 2004).

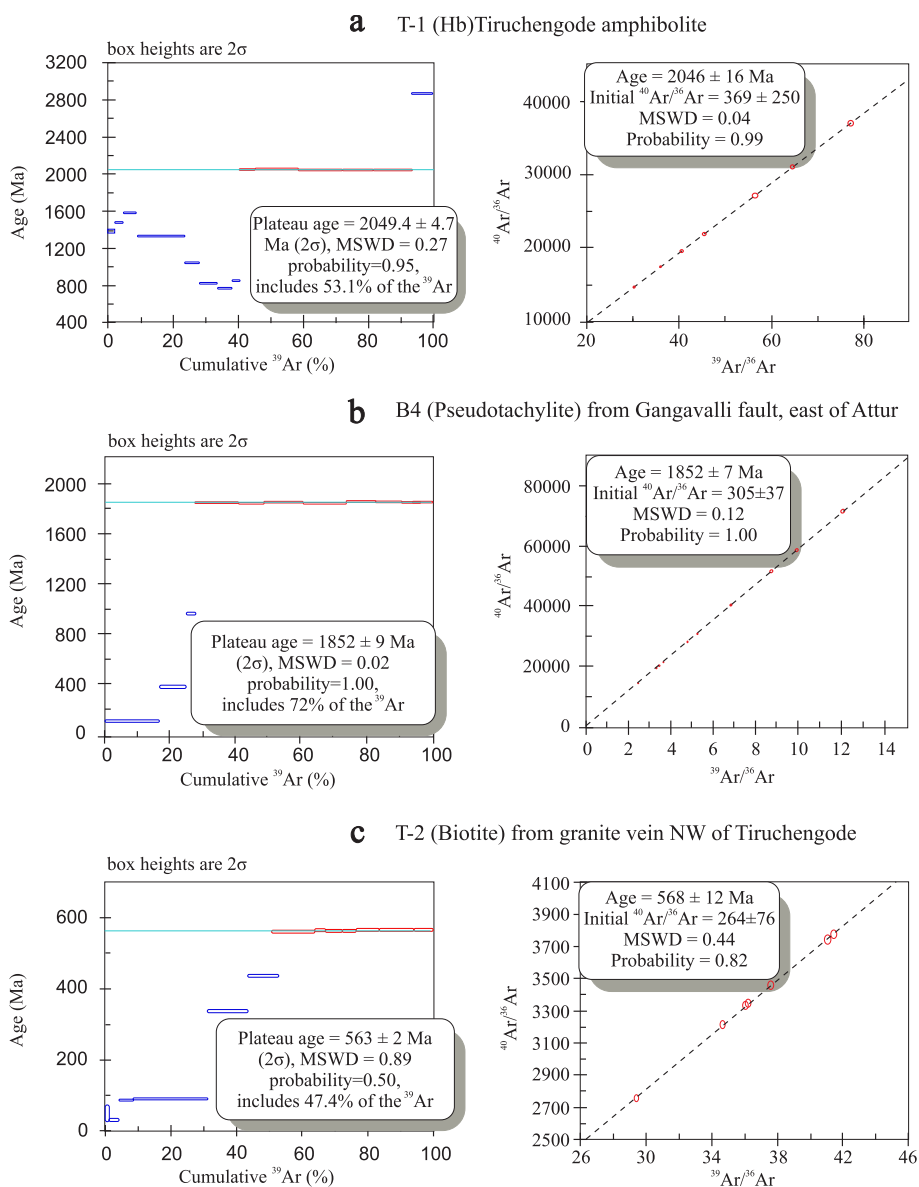


**Fig. 15.** (a) T-1 sample, hornblende from amphibolite from Tiruchengode, Fig. 1,  $^{40}\text{Ar}/^{39}\text{Ar}$  plateau spectra (left panels) and isochron plots (right panels); (b) Pseudotachylite from Gangavalli fault, close to Attur, Fig. 1; (c) Granite veins from NW of Tiruchengode Fig. 1. In the plateau spectra, the plateau is drawn with red outlines and the nonplateau with dark blue outlines. The value of mean square weighted deviate (MSWD) for each analysis is mentioned. (For interpretation of the references to color in this figure legend, the reader is referred to the web version of this article.)

**5.3. Tectonic implication**

The Salem-Namakkal blocks consisted of similar lithologies and a common magmatic and deformational history ( $D_{1-2}$ ). Charnockite magmatism was at ca 3.2–2.6 Ga and  $M_1$  metamorphism took place at 2.5–2.3 Ga (Clark et al., 2009; Plavsa et al., 2015, present study

Table 5). Hence, the blocks were contiguous before the  $D_3$ -Salem-Attur shear zone affected them at ca. 2.0 Ga. The Namakkal block overthrust the Salem block to the N-NNE. The regional map of the SGT depicted the Salem-Attur shear zone merging with Moyar-Bhavani shear zone to the west (Fig. 1 inset). The Moyar-Bhavani shear zones were not studied with respect to shear kinematics, strain pattern and

**Table 4**

Summary of  $^{40}\text{Ar}$ - $^{39}\text{Ar}$  dating results for sample T-1 (N11°28'14.86", E77°59'15.25") from amphibolite rock, sample B-4 (N11°28'10.09", E78°36'02.07") from pseudotachylite vein and sample T-2 (N11°32'52.15", E78°55'17.28") from granite vein.

Sample	Plateau					Isochron				Inverse isochron			
	Steps	% $^{39}\text{Ar}$	Age(Ma)	MSWD	p	Age(Ma)	Trap	MSWD	p	Age(Ma)	Trap	MSWD	p
T-1 (Hornblende from Tiruchengode)	16	53.1	2049.4 ± 4.7	0.27	0.95	2046 ± 16	369 ± 250	0.04	0.99	2046 ± 11	359 ± 150	0.12	0.99
B4 (Pseudotachylite from Gangavalli)	17	72	1852 ± 9	0.02	1.00	1852 ± 7	305 ± 37	0.12	1.00	1852 ± 7	295 ± 10	0.02	1.00
T-2 (Biotite from granite veins, NW of Tiruchengode)	13	47.4	563 ± 2	0.89	0.50	568 ± 12	264 ± 76	0.44	0.82	568.7 ± 9.7	262 ± 59	0.74	0.60

**Table 5**  
Comparison of tectonothermal age in Salem-Namakkal blocks.

Events	Salem block	Namakkal block
Intrusion of charnockites, granite gneiss Anorthosite intrusion Syenite intrusion	Ca.2.5 Ga Clark et al. (2009), Sato et al. (2011a)	Ca 2.5 Ga Ghosh et al. (2004) Ca.2.5 Ga (Present study, TKB-18, 19, 20) Ca. 2.5 Ga Mohan et al. (2013) Ca.2.5 Ga (Present study TKB-22)
Age of metamorphism D <sub>1</sub> and D <sub>2</sub> D <sub>2</sub> shearing	Ca. 2.4–2.5 Ga Clark et al. (2009) Ca. 2.4–2.5 Ga Sato et al. (2011a) Ca. 2.4–2.5 Ga, M <sub>2</sub> , ca. 2.3 Ga (Present study, S-470, monazite geochronology)	Ca.2.4–2.5 Ga Mohan et al. (2013) Ca. 2.5 Ga Plavsa et al. (2015) Ca. 2.5 Ga Brandt et al. (2014)
Age of ductile shearing D <sub>3</sub> shearing	Ca. 2.0 Ga (present study, S-478, monazite geochronology), ca 2.0 Ga ages are reported from Trivandrum block Ghosh et al. (2004), Second metamorphism in Moyar-Bhavani, Brandt et al. (2014)	Ca. 2.2 Ga Brandt et al. (2014)
Age of strike-slip shearing and pseudotachylite emplacement D <sub>4</sub> shearing	Ca.1.9 Ga (Present study, TKB-21), ca.1.8 Ga granitic magmatism Ghosh et al. (2004), Brandt et al. (2014)	
Age of normal faulting and granite-pegmatite vein intrusion D <sub>4</sub> shearing	Ca 0.8–0.5 Ga. (Present study, TKB-19,20, S-478), ca. 0.5 Ga Brandt et al. (2014), Plavsa et al. (2015)	

timing of shearing. The available age data suggested a reset ages at ca. 0.5 Ga (Deters-Umlauf et al., 1997). Recent geochemical and geochronological studies of rocks near the Bhavani shear zone suggested it to be a Neoproterozoic suture zone (Santosh et al., 2013; Brandt et al., 2014; Table 5). Similarly, the Palghat-Cauvery shear zone was once described to trace a late Neoproterozoic-Cambrian suture representing the closure of the Neo-proterozoic Mozambique Ocean during Gondwana amalgamation (Collins et al., 2007a; Santosh et al., 2009a,b, 2012; Sato et al., 2011a). In an alternative model the Palghat-Cauvery shear zone was considered a Neoproterozoic suture as ca. 2.5 Ga rocks existed on either side (Brandt et al., 2014). Brandt et al. (2014) suggested that the Karur-Kambam-Painavu-Trichur shear zone was a Late-Palaeoproterozoic to early-Mesoproterozoic collision zone. Our study on the Salem-Attur shear zone led to the interpretation that the shear zones between different blocks might not be suture zones, but they represented intra-terrane shear zones within a single Archean-Paleoproterozoic SGT. Even Palaeoproterozoic (2.0–1.6 Ga) crust existed in the Madurai as well as Trivandrum block (Braun et al., 1998; Ghosh et al., 2004; Table 5). The SGT has been reactivated during different period. There was stronger Pan-African overprint in the Madurai and Trivandrum blocks as these were closer to the Pan-African Betsimisaraka suture in Madagascar (Collins et al., 2007a). As the Salem-Namakkal block was far away from this proposed suture, the Pan-African orogeny was only expressed as brittle normal faults.

The SGT was considered to be a reworked part of the Dharwar craton. The Antongil (ca. 3.32–3.18 Ga; Tucker et al., 1999, 2011a; Schofield et al., 2010; Key et al., 2011; De Waele et al., 2011) and Antananarivo cratons (granulite facies metamorphism 2.5 Ga; Kroner et al., 2000) were considered part of the greater Dharwar craton (e.g., Tucker et al., 2011a, b). In this model, the Salem-Namakkal blocks could have been contiguous with Antananarivo block. The eastward extension of the Salem-Namakkal block to the Bastar craton and into Sri Lanka is unknown. The Madurai and Achankovil blocks were correlated with the Wani complex of Sri Lanka (Braun and Kriegsman, 2003; Cenki et al., 2004; Kooijman et al., 2011; Kroner et al., 2012; Plavsa et al., 2012). The Madurai block has been extended eastward into the Ongole domain of the Eastern Ghats mobile belt (Kovach et al., 2001; Bose et al., 2011; Sarkar and Schenk, 2012). It is thus plausible to suggest that fragments of the Dharwar craton, which underwent reworking during the Neoproterozoic-Paleoproterozoic period, now occur in several continental fragments of Gondwanaland. Most of these fragments later underwent Mesoproterozoic and Neoproterozoic-reworking, resulting in reactivation of shear zones.

## 6. Conclusions

Detailed structural mapping of the Salem-Namakkal blocks;

including kinematic study and vorticity analysis of the shear zone and multi-thermo-chronometric study of the magmatic rocks and mylonites were integrated to establish the tectonothermal evolution of the Salem-Attur shear zone of the SGT in South India. The lithological assemblage in the Salem-Namakkal blocks formed between 3.2 and 2.6 Ga, and were deformed (D<sub>1-2</sub>) and metamorphosed to granulite facies at 2.5 Ga and 2.3 Ga. The D<sub>1</sub> deformation produced F<sub>1</sub> isoclinal recumbent folds and S<sub>1</sub> subhorizontal fabric, while D<sub>2</sub> deformation produced tight upright to inclined F<sub>2</sub> folds. Several D<sub>2</sub> ductile shear zones were developed characterized by high temperature vertical shearing. The syenites (ca. 2.5 Ga) intruded syntectonically during D<sub>2</sub> shearing. Dynamic recrystallization of plagioclase and chessboard twinning in quartz of syenite suggested P-T conditions of 7 kb/600 °C. The Salem-Attur blocks formed a single block before the development of the Salem-Attur shear zone deformed it. The Salem-Attur shear zone formed during D<sub>3</sub> in feldspar brittle-quartz ductile zone. Charnockite, granite gneiss and quartzofeldspathic gneiss retrograded to quartz-biotite-muscovite mylonite, and mafic granulite to hornblende-albite mylonite. P-T conditions of around 4 kb/500 °C was interpreted for D<sub>2</sub> shearing based on retrogression of minerals, rotation recrystallization of quartz and brittle nature of feldspar. The Salem-Attur shear zone consisted of three southerly dipping imbricate thrusts with dips varying from near horizontal to subvertical. On low dipping mylonitic foliation, the stretching lineations were perfectly down dip; while in steeper foliation the pitch of the lineations was 70–80° which was attributed to pure shear component. Abundant shear sense criteria suggested an N-NNE verging thrust slip, suggesting that the Namakkal block was thrust over the Salem block. The kinematic vorticity number derived from RGN and Rs/θ analysis suggested general simple shear with 50% pure shear component. Th-U-total Pb monazite and hornblende <sup>40</sup>Ar-<sup>39</sup>Ar geochronology constrained the age of shearing to 2.0 Ga. Latter brittle deformation affected the Salem-Namakkal blocks including strike-slip shearing at 1.9 Ga and normal faulting at 0.5 Ga. The strike-slip faults were produced through N-S compression, with the high slip rates generated pseudotachylites along the Gangavalli fault. Normal faults were developed through extension during the Pan-African orogeny. We suggested that the Salem-Namakkal blocks experienced a long lived shearing history from ca. 2.5 Ga to 0.5 Ga and that shear zones were reactivated during different period of global orogeny. This polyphase tectonic evolution may be applicable for the entire SGT.

## Acknowledgements

We are extremely thankful to Prof. Kanchan Pande for supporting in Ar-Ar analysis at IIT Bombay-DST National Facility for <sup>40</sup>Ar-<sup>39</sup>Ar Geochronology funded by the Department of Science and Technology, Government of India (Grant No. IR/S4/ESF-04/200) and

maintenance support to the facility by the IRCC, IIT Bombay (Grant no. 15IRCCCF04). We are also thankful to IIT Bombay to provide the facilities of the electron probe microanalysis (EPMA) Lab at IIT Bombay and John de Laeter Centre at Curtin University, Western Australia, for the SHRIMP geochronology. We also thank the editor Prof. G. Zhao, associate editor Prof. R. Hariharan for handling the manuscript. Sebastián Oriolo and two anonymous reviewers are acknowledged for their constructive comments which helped in improving the standard of the manuscript.

## Appendix A. Supplementary data

Supplementary data to this article can be found online at <https://doi.org/10.1016/j.precamres.2019.01.022>.

## References

- Abati, J., Arenas, R., Martinez Catalan, J.R., Diaz Garcia, F., 2003. Anticlockwise P-T path of granulites from the Monte Castelo gabbro (Ordenes Complex, NW Spain). *J. Petrol.* 44 (2), 305–327.
- Anderson, J.R., Payne Justin, L., Kelsey David, E., Hand, M., Collins Alan, S., Santosh, M., 2012. High-pressure granulites at the dawn of the Proterozoic. *Geology* 40 (5), 431–434.
- Bartlett, J.M., Dougherty-Page, J.S., Hams, N.B.W., Hawksworth, C.J., Santosh, M., 1998. The application of single zircon evaporation and model Nd ages to the interpretation of polymetamorphic terranes: an example from the Proterozoic mobile belt of South India. *Contrib. Mineral. Petrol.* 131, 181–195.
- Behera, B.M., Thirukumaran, V., Soni, A., Mishra, P.K., Biswal, T.K., 2017. Size distribution and roundness of clasts within pseudotachylites of the Gangavalli Shear Zone, Salem, Tamil Nadu: An insight into its origin and tectonic significance. *J. Earth Sys. Sci.* 126 (4), 46.
- Bhaskar Rao, Y.J., Chetty, T.R.K., Janardhan, A.S., Gopalan, K., 1996. Sm-Nd and Rb-Sr ages and PT history of the Archean Sittampundi and Bhavani layered meta-anorthosite complexes in Cauvery shear zone, South India: evidence for Neoproterozoic reworking of Archean crust. *Contrib. Mineral. Petrol.* 125 (2), 237–250.
- Bhaskar Rao, Y.J., Janardhan, A.S., Kumar, T., Narayana, B.L., Dayal, A.M., Taylor, P.N., Chetty, T.R.K., 2003. Sm-Nd model ages and Rb-Sr isotopic systematics of charnockites and gneisses across the Cauvery shear zone of southern India: implications for the Archean-Neoproterozoic terrain boundary in the Southern Granulite Terrain. In: Ramakrishnan, M. (Ed.), *In Tectonics of Southern Granulite Terrain: Kuppam-Palani Geotranssect. Memoir J. Geol. Soc. India* 50.
- Bhutani, R., Balakrishnan, S., Nevin, C.G., Jeyabal, S., 2007. Sm-Nd isochron ages from Southern Granulite Terrain, South India: age of protolith and metamorphism. *Geochim. Cosmochim. Acta* 71 (15) A89 A89.
- Biswal, T.K., De Waele, B., Ahuja, H., 2007. Timing and dynamics of the juxtaposition of the Eastern Ghats Mobile Belt against the Bhandara Craton, India: a structural and zircon U-Pb SHRIMP study of the fold-thrust belt and associated nepheline syenite plutons. *Tectonics* 26 (4).
- Biswal, T.K., Thirukumaran, V., Rathe, K., Sundaralingam, K., 2009. Study of the Salem-Attur shear zone, east of Salem, Tamil Nadu: a new kinematic interpretation. *Curr. Sci.* 96 (10), 1–4.
- Biswal, T.K., Thirukumaran, V., Rathe, K., Bandyapadhyaya, K., Sundaralingam, K., Mondal, A.K., 2010. A Study of mylonites from parts of the salem-attur shear zone (Tamil Nadu) and its Tectonic Implications. *J. Geol. Soc. India* 75, 128–136.
- Black, L.P., Kamo, S.L., Williams, I.S., Mundil, R., Davis, D.W., Korsch, R.J., Foudoulis, C., 2003. The application of SHRIMP to Phanerozoic geochronology; a critical appraisal of four zircon standards. *Chem. Geol.* 200 (1), 171–188.
- Black, L.P., Kamo, S.L., Allen, C.M., Davis, D.W., Aleinikoff, J.N., Valley, J.W., Mundil, R., Campbell, I.H., Korsch, R.J., Williams, I.S., Foudoulis, C., 2004. Improved  $^{206}\text{Pb}/^{238}\text{U}$  microprobe geochronology by the monitoring of a trace-element-related matrix effect; SHRIMP, ID-TIMS, ELA-ICP-MS and oxygen isotope documentation for a series of zircon standards. *Chem. Geol.* 205 (1), 115–140.
- Bose, S., Dunkley, D.J., Dasgupta, S., Das, K., Arima, M., 2011. India-Antarctica-Australia-Laurentia connection in the Paleoproterozoic-Mesoproterozoic revisited: Evidence from new zircon U-Pb and monazite chemical age data from the Eastern Ghats Belt India. *Bulletin* 123 (9–10), 2031–2049.
- Brandt, S., Schenk, V., Raith, M.M., Appel, P., Gerdes, A., Srikantappa, C., 2011. Late Neoproterozoic PT evolution of HP-UHT granulites from the Palni Hills (South India): New constraints from phase diagram modelling, LA-ICP-MS zircon dating and in-situ EMP monazite dating. *J. Petrol.* 52 (9), 1813–1856.
- Brandt, S., Raith, M.M., Schenk, V., Sengupta, P., Srikantappa, C., Gerdes, A., 2014. Crustal evolution of the Southern Granulite Terrain, south India: New geochronological and geochemical data for felsic orthogneisses and granites. *Precamb. Res.* 246, 91–122.
- Braun, I., Montel, J.M., Nicollet, C., 1998. Electron microprobe dating of monazites from high-grade gneisses and pegmatites of the Kerala Khondalite Belt, southern India. *Chem. Geol.* 146 (1–2), 65–85.
- Braun, I., Kriegsman, L.M., 2003. Proterozoic crustal evolution of southernmost India and Sri Lanka. *Geol. Soc. London Spec. Pub.* 206 (1), 169–202.
- Braun, I., 2006. Pan-African granitic magmatism in the Kerala Khondalite Belt, southern India. *J. Asian Earth Sci.* 28 (1), 38–45.
- Braun, I., Cenki-Tok, B., Paquette, J.L., Tiepolo, M., 2007. Petrology and U-Th-Pb geochronology of the sapphirine-quartz-bearing metapelites from Rajapalayam, Madurai Block, Southern India: evidence for polyphase Neoproterozoic high-grade metamorphism. *Chem. Geol.* 241 (1), 129–147.
- Carreras, J., Druguet, E., 1994. Structural zonation as a result of inhomogeneous non-coaxial deformation and its control on syntectonic intrusions: an example from the Cap de Creus area, eastern-Pyrenees. *J. Struct. Geol.* 16 (11), 1525–1534.
- Chatterjee, A., Das, K., Bose, S., Ganguly, P., Hidaka, H., 2017. Zircon U-Pb SHRIMP and monazite EPMA U-Th-total Pb geochronology of granulites of the western boundary, Eastern Ghats Belt, India: a new possibility for Neoproterozoic exhumation history. *Geol. Soc. London Spec. Pub.* 457, SP457-1.
- Cherniak, D.J., Watson, E.B., 2001. Pb diffusion in zircon. *Chem. Geol.* 172 (1–2), 5–24.
- Cherniak, D.J., Watson, E.B., Grove, M., Harrison, T.M., 2004. Pb diffusion in monazite: a combined RBS/SIMS study. *Geochim. Cosmochim. Acta* 68 (4), 829–840.
- Cherniak, D.J., Pyle, J.M., 2008. Th diffusion in monazite. *Chem. Geol.* 256 (1–2), 52–61.
- Chetty, T.R.K., 1996. Proterozoic shear zones in Southern Granulite Terrain, India. The Archean and Proterozoic terranes in Southern India within East Gondwana. *Gondwana Res. Gr. Memoir* 3, 77–90.
- Chetty, T.R.K., Rao, Y.B., 1998. Behaviour of stretching lineations in the Salem-Attur shear belt, southern granulite terrane, South India. *J. Geol. Soc. India* 52 (4), 443–448.
- Chetty, T.R.K., Rao, Y.B., Narayana, B.L., 2003. A structural cross section along Krishnagiri-Palani corridor, Southern Granulite terrain of India. *Memoirs-Geol. Soc. India* 255–278.
- Chetty, T.R.K., Rao, Y.B., 2006. Constrictive deformation in transpressional regime: field evidence from the Cauvery Shear Zone, Southern Granulite Terrain India. *J. Struct. Geol.* 28 (4), 713–720.
- Cenki, B., Braun, I., Brocker, M., 2004. Evolution of the continental crust in the Kerala Khondalite Belt, southernmost India: evidence from Nd isotope mapping, U-Pb and Rb-Sr geochronology. *Precamb. Res.* 134 (3–4), 275–292.
- Claoue-Long, J., 1994. SHRIMP zircon data. 33.
- Clark, C., Collins, A.S., Timms, N.E., Kinny, P.D., Chetty, T.R.K., Santosh, M., 2009. SHRIMP U-Pb age constraints on magmatism and high-grade metamorphism in the Salem Block, southern India. *Gondwana Res.* 16 (1), 27–36.
- Collins, A.S., Clark, C., Sajeev, K., Santosh, M., Kelsey, D.E., Hand, M., 2007a. Passage through India: the Mozambique Ocean suture, high-pressure granulites and the Palghat-Cauvery shear zone system. *Terra Nova* 19 (2), 141–147.
- Collins, A.S., Santosh, M., Braun, I., Clark, C., 2007b. Age and sedimentary provenance of the Southern Granulites, South India: U-Th-Pb SHRIMP secondary ion mass spectrometry. *Precamb. Res.* 155 (1), 125–138.
- Collins, A.S., Clark, C., Plavsa, D., 2014. Peninsular India in Gondwana: the tectono-thermal evolution of the Southern Granulite Terrain and its Gondwanan counterparts. *Gondwana Res.* 25 (1), 190–203.
- Condie, K.C., 1986. Geochemistry and tectonic setting of early Proterozoic supracrustal rocks in the southwestern United States. *J. Geol.* 94 (6), 845–864.
- Dahl, P.S., 1997. A crystal-chemical basis for Pb retention and fission-track annealing systematics in U-bearing minerals, with implications for geochronology. *Earth Planet. Sci. Lett.* 150 (3–4), 277–290.
- Deshmukh, T., Prabhakar, N., Bhattacharya, A., Madhavan, K., 2017. Late Paleoproterozoic clockwise P-T history in the Mahakoshal Belt, Central Indian Tectonic Zone: Implications for Columbia supercontinent assembly. *Precamb. Res.* 298, 56–78.
- Deters-Umlauf, P., Srikantappa, C., Kohler, H., 1997. Pan-African ages in the Moyar-and Bhavani Shear Zone (South India): First geochronological results. In *Proceedings of the UNESCO-IUGS-IGCP-348/368, International field workshop on Proterozoic Geology of Madagascar, Antananarivo, Madagascar*, 16–30.
- De Waele, B., Thomas, R.J., Macey, P.H., Horstwood, M.S.A., Tucker, R.D., Pitfield, P.E.J., Schofield, D.I., Goodenough, K.M., Bauer, W., Key, R.M., Potter, C.J., 2011. Provenance and tectonic significance of the Palaeoproterozoic metasedimentary successions of central and northern Madagascar. *Precamb. Res.* 189 (1–2), 18–42.
- Dharma Rao, C., Santosh, M., Sajeev, K., Windley, B.F., 2013. Chromite-silicate chemistry of the Neoproterozoic Sittampundi Complex, southern India: Implications for subduction-related arc magmatism. *Precamb. Res.* 227, 259–275.
- Drury, S.A., Holt, R.W., 1980. The tectonic framework of the South Indian craton: a reconnaissance involving LANDSAT imagery. *Tectonophysics* 65 (3–4), 1–15.
- Drury, S.A., Harris, N.B.W., Holt, R.W., Reeves-Smith, G.J., Wightman, R.W., 1984. Precambrian tectonics and crustal evolution in South India. *J. Geol.* 92, 3–20.
- Dumond, G., McLean, N., Williams, M.L., Jercinovic, M.J., Bowring, S.A., 2008. High-resolution dating of granite petrogenesis and deformation in a lower crustal shear zone: athabasca granulite terrane, western Canadian Shield. *Chem. Geol.* 254 (3–4), 175–196.
- Dumond, G., Goncalves, P., Williams, M.L., Jercinovic, M.J., 2015. Monazite as a monitor of melting, garnet growth and feldspar recrystallization in continental lower crust. *J. Metamorph. Geol.* 33 (7), 735–762.
- Fossen, H., Tikoff, B., 1993. The deformation matrix for simultaneous simple shearing, pure shearing and volume change, and its application to transpression-transension tectonics. *J. Struct. Geol.* 15 (3–5), 413–422.
- Fossen, H., Cavalcanti, G.C.G., 2017. Shear zones—A review. *Earth-Sci. Rev.* 171, 434–455.
- Foster, G., Parrish, R.R., Horstwood, M.S., Chenery, S., Pyle, J., Gibson, H.D., 2004. The generation of prograde P-T-t points and paths; a textural, compositional, and chronological study of metamorphic monazite. *Earth Planet. Sci. Lett.* 228 (1–2), 125–142.
- Friend, C.R.L., Janardhan, A.S., 1984. Mineral chemistry of coexisting phases from shonkinitic rocks, Salem, Tamil Nadu, India. *Mineral. Mag.* 48, 181–193.

- Friend, C.R.L., Nutman, A.P., 1992. Response of zircon U-Pb isotopes and whole-rock geochemistry to CO<sub>2</sub> fluid-induced granulite-facies metamorphism, Kabbaldurga, Karnataka, South India. *Contrib. Mineral. Petrol.* 111 (3), 299–310.
- Ghosh, S.K., Rameberg, H., 1976. Reorientation of inclusions by combination of pure shear and simple shear. *Tectonophysics* 34 (1), 1–70.
- Ghosh, S., Paul, D.K., Bhalla, J.K., Bishui, P.K., Gupta, S.N., Chakraborty, S., 1994. New Rb-Sr isotopic ages and geochemistry of granitoids from Meghalaya and their significance in middle-to-late Proterozoic crustal evolution. *Indian Miner.* 48 (1–2), 33–44.
- Ghosh, J.G., De Wit, M.J., Zartman, R.E., 2004. Age and tectonic evolution of Neoproterozoic ductile shear zones in the Southern Granulite Terrain of India, with implications for Gondwana studies. *Tectonics* 23, TC3006.
- Goncalves, G.O., Lana, C., Scholz, R., Buick, L.S., Gerdes, A., Kamo, S.L., Corfu, F., Marinho, M.M., Chaves, A.O., Valeriano, C., Nalini Jr, H.A., 2016. An assessment of monazite from the Itambé pegmatite district for use as U-Pb isotope reference material for microanalysis and implications for the origin of the “Moacyr” monazite. *Chem. Geol.* 424, 30–50.
- Harley, S.L., 1989. The origin of granulites: a metamorphic perspective. *Geol. Mag.* 126, 215–247.
- Harris, N.B.W., Santosh, M., Taylor, P.N., 1994. Crustal evolution in South India: constraints from Nd isotopes. *J. Geol.* 102 (2), 139–150.
- Harrison, T.M., 1981. Diffusion of <sup>40</sup>Ar in hornblende. *Contrib. Mineral. Petrol.* 78 (3), 324–331.
- Harrison, T.M., Duncan, I., McDougall, I., 1985. Diffusion of <sup>40</sup>Ar in biotite: temperature, pressure and compositional effects. *Geochem. Cosmochem. Acta* 49 (11), 2461–2468.
- Jayananda, M., Janardhan, A.S., Sivasubramanian, P., Peucat, J.J., 1995. Geochronologic and isotopic constraints on granulite formation in the Kodaikanal area, Southern India. *Memoirs Geol. Soc. India* 373–390.
- Jercinovic, M.J., Williams, M.L., 2005. Analytical perils (and progress) in electron microprobe trace element analysis applied to geochronology: Background acquisition, interferences, and beam irradiation effects. *Amer. Mineral.* 90 (4), 526–546.
- Jercinovic, M.J., Williams, M.L., Lane, E.D., 2008. In-situ trace element analysis of monazite and other fine-grained accessory minerals by EPMA. *Chem. Geol.* 254 (3), 197–215.
- Jessup, M.J., Law, R.D., Frassi, C., 2007. The Rigid Grain Net (RGN): An alternative method for kinematic vorticity number (Wm). *J. Struct. Geol.* 29, 411–421.
- John, M.M., Balakrishnan, S., Bhadra, B.K., 2005. Contrasting metamorphism across Cauvery shear zone, south India. *J. Earth Sys. Sci.* 114 (2), 143–158.
- Jones, R.R., Holdsworth, R.E., Clegg, P., McCaffrey, K., Tavarnelli, E., 2004. Inclined transpression. *J. Struct. Geol.* 26 (8), 1531–1548.
- Just, J., Schulz, B., de Wall, H., Jourdan, F., Pandit, M.K., 2011. Monazite CHIME/EPMA dating of Erinpura granulite deformation: Implications for Neoproterozoic tectonothermal evolution of NW India. *Gondwana Res.* 19 (2), 402–412.
- Kelley, S.P., Reddy, S.M., Maddock, R., 1994. Laser-probe 40Ar/39Ar investigation of a pseudotachylite and its host rock from the Outer Isles thrust, Scotland. *Geology* 22 (5), 443–446.
- Kelsey, D.E., 2008. On ultrahigh-temperature crustal metamorphism. *Gondwana Res.* 13 (1), 1–29.
- Key, R.M., Pitfield, P.E.J., Thomas, R.J., Tucker, R.T., De Waele, B., Horstwood, M.S.A., Styles, M.T., 2011. Polyphase Neoproterozoic orogenesis within the East Africa–Antarctica Orogenic Belt in Madagascar. In: Van Hinsbergen, D.J.J., Buitter, S.J.H., Torsvik, T.H., Gaina, C., Webb, S.J. (Eds.), *The Formation and Evolution of Africa: A Synopsis of 3.8 Ga of Earth History*. Geol. Soc., London, Sp. Pub., pp. 49–68.
- Kooijman, E., Upadhyay, D., Mezger, K., Raith, M.M., Berndt, J., Srikanthappa, C., 2011. Response of the U-Pb chronometer and trace elements in zircon to ultrahigh-temperature metamorphism: the Kadavur anorthosite complex, southern India. *Chem. Geol.* 290 (3–4), 177–188.
- Kovach, V.P., Simmat, R., Rickers, K., Berezhnaya, N.G., Salnikova, E.B., Dobmeier, C., Raith, M.M., Yakovleva, S.Z., Kotov, A.B., 2001. The western charnockite zone of the eastern ghat belt, india—an independent crustal province of late archaean (2.8 Ga) and Palaeoproterozoic (1.7–1.6 Ga) Terrains. *Gondwana Res.* 4 (4), 666–667.
- Krohe, A., Wawrzenitz, N., 2000. Domainal variations of U-Pb monazite ages and Rb-Sr whole-rock dates in polymetamorphic paragneisses (KTB Drill Core, Germany): influence of strain and deformation mechanisms on isotope systems.
- Kroner, A., O'Brien, P.J., Nemchin, A.A., Pidgeon, R.T., 2000. Zircon ages for high pressure granulites from South Bohemia, Czech Republic, and their connection to Carboniferous high temperature processes. *Contrib. Mineral. Petrol.* 138 (2), 127–142.
- Kroner, A., Santosh, M., Wong, J., 2012. Zircon ages and Hf isotopic systematics reveal vestiges of Mesoproterozoic to Archaean crust within the late Neoproterozoic–Cambrian high-grade terrain of southernmost India. *Gondwana Res.* 21 (4), 876–886.
- Kruhl, J.H., 1996. Prism-and basal-plane parallel subgrain boundaries in quartz: a microstructural geothermobarometer. *J. Metamorph. Geol.* 14 (5), 581–589.
- Kumar, C.R., Chacko, T., 1994. Geothermobarometry of mafic granulites and metapelite from the Palghat Gap, South India: petrological evidence for isothermal uplift and rapid cooling. *J. Metamorph. Geol.* 12 (4), 479–492.
- Law, R.D., Searle, M.P., Simpson, R.L., 2004. Strain, deformation temperatures and vorticity of flow at the top of the Greater Himalayan Slab, Everest Massif, Tibet. *J. Geol. Soc. London* 161, 305–320.
- Lin, S., Jiang, D., Williams, P.F., 2007. Importance of differentiating ductile slickenside striations from stretching lineations and variation of shear direction across a high-strain zone. *J. Struct. Geol.* 29 (5), 850–862.
- Lisle, R.J., 1985. The use of the orientation tensor for the description and statistical testing of fabrics. *J. Struct. Geol.* 7 (1), 115–117.
- Ludwig, K., 2012. User's manual for Histogram version 3.75-4.15: a geochronological toolkit for Microsoft. Excel Berkley Geochronological Center Special Publication. 5.
- Magloughlin, J.F., Hall, C.M., Van der Pluijm, B.A., 2001. <sup>40</sup>Ar–<sup>39</sup>Ar geochronometry of pseudotachylites by vacuum encapsulation: North Cascade Mountains, Washington USA. *Geology* 29 (1), 51–54.
- Mahan, K.H., Goncalves, P., Williams, M.L., Jercinovic, M.J., 2006. Dating metamorphic reactions and fluid flow: application to exhumation of high-P granulites in a crustal-scale shear zone, western Canadian Shield. *J. Metamorph. Geol.* 24 (3), 193–217.
- McCourt, S., Vearncombe, J.R., 1987. Shear zones bounding the central zone of the Limpopo mobile belt, southern Africa. *J. Struct. Geol.* 9 (2), 127–137.
- Meibner, B., Deters, P., Srikanthappa, C., Kohler, H., 2002. Geochronological evolution of the Moyar, Bhavani and Palghat shear zones of southern India: implications for east Gondwana correlations. *Precamb. Res.* 114 (1), 149–175.
- Merlet, C., 1992. Quantitative electron probe microanalysis: new accurate  $\Phi(\rho z)$  description. In: *Electron Microbeam Analysis*. Springer, Vienna, pp. 107–115.
- Mohan, M.R., Satyanarayanan, M., Santosh, M., Sylvester, P.J., Tubrett, M., Lam, R., 2013. Neoproterozoic suprasubduction zone arc magmatism in southern India: Geochemistry, zircon U-Pb geochronology and Hf isotopes of the Sittampundi Anorthosite Complex. *Gondwana Res.* 23 (2), 539–557.
- Montel, J.M., Foret, S., Veschambre, M., Nicollet, C., Provost, A., 1996. Electron microprobe dating of monazite. *Chem. Geol.* 131 (1–4), 37–53.
- Mukhopadhyay, B., Bose, M.K., 1994. Transitional granulite-eclogite facies metamorphism of basic supracrustal rocks in a shear zone complex in the Precambrian shield of south India. *Mineral. Mag.* 58, 97–118.
- Mukhopadhyay, D., Kumar, P.S., Srinivasan, R., Bhattacharya, T., 2003. Nature of the Palghat-Cauvery lineament in the region South of Namakkal, Tamil Nadu: implications for terrane assembly in the South Indian granulite Province. *Memoirs Geol. Soc. India* 279–296.
- Naha, K., Srinivasan, R., 1996. Nature of the Moyar and Bhavani shear zones, with a note on its implication on the tectonics of the southern Indian Precambrian shield. *Proc. Indian Acad. Sci. Earth Planet. Sci.* 105 (2), 173.
- Nathan, N.P., Krishna Rao, A.V., Balasubramanian, E., Subramanian, N., Oberoi, L.K., Natarajan, V., Gopalakrishnan, K., Raman, R., Bhalla, J.K., 1994. Geochemistry and geochronology of this pegmatoidal granite of Sankari-Tiruchengode area, Tamil Nadu. *Indian Mineral.* 48 (1–2), 113–122.
- Nishimiya, Y., Tsunogae, T., Santosh, M., Dubessy, J., Chetty, T.R.K., 2009. Prograde and retrograde hoegbomites in sapphirine + quartz bearing Mg-Al rock from the Palghat-Cauvery suture zone, southern India. *J. Mineral. Petrol. Sci.* 104 (5), 319–323.
- Oriolo, S., Oyhantçabal, P., Wemmer, K., Basei, M.A., Benowitz, J., Pfänder, J., Hannich, F., Siegesmund, S., 2016. Timing of deformation in the Sarandí del Yí Shear Zone, Uruguay: Implications for the amalgamation of western Gondwana during the Neoproterozoic Brasiliano–Pan-African Orogeny. *Tectonics* 35 (3), 754–771.
- Oyhantçabal, P., Siegesmund, S., Wemmer, K., Layer, P., 2010. The sierra ballena shear zone in the southernmost dom feliciano belt (Uruguay): evolution, kinematics, and deformation conditions. *Int. J. Earth Sci.* 99 (6), 1227–1246.
- Oyhantçabal, P., Wagner-Eimer, M., Wemmer, K., Schulz, B., Frei, R., Siegesmund, S., 2012. Paleo- and Neoproterozoic magmatic and tectonometamorphic evolution of the Isla Cristalina de Rivera (Nico Pérez Terrane, Uruguay). *Int. J. Earth Sci.* 101 (7), 1745–1762.
- Pandey, B.K., Krishna, V., Sastry, D.V.L.N., Chabria, T., Mary, K.K., Dhana Raju, R., 1993. Pan-African Whole-rock Rb-Sr isochron ages for the granites and pegmatites of Kullampatti-Suriyamalai area, Salem District, Tamil Nadu, India. In: VI National Symposium on Mass spectrometry. Indian Institute of Petroleum, Dehradun, pp. 480–482 Abstract.
- Pant, N.C., Kundu, A., Joshi, S., Dey, A., Bhandari, A., Joshi, A., 2009. Chemical dating of monazite: testing of an analytical protocol against independently dated standards. *Indian J. Geosci.* 63, 311–318.
- Passchier, C.W., 1987. Stable positions of rigid objects in non-coaxial flow—a study in vorticity analysis. *J. Struct. Geol.* 9 (5–6), 679–690.
- Passchier, C.W., 1997. The fabric attractor. *J. Struct. Geol.* 19 (1), 113–127.
- Passchier, C.W., Trouw, R.A.J., 2005. *Microtectonics*, Second edition. Springer-Verlag, Berlin.
- Peucat, J.J., Mahabaleswar, B., Jayananda, M., 1993. Age of younger tonalitic magmatism and granulitic metamorphism in the South Indian transition zone (Krishnagiri area); comparison with older Peninsular gneisses from the Gorur-Hassan area. *J. Metamorph. Geol.* 11 (6), 879–888.
- Pidgeon, R.T., 1994. Calibration of zircon standards for the Curtin SHRIMP II. In *Abstract of Eighth International Conference on Geochronology, Cosmochronology and Isotope Geology*, 251.
- Plavsa, D., Collins, A.S., Foden, J.F., Kropinski, L., Santosh, M., Chetty, T.R.K., Clark, C., 2012. Delineating crustal domains in Peninsular India: age and chemistry of orthopyroxene-bearing felsic gneisses in the Madurai Block. *Precamb. Res.* 198, 77–93.
- Plavsa, D., Collins, A.S., Foden, J.D., Clark, C., 2015. The evolution of a Gondwanan collisional orogen: a structural and geochronological appraisal from the Southern Granulite Terrane, South India. *Tectonics* 34 (5), 820–857.
- Prabhakar, N., 2013. Resolving poly-metamorphic Paleoproterozoic ages by chemical dating of monazites using multi-spectrometer U, Th and Pb analyses and sub-counting methodology. *Chem. Geol.* 347, 255–270.
- Pryer, L.L., 1993. Microstructures in feldspars from a major crustal thrust zone: the Grenville Front, Ontario Canada. *J. Struct. Geol.* 15 (1), 21–36.
- Pyle, J.M., Spear, F.S., 2003. Yttrium zoning in garnet: Coupling of major and accessory phases during metamorphic reactions. *Amer. Mineral.* 88 (4) 708–708.
- Raith, M.M., Sengupta, P., Kooijman, E., Upadhyay, D., Srikanthappa, C., 2010. Corundum-leucosome-bearing aluminous gneiss from Ayyarmalai, Southern Granulite Terrain, India: A textbook example of vapor phase-absent muscovite-melting in silica-undersaturated aluminous rocks. *Amer. Miner.* 95 (7), 897–907.
- Rajaram, M., Harikumar, P., Balakrishnan, T.S., 2003. Thin magnetic crust in southern

- granulite terrain. *Memoir Geol. Soc. India* 50, 165–176.
- Rajesh, K.G., Chetty, T.R.K., 2006. Structure and tectonics of the Achankovil Shear Zone, southern India. *Gondwana Res.* 10 (1), 86–98.
- Ramakrishnan, M., Vaidyanadhan, R., 2008. *Geology of India*. Geol. Soc. India 1, 335–365.
- Ramsay, J.G., 1967. *Folding and fracturing of rocks*. McGraw-Hill, New York, pp. 103–109.
- Ramsay, J.G., 1980. Shear zone geometry: a review. *J. Struct. Geol.* 2 (1–2), 83–99.
- Ramsay, J.G., Huber, M.I., 1983. *The Techniques of Modern Structural Geology, Strain Analysis*. Academic Press, London.
- Ramsay, J.G., Huber, M.I., 1987. *The Techniques of Modern Structural Geology*. Academic press, London.
- Ramsay, J.G., Lisle, R.J., 2000. *The Techniques of Modern Structural Geology. Applications of Continuum Mechanics in Structural Geology*. Academic, San Diego, California.
- Rao, Y.B., Chetty, T.R.K., Janardhan, A.S., Gopalan, K., 1996. Sm-Nd and Rb-Sr ages and PT history of the Archean Sittampundi and Bhavani layered meta-anorthositic complexes in Cauvery shear zone, South India: evidence for Neoproterozoic reworking of Archean crust. *Contrib. Mineral. Petrol.* 125 (2–3), 237–250.
- Reddy, B.M., Janardhanan, A.S., Peucat, J.J., 1995. Geochemistry, age and origin of alkaline and ultramafic rocks of Salem, Tamil Nadu, South India. *Geol. Soc. India* 45 (3), 251–262.
- Renne, P.R., Swisher, C.C., Deino, A.L., Karner, D.B., Owens, T.L., DePaolo, D.J., 1998. Intercalibration of standards, absolute ages and uncertainties in  $^{40}\text{Ar}/^{39}\text{Ar}$  dating. *Chem. Geol.* 145 (1–2), 117–152.
- Rosenberg, C.L., Stunitz, H., 2003. Deformation and recrystallization of plagioclase along a temperature gradient: an example from the Bergell tonalite. *J. Struct. Geol.* 25 (3), 389–408.
- Saitoh, Y., Tsunogae, T., Santosh, M., Chetty, T.R.K., Horie, K., 2011. Neoproterozoic high-pressure metamorphism from the northern margin of the Palghat-Cauvery Suture Zone, southern India: Petrology and zircon SHRIMP geochronology. *J. Asian Earth Sci.* 42 (3), 268–285.
- Sambridge, M.S., Compston, W., 1994. Mixture modeling of multi-component data sets with application to ion-probe zircon ages. *Earth Planet. Sci. Lett.* 128 (3–4), 373–390.
- Santosh, M., Tanaka, K., Yokoyama, K., Collins, A.S., 2005. Late Neoproterozoic–Cambrian felsic magmatism along transcrustal shear zones in southern India: U–Pb electron microprobe ages and implications for the amalgamation of the Gondwana supercontinent. *Gondwana Res.* 8 (1), 31–42.
- Santosh, M., Collins, A.S., Tamashiro, I., Koshimoto, S., Tsutsumi, Y., Yokoyama, K., 2006a. The timing of ultrahigh-temperature metamorphism in Southern India: U–Th–Pb electron microprobe ages from zircon and monazite in sapphirine-bearing granulites. *Gondwana Res.* 10 (1), 128–155.
- Santosh, M., Morimoto, T., Tsutsumi, Y., 2006b. Geochronology of the khondalite belt of Trivandrum Block, southern India: electron probe ages and implications for Gondwana tectonics. *Gondwana Res.* 9 (3), 261–278.
- Santosh, M., Tagawa, M., Yokoyama, K., Collins, A.S., 2006c. U–Pb electron probe geochronology of the Nagercoil granulites, Southern India: implications for Gondwana amalgamation. *J. Asian Earth Sci.* 28 (1), 63–80.
- Santosh, M., Maruyama, S., Sato, K., 2009a. Anatomy of a Cambrian suture in Gondwana: Pacific type orogeny in southern India? *Gondwana Res.* 16, 321–341.
- Santosh, M., Tsunogae, T., Tsutsumi, Y., Iwamura, M., 2009b. Microstructurally controlled monazite chronology of ultrahigh-temperature granulites from southern India: Implications for the timing of Gondwana assembly. *Island Arc.* 18 (2), 248–265.
- Santosh, M., Xiao, W.J., Tsunogae, T., Chetty, T.R.K., Yellappa, T., 2012. The Neoproterozoic subduction complex in southern India: SIMS zircon U–Pb ages and implications for Gondwana assembly. *Precamb. Res.* 192, 190–208.
- Santosh, M., Shaji, E., Tsunogae, T., Mohan, M.R., Satyanarayanan, M., Horie, K., 2013. Suprasubduction zone ophiolite from Agali hill: petrology, zircon SHRIMP U–Pb geochronology, geochemistry and implications for Neoproterozoic plate tectonics in southern India. *Precamb. Res.* 231, 301–324.
- Sarkar, T., Schenk, V., 2012. The granulite facies Ongole domain of the Eastern Ghats Belt, India—a Proterozoic island arc. *EMC2012, Frankfurt*, 311.
- Satheesh Kumar, R., Prasannakumar, V., 2009. Fabric evolution in Salem-Attur Shear Zone, South India, and its implications on the kinematics. *Gondwana Res.* 16 (1), 37–44.
- Sato, K., Santosh, M., Tsunogae, T., 2009. A petrologic and laser Raman spectroscopic study of sapphirine-spinel-quartz-Mg-staurolite inclusions in garnet from Kumiloathu, southern India: Implications for extreme metamorphism in a collisional orogen. *J. Geodyn.* 47 (2), 107–118.
- Sato, K., Santosh, M., Tsunogae, T., Chetty, T.R.K., Hirata, T., 2011a. Laser ablation ICP mass spectrometry for zircon U–Pb geochronology of metamorphosed granite from the Salem Block: implication for Neoproterozoic crustal evolution in southern India. *J. Mineral. Petrol. Sci.* 106, 1–12.
- Sato, K., Santosh, M., Tsunogae, T., Chetty, T.R.K., Hirata, T., 2011b. Subduction-accretion-collision history along the Gondwana suture in southern India: a laser ablation ICP-MS study of zircon chronology. *J. Asian Earth Sci.* 40 (1), 162–171.
- Schleicher, H., Todt, W., Viladkar, S.G., Schmidt, F., 1997. Pb/Pb age determinations on the Newania and Sevattur carbonates of India: evidence for multi-stage histories. *Chem. Geol.* 140 (3–4), 261–273.
- Schofield, D.I., Thomas, R.J., Goodenough, K.M., De Waele, B., Pitfield, P.E.J., Key, R.M., Bauer, W., Walsh, G.J., Lidke, D.J., Ralison, A.V., Rabarimanana, M., Rafahatelo, J.M., Randriamananjara, T., 2010. Geological evolution of the Antongil Craton, NE Madagascar. *Precamb. Res.* 182, 187–203.
- Sherlock, S.C., Strachan, R.A., Jones, K.A., 2009. High spatial resolution  $^{40}\text{Ar}/^{39}\text{Ar}$  dating of pseudotachylites: geochronological evidence for multiple phases of faulting within basement gneisses of the Outer Hebrides (UK). *J. Geol. Soc.* 166 (6), 1049–1059.
- Shimpo, M., Tsunogae, T., Santosh, M., 2006. First report of garnet–corundum rocks from southern India: implications for prograde high-pressure (eclogite-facies?) metamorphism. *Earth Planet. Sci. Lett.* 242 (1), 111–129.
- Simpson, C., De Paor, D.G., 1993. Strain and kinematic analysis in general shear zones. *J. Struct. Geol.* 15 (1), 1–20.
- Simpson, C., De Paor, D.G., 1997. Practical analysis of general shear zones using the porphyroblast hyperbolic distribution method: an example from the Scandinavian Caledonides. In: *Evolution of Geological Structures in Micro-to Macro-Scales*. Springer, Netherlands, pp. 169–184.
- Sims, J.P., Ireland, T.R., Camacho, A., Lyons, P., Pieters, P.E., Skirrow, R.G., Stuart-Smith, P.G., Miro, R., 1998. U–Pb, Th–Pb and Ar–Ar geochronology from the southern Sierrita Pampeanas, Argentina: implications for the Palaeozoic tectonic evolution of the western Gondwana margin. *Geol. Soc. London, Spec. Pub.* 142 (1), 259–281.
- Spear, F.S., Kohn, M.J., Cheney, J.T., Florence, F., 2002. Metamorphic, thermal, and tectonic evolution of central New England. *J. Petrol.* 43 (11), 2097–2120.
- Spear, F.S., Wark, D.A., 2009. Cathodoluminescence imaging and titanium thermometry in metamorphic quartz. *J. Metamorph. Geol.* 27 (3), 187–205.
- Stacey, J.T., Kramers, J.D., 1975. Approximation of terrestrial lead isotope evolution by a two-stage model. *Earth Planet. Sci. Lett.* 26 (2), 207–221.
- Stahr, D.W., Law, R.D., 2011. Effect of finite strain on clast-based vorticity gauges. *J. Struct. Geol.* 33 (7), 1178–1192.
- Stahr, D.W., Law, R.D., 2014. Strain memory of 2D and 3D rigid inclusion populations in viscous flows—What is clast SPO telling us? *J. Struct. Geol.* 68, 347–363.
- Stern, R.A., 2001. A new isotopic and trace-element standard for the ion microprobe: preliminary thermal ionization mass spectrometry (TIMS) U–Pb and electron-microprobe data. *Ressources naturelles Canada*, 11.
- Stipp, M., Stuenkel, H., Heilbronner, R., Schmid, S.M., 2002. The eastern Tonale fault zone: a ‘natural laboratory’ for crystal plastic deformation of quartz over a temperature range from 250 to 700 °C. *J. Struct. Geol.* 24 (12), 1861–1884.
- Subramanyam, A.P., 1956. Mineralogy and petrology of the Sittampundi complex, Salem district, Madras, India. *Geol. Soc. Amer. Bull.* 67, 317–389.
- Sundaralingam, K., Waele, B.D., Thirukumaran, V., Thakur, S.S., Tanushree, M., Biswal, T.K., 2012. Deformation, metamorphism and geochronology of the Palaeoproterozoic Salem-Namakal fold thrust belt and implication for the Gondwanaland continental assembly. *Int. J. Earth Environ. Sci.* 2 (2), 266–283.
- Sundaralingam, K., Biswal, T.K., Thirukumaran, V., 2017. Strain analysis of the salem-attur shear zone of southern granulite terrane around Salem, Tamil Nadu. *Geol. Soc. India* 89 (1), 5–11.
- Suzuki, K., Adachi, M., 1991. The chemical Th–U–total Pb isochron ages of zircon and monazite from the Gray Granite of the Hida terrane, Japan. *Earth Sci. Nagoya Univ.* 38, 11–37.
- Suzuki, K., Kato, T., 2008. CHIME dating of monazite, xenotime, zircon and polycrase: protocol, pitfalls and chemical criterion of possibly discordant age data. *Gondwana Res.* 14 (4), 569–586.
- Teufel, S., Heinrich, W., 1997. Partial resetting of the U–Pb isotope system in monazite through hydrothermal experiments: An SEM and U–Pb isotope study. *Chem. Geol.* 137 (3–4), 273–281.
- Thost, D.E., Hensen, B.J., Motoyoshi, Y., 1991. Two-stage decompression in garnet-bearing mafic granulites from Sostrene Island, Prydz Bay, East Antarctica. *J. Metamorph. Geol.* 9 (3), 245–256.
- Tikoff, B., Fossen, H., 1995. The limitations of three-dimensional kinematic vorticity analysis. *J. Struct. Geol.* 17 (12), 1771–1784.
- Tomson, J.K., Rao, Y.B., Kumar, T.V., Rao, J.M., 2006. Charnokite genesis across the Archean-Proterozoic terrane boundary in the South Indian Granulite Terrain: Constraints from major-trace element geochemistry and Sr–Nd isotopic systematics. *Gondwana Res.* 10 (1), 115–127.
- Tsunogae, T., Santosh, M., 2006. Reply to Comment on “First report of garnet–corundum rocks from Southern India: implications for prograde high-pressure (eclogite-facies?) metamorphism” by D. E. Kelsey, C. Clark, M. Hand, A. S. Collins. *Earth Planet. Sci. Lett.* 249, 535–540.
- Tucker, R.D., Ashwal, L.D., Handke, M.J., Hamilton, M.A., Le Grange, M., Rambeloson, R.A., 1999. U–Pb geochronology and isotope geochemistry of the Archean and Proterozoic rocks of north-central Madagascar. *J. Geol.* 107 (2), 135–153.
- Tucker, R.D., Roig, J.Y., Delor, C., Amelin, Y., Goncalves, P., Rabarimanana, M.H., Ralison, A.V., Belcher, R.W., 2011a. Neoproterozoic extension in the Greater Dharwar Craton: a reevaluation of the “Betsimisaraka suture” in Madagascar. *Can. J. Earth Sci.* 48 (2), 389–417.
- Tucker, R.D., Roig, J.Y., Macey, P.H., Delor, C., Amelin, Y., Armstrong, R.A., Rabarimanana, M.H., Ralison, A.V., 2011b. A new geological framework for south-central Madagascar, and its relevance to the “out-of-Africa” hypothesis. *Precamb. Res.* 185 (3–4), 109–130.
- Valdiya, K.S., 1984. *Aspects of tectonics: focus on south-central Asia*. Tata McGraw-Hill Publishing Company Limited, New Delhi.
- Vinogradov, A., Tugarinov, A.L., Zhykov, C., Stapanikova, N., Bibikova, E., Khorre, K., 1964. Geochronology of Indian Precambrian. In *Report of the 22nd Int. Congress, New Delhi*, 10, 553–567.
- Vlach, S.R.F., 2010. Th–U–Pb dating by electron probe microanalysis, part I. Monazite: analytical procedures and data treatment. *Geologia USP: Serie Cientifica*, 10(1), 61–85.
- Wallis, S.R., Platt, J.P., Knott, S.D., 1993. Recognition of syn-convergence extension in accretionary wedges with examples from the Calabrian Arc and the Eastern Alps. *Amer. J. Sci.* 293 (5), 463–494.
- Wallis, S.I.M.O.N., 1995. Vorticity analysis and recognition of ductile extension in the Sanbagawa belt, SW Japan. *J. Struct. Geol.* 17 (8), 1077–1093.
- Warr, L.N., Van Der Pluijm, B.A., Tourscher, S., 2007. The age and depth of exhumed friction melts along the Alpine fault, New Zealand. *Geology* 35 (7), 603–606.

- Wawrzenitz, N., Krohe, A., Rhede, D., Romer, R.L., 2012. Dating rock deformation with monazite: The impact of dissolution precipitation creep. *Lithos* 134, 52–74.
- Williams, M.L., Jercinovic, M.J., 2002. Microprobe monazite geochronology: putting absolute time into microstructural analysis. *J. Struct. Geol.* 24 (6–7), 1013–1028.
- Williams, M.L., Jercinovic, M.J., Hetherington, C.J., 2007. Microprobe monazite geochronology: understanding geologic processes by integrating composition and chronology. *Annu. Rev. Earth Planet. Sci.* 35, 137–175.
- Xypolias, P., 2009. Some new aspects of kinematic vorticity analysis in naturally deformed quartzites. *J. Struct. Geol.* 31 (1), 3–10.
- Xypolias, P., 2010. Vorticity analysis in shear zones: a review of methods and applications. *J. Struct. Geol.* 32 (12), 2072–2092.
- Yellappa, T., Chetty, T.R.K., Tsunogae, T., Santosh, M., 2010. The Manamedu Complex: Geochemical constraints on Neoproterozoic suprasubduction zone ophiolite formation within the Gondwana suture in southern India. *J. Geodyn.* 50 (3), 268–285.
- Zhu, X.K., O’Nions, R.K., 1999. Monazite chemical composition: some implications for monazite geochronology. *Contrib. Mineral. Petrol.* 137 (4), 351–363.